



**DEGRADATION OF CARBON FIBER REINFORCED POLYMER AND
GRAPHITE BY LASER HEATING**

DISSERTATION

Nicholas C. Herr, Captain, USAF

AFIT-ENP-DS-16-S-025

**DEPARTMENT OF THE AIR FORCE
AIR UNIVERSITY**

AIR FORCE INSTITUTE OF TECHNOLOGY

Wright-Patterson Air Force Base, Ohio

DISTRIBUTION STATEMENT A.
APPROVED FOR PUBLIC RELEASE; DISTRIBUTION UNLIMITED.

The views expressed in this thesis are those of the author and do not reflect the official policy or position of the United States Air Force, Department of Defense, or the United States Government. This material is declared a work of the U.S. Government and is not subject to copyright protection in the United States.

AFIT-ENP-DS-16-S-025

**DEGRADATION OF CARBON FIBER REINFORCED POLYMER AND
GRAPHITE BY LASER HEATING**

DISSERTATION

Presented to the Faculty

Department of Engineering Physics

Graduate School of Engineering and Management

Air Force Institute of Technology

Air University

Air Education and Training Command

In Partial Fulfillment of the Requirements for the

Degree of Doctor of Philosophy

Nicholas C. Herr, BS, MS

Captain, USAF

August 2016

DISTRIBUTION STATEMENT A.
APPROVED FOR PUBLIC RELEASE; DISTRIBUTION UNLIMITED.

**DEGRADATION OF CARBON FIBER REINFORCED POLYMER AND
GRAPHITE BY LASER HEATING**

Nicholas C. Herr, BS, MS

Captain, USAF

Committee Membership:

Dr. Glen. P. Perram
Chair

Dr. Michael A. Marciniak
Member

Dr. Marina B. Ruggles-Wrenn
Member

ADEDJI B. BADIRU, PhD
Dean, Graduate School of Engineering and Management

Abstract

Emissivity-adjusted surface temperatures from laser irradiated carbon fiber reinforced polymer (CFRP) and porous graphite targets were measured using a mid wave infrared (MWIR) thermal camera and modeled to determine changing material thermal properties and decomposition kinetics. The resultant CFRP model was used to predict and analyze residual compressive strengths following laser irradiation. Decomposition plumes were investigated using a MWIR imaging Fourier transform infrared (FTIR) spectrometer to define ignition conditions. CFRP and graphite targets were irradiated with a 1.07 μm ytterbium doped continuous wave (cw) fiber laser under buoyant conditions at irradiances ranging from 5-525 W/cm^2 and 780-3000 W/cm^2 , respectively. Surface temperatures were measured at spatial resolutions of 0.32-1.49 mm/pixel and frame rates of 30-240 Hz at four integration times to give a dynamic temperature range of > 3000 K. Temperatures were corrected with surface emissivity, ranging from $\epsilon = 0.93$ -0.75 as CFRP decomposed and from $\epsilon = 0.81 - 0.9$ as graphite binder was removed. A 3D, explicit finite difference, thermal model based on Fourier's heat diffusion equation with Neumann boundary conditions for laser absorption, surface emission, and convection was used to estimate Arrhenius decomposition reaction kinetic constants for CFRP, as well as binder removal and sublimation kinetics for graphite samples. CFRP decomposition was observed to be a two-step process with activation energies of 120 and 150 kJ/mol, heats of reaction of -1.3 and -1.0 MJ/kg, and little dependence on heating rate at heating rates of 12-330 K/s. Thickness conductivity fell from 0.6 to 0.1 W/m K

during decomposition. Graphite temperatures of 2250-3600 K were reached by irradiances of 780-3000 W/cm², with binder removal occurring from 2200-2900 K and sublimation beginning at 3500 K. Binder removal had an activation energy of 350 kJ/mol and a heat of reaction of -29.2 MJ/kg. Residual CFRP compressive strengths of 27-59% remained when limited to front side combustion only, decreasing to 5-10% with the addition of backside combustion. Under buoyant conditions, surface ignition of CFRP under HEL irradiation requires surface temperatures of 1451 ± 48 K and is not dependent on critical levels of volatile decomposition products.

Acknowledgments

I would like to express my sincere appreciation to my wife and children for their love and support throughout this academic program. I am thankful to my parents as well for their love, sacrifice, and for teaching me about hard work and the value of education. Many thanks are due to my advisor, Prof. Glen Perram, for his patience, dedication, guidance and help throughout this whole process. I am grateful to be a part of Dr. Perram's research group and especially want to thank fellow students Capt Ashley Gonzales, Capt William Bauer, and Charles Fox for their collaboration and assistance.

I would also like to thank my committee members, Dr. Michael Marciniak and Dr. Marina Ruggles-Wrenn, for their expertise and for access to their research facilities. I owe a similar debt to the Air Force Research Laboratory, Laser Effects Branch (AFRL/RDLE), especially Capt Chris McGahan, for their assistance during laser testing. Finally, thank you to the High Energy Laser Joint Technology Office (HEL-JTO) for funding this research.

Nicholas C. Herr

Table of Contents

	Page
Abstract	iv
Acknowledgments.....	vi
Table of Contents	vii
List of Figures	ix
List of Tables	xviii
I. Introduction	1
Document Overview	3
II. Background	5
Introduction	5
Materials	5
Carbon Fiber Reinforced Polymers (CFRP).....	5
Graphite	8
Laser Material Interactions	10
Epoxy Decomposition Kinetics	13
Radiometric Temperature Measurement.....	16
Thermal Modeling.....	19
Strength Testing	23
Fourier Transform Spectroscopy.....	25
III. Thermal Imagery and Modeling of Laser Irradiated Carbon Fiber Composite	28
Introduction	28
Experimental	31
Results and discussion.....	34
Sample response to laser radiation.....	34
Thermal imagery.....	36
Thermal model.....	45
Conclusions	56

IV. Thermal Imagery and Modeling of Laser Irradiated Graphite	58
Introduction	58
Experimental	60
Results and discussion.....	63
Surface Emissivity	63
Surface temperatures.....	66
Thermal modeling.....	71
Conclusions	83
V. Carbon Fiber Composite Laser-induced Compressive Strength Reduction	85
Introduction	85
Experimental	87
Results and Discussion.....	90
Surface Temperatures	93
Model	99
Conclusions	104
VI. Carbon Fiber Composite Laser-Induced Surface Ignition.....	106
Introduction	106
Experimental	107
Results and Discussion.....	108
Conclusions	116
VII. Conclusions	117
Key Results	117
Carbon Fiber Composite.....	118
Graphite	118
Carbon Fiber Composite Strength Reduction.....	120
Carbon Fiber Composite Ignition Conditions.....	120
Recommendations for Future Work.....	121
Appendix A. Thermal Model Sensitivity Analysis.....	123
Bibliography	134
Vita.....	143

List of Figures

Figure	Page
Fig. 1. Gas-phase Infrared Spectra of Volatile Degradation Products [56]. (a) Bisphenol A (b) Phenol (c) m-Cresol (d) 4-Isopropylphenol (e) Propene (f) Methane	27
Fig. 2. Experimental Schematic	32
Fig. 3. Visible images of 3.1 mm panel, 35.7 W/cm ² : (a) undamaged CFRP panel, (b) laser spot (1 sec), (c) smoky decomposition plume (5 sec), (d) surface flame (45 sec), (e) flame after laser-off (58 sec), and (f) final damaged panel. Panel dimensions are 10.2 x 10.2 cm.	35
Fig. 4. Sample Mass Loss under (♦) ignition and (●) non-ignition conditions at 6 cm spot size and ignition at 2.3 cm spot (■).	36
Fig. 5. (a) Temporally averaged laser center irradiance profile in vertical direction at 9.9 W/cm ² spatially averaged irradiance at measured and modeled spatial resolution, (b) uncalibrated FLIR signal at 4 integration times (0.1, 0.3, 2, and 4 ms) for a vertical slice through laser center at 9.9 W/cm ² and 30 s, (c) signal from part (b) calibrated for absolute temperature at: $\epsilon = 1$ (solid line) with offsets to illustrate overlap from different integration times (dotted lines) and $\epsilon = 0.85$ (dashed line) with all integration times overlaid, and (d) final FLIR front surface temperature map (°C) showing vertical temperature slice used for parts (a-c).	38
Fig. 6. Emissivity (a) decreases with wavelength and as decomposition progresses from [—] virgin resin to [—] char to [—] bare fiber, (b) emissivity is constant over the	

bandwidth of the MWIR camera, (c) emissivity at $3.9\text{ }\mu\text{m}$ decreases slowly as temperature increases and (d) temperature error due to incorrect emissivity (true $\epsilon = 0.75$) at $3.9\text{ }\mu\text{m}$ at [—] $100\text{ }^{\circ}\text{C}$, [+] $500\text{ }^{\circ}\text{C}$, [*] $900\text{ }^{\circ}\text{C}$, and [o] $1400\text{ }^{\circ}\text{C}$ 40

Fig. 7. Measured absorptivity of (a) undamaged CFRP (b) charred CFRP and (c) bare fiber at $1.07\text{ }\mu\text{m}$ and surrounding wavelengths. 41

Fig. 8. (filled symbols) front and (open symbols) backside temperatures for a 3.1 mm thick panel at (•) 5 W/cm^2 , (♦) 9.8 W/cm^2 , (■) 35.7 W/cm^2 , and (*) 63.7 W/cm^2 . Markers are included at point of maximum decomposition (*) and ignition (+). 44

Fig. 9. Evolving temperatures at laser center for (a) 9.9 W/cm^2 and (b) 35.6 W/cm^2 . Comparisons are made between (filled symbols) front surface and (open symbols) back surface laser center temperatures for sample thicknesses of (•) 3.2 mm (♦) 2.4 mm , and (■) 1.7 mm 44

Fig. 10. Front (—), backside (—), and modeled (---) laser center temperatures of 3.2 mm thick panels at (a-c) 5 W/cm^2 and (d-f) 10 W/cm^2 . Radial temperature profile comparisons are shown at 30, 60, and 120 seconds (increasing throughout). 51

Fig. 11. Model fit (dashed) of front and back side temperatures at laser center. Multiple pixels near laser center are plotted for laser irradiances and sample thickness of: (a) 35.7 W/cm^2 , 3.1 mm thick, (b) 35.7 W/cm^2 , 2.4 mm thick, (c) 35.7 W/cm^2 , 1.7 mm thick, (d) 63.7 W/cm^2 , 3.1 mm thick. 55

Fig. 12. Experimental set-up 61

Fig. 13. Dependence of average emissivity (ϵ) on wavelength (λ) for (from top to bottom at $5\text{ }\mu\text{m}$) fine graphite irradiated (♦), isomolded irradiated (►), medium irradiated

(●), fine unirradiated (+), isomolded unirradiated (★), medium unirradiated (■),
coarse irradiated (×) and coarse unirradiated(▲)..... 64

Fig. 14. Dependence of average spectral emissivity, ϵ_λ , at $\lambda=3.9 \mu\text{m}$ on sample surface
temperature, T_s for (●) medium, (▲) coarse, (×) fine, and (■) isomolded graphite
samples. 65

Fig. 15. (a) Surface temperature map and (b) vertical temperature profile (at arrow) of
isomolded graphite (7.62 cm x 7.62 cm x 1.27 cm) irradiated at 1500 W/cm² for 120
seconds (0.06, 0.2, 0.6, and 1.5 ms integration times. Temperatures above laser
center are reflected about the peak to illustrate symmetry (*). 67

Fig. 16. Temperatures at laser center during 120 second test at laser powers from 780-
3000 W/cm². Best labeling scheme? Isomolded graphite plates at 780 W/cm², 1000
W/cm², 1250 W/cm², 1500 W/cm², 1750 W/cm², 2000 W/cm², and 3000 W/cm².
Beginning and end of binder removal is labeled with *. 68

Fig. 17. Temperatures at laser center during 120 second test at laser powers of 1000
W/cm², 1500 W/cm², and 2000 W/cm² for isomolded (solid blue), medium (red --),
and coarse (-.-) porosities. 69

Fig. 18. The fraction of incident laser energy that is re-radiated from the graphite surface
peaks at 3350 K (1500 W/cm²). 70

Fig. 19. Temperature dependence of specific heat used in model. (*) Equation 1 (o)
Equation 2, and (—) composite equation 73

Fig. 20. Thermal conductivity temperature dependence (o) from reference [93], and (—)
power law fit 74

Fig. 21. Isomolded graphite comparison between measured (—) and modeled (-*-) temperatures at laser powers of 780 W/cm ² (*), 1000 W/cm ² (*), 1250 W/cm ² (*), 1500 W/cm ² (*), 1750 W/cm ² (*), 2000 W/cm ² (*), and 3000 W/cm ² (*) at (a) laser center during entire test and (b) vertical temperature profile through laser center at 21 seconds.	80
Fig. 22. Total actual (*) and modeled (•) graphite mass loss as a function of total energy deposited for (a) isomolded (b) medium and (c) coarse porosity.	82
Fig. 23. Testing Schematic.....	88
Fig. 24. Large panel cutting diagram. Resin is completely removed from black region above laser spot. Samples at the same distance from laser center are considered to be equivalent (i.e. L1 = R1, L2 = R2, etc.)	90
Fig. 25. MTS Testing Machine with sample.....	91
Fig. 26. Strips in order of (left to right) increasing irradiance (100, 150, 205, 291, 396, 450, and 520 W/cm ²). (a) Front side (b) Back side.....	92
Fig. 27. Large test panels at 85, 284, and 490 W/cm ² . Backside in inset. Markings are guidelines for cutting into testing strips (later widened strips, allowing only 4 to be cut).....	94
Fig. 28. Thermal image of flame jets (a) large panels at 490 W/cm ² after 6 seconds and (b) pre-cut strip at 520 W/cm ² after 1.6 seconds.....	95
Fig. 29. Pre-cut strip laser center temperatures at 100 W/cm ² (—), 152 W/cm ² (○), 205 W/cm ² (*), 296 W/cm ² (◇), 396 W/cm ² (□), 450 W/cm ² (×), 520 W/cm ² (△) ..	95

Fig. 30. Panel temperatures at 85 (—), 189 (○), 285 (*), 396 (◇), and 490 (□) W/cm ² at (a) laser center and (b) horizontal profile through laser center. Steady state temperatures increase with irradiance.	96
Fig. 31. Mass removed from thin strips as function of total energy deposited.	97
Fig. 32. Failure modes of CFRP. Undamaged material (a-c) failed dramatically in compression at 45° relative to applied stress. Test was terminated after sharp reduction (>90%) in sustained load. Heavily damaged material (d) failed gradually in brooming-type failure.	98
Fig. 33. Testing behavior of baseline (—), 130 W (---), and 500 W (●) strength testing samples.	98
Fig. 34. Ultimate compressive strength decreased with increasing laser power.	99
Fig. 35. Strength reduction away from laser center at 85 W/cm ² (○), 189 W/cm ² (+), 285 W/cm ² (*), 396 W/cm ² (□), and 490 W/cm ² (△).	100
Fig. 36. Relative amounts of decomposition phases at end of simulation: virgin resin (*), dehydrated resin (○), char (◆), and bare fiber (△).	102
Fig. 37. Proportions of resin, dehydrated resin, char, and bare fiber (columns a–d) remaining after 10 seconds irradiation at 100 W/cm ² (row 1) and 525 W/cm ² (row 2). At lower irradiance, a reaction front mirroring the laser spot is visible midway through the sample thickness. At high irradiance, all the virgin resin and dehydrated resin has decomposed, with a core of char and bare fiber on both faces.	103
Fig. 38. Telops IFTS imaging configuration. IFTS measurements were taken concurrently with FLIR surface temperature measurements (see schematic in Fig. 2), but for clarity those elements have been omitted here.	109

Fig. 39. Ignition times (a) and ignition time inverse (b) as a function of incident laser irradiance.....	110
Fig. 40. Ignition temperatures as a function of laser intensity.....	112
Fig. 41. The Telops MWIR IFTS imaged through the surface decomposition plume with the sample in profile (5 W/cm^2 laser coming from the left) as shown in the broadband image in part (a), with the highest intensity in front of the laser spot. Part (b) shows the FTIR spectrum at each pixel in a row at laser center, starting far in front of the sample and ending on the backside, with the highest intensity peaks from $1959\text{-}2337 \text{ cm}^{-1}$, $2677\text{-}3201 \text{ cm}^{-1}$, and $3600\text{-}3700 \text{ cm}^{-1}$ for several pixels near the surface.	113
Fig. 42. Illustration of peak area calculation. Calibrated spectra (—) in (a) are first smoothed (—) and the baseline (—) is fit to a polynomial before being removed. Peak areas (b) are then numerically integrated. The feature near 5000 cm^{-1} is an artifact of calibration, which is poor above 4000 cm^{-1}	114
Fig. 43. Maximum volatile peak areas and surface temperatures (T_s) at (a) 37 W/cm^2 and (b) 39 W/cm^2 . Peak areas from $2677\text{-}3201 \text{ cm}^{-1}$ are greatest (•), followed by peak areas from $1959\text{-}2337 \text{ cm}^{-1}$ (•), and peak areas from $3600\text{-}3700 \text{ cm}^{-1}$ (•).....	115
Fig. 44. Impact of the number of model elements in the thickness direction on front and backside laser center temperatures at 5 W/cm^2 with 4 (—•—), 8 (—), and 16 (—•—) elements.....	124
Fig. 45. Impact of the residual weight percent of char after decomposition on front and backside laser center temperatures at 5 W/cm^2 : 60% (—•—), 40% (—), and 20% (—•—).	124

Fig. 46. Impact of radiative cooling of bare fiber on front and backside laser center temperatures at 5 W/cm ² with $\epsilon = \epsilon(T) - 0.1$ (- · -), $\epsilon(T)$ (—), and $\epsilon(T) + 0.1$ (- - -).	125
Fig. 47. Impact of the resin dehydration reaction (a) activation energy [5% reduction (- - -), best fit (—), and 5% increase (- · -)], (b) pre-exponential factor [25% reduction (- - -), best fit (—), and 25% increase (- · -)], and (c) enthalpy of reaction [25% reduction (- - -), best fit (—), and 25% increase (- · -)] on front and back- side laser center temperatures at 5 W/cm ² .	125
Fig. 48. Impact of the dehydrated resin decomposition reaction (a) activation energy [10% reduction (- - -), best fit (—), and 10% increase (- · -)], (b) pre-exponential factor [25% reduction (- - -), best fit (—), and 25% increase (- · -)], and (c) enthalpy of reaction [25% reduction (- - -), best fit (—), and 25% increase (- · -)] on front and back- side laser center temperatures at 5 W/cm ² . The impact of dehydrated resin decomposition reaction (d) activation energy and (e) enthalpy of reaction on laser center temperatures at 10 W/cm ² is shown as well for 25% reduction (- - -), best fit (—), and 25% increase (- · -).	126
Fig. 49. Impact of the char oxidation reaction (a) activation energy [25% reduction (- - -), best fit (—), and 25% increase (- · -)], (b) pre-exponential factor [25% reduction (- - -), best fit (—), and 25% increase (- · -)], and (c) enthalpy of reaction [0.2 MJ/kg (- - -), none (—)] on front and back- side laser center temperatures at 5 W/cm ² .	127

Fig. 50. Impact of the laser absorptivity of (a) virgin resin [1.0 (— · —), 0.93 (—), and 0.85 (— · —)], (b) dehydrated resin [1.0 (— · —), 0.93 (—), and 0.85 (— · —)], (c) char 0.95 [(— · —), 0.98 (—), and 0.75 (— · —)], and (d) bare fiber [$\alpha + 0.1$ (— · —), $\alpha(T)$ (—), and $\alpha - 0.1$ (— · —)] on front and backside laser center temperatures at 5 W/cm². The effect is greatest when a given decomposition phase is most abundant. 128

Fig. 51. Impact of the thermal conductivity in the thickness direction of (a) virgin resin, (b) dehydrated resin, (c) char, and (d) bare fiber on front and backside laser center temperatures at 5 W/cm²: 25% reduction (— · —), best fit (—), and 25% increase (— · —). 129

Fig. 52. Impact of the thermal conductivity in the fiber/surface planar direction of (a) virgin resin, (b) dehydrated resin, (c) char, and (d) bare fiber on front and backside laser center temperatures at 5 W/cm²: 25% reduction (— · —), best fit (—), and 25% increase (— · —). 130

Fig. 53. Impact of the surface convection coefficient (hc) on front and back laser center temperatures at 5 W/cm²: 50% reduction (— · —), best fit (—), and 100% increase (— · —). 131

Fig. 54. Impact of graphite binder removal activation energy on front and backside laser center temperatures at 1500 W/cm² at varying deviations from best fit parameter: (a) 25% reduction (— · —), best fit (—), and 25% increase (— · —), (b) 10% reduction (— · —), best fit (—), and 10% increase (— · —), (c) 5% reduction (— · —), best fit (—), and 5% increase (— · —) 131

Fig. 55. Impact of the graphite binder removal pre-exponential factor on front and backside laser center temperatures at 1500 W/cm^2 for variations of (a) 25% reduction (---), best fit (—), and 25% increase (- · -) and (b) 90% reduction (---), best fit (—), and 1000% increase (- · -).	132
Fig. 56. Impact of the graphite conductivity on front and backside laser center temperatures at 1500 W/cm^2 for variations of (a) 25% reduction (---), best fit (—), and 25% increase (- · -).	132
Fig. 57. Impact of the percent graphite binder initially present on front and backside laser center temperatures at 1500 W/cm^2 for variations of (a) 20% binder (---), 40% binder (—), and 60% binder (- · -).	133
Fig. 58. Impact of the graphite absorptivity and emissivity ($\epsilon = \alpha$) on front and backside laser center temperatures at 1500 W/cm^2 for variations of (a) $\epsilon - 0.1$ (---), ϵ (—), and $\epsilon + 0.1$ (- · -).	133

List of Tables

Table	Page
Table 1. Summary of carbon fiber properties.	7
Table 2. Some Arrhenius constants reported in the literature for epoxy degradation. *IKP – Invariant Kinetic Parameter Method	15
Table 3. Thermal parameters derived in this work compared with prior studies.	53
Table 4. Kinetic parameters derived in this work compared with prior studies.	54
Table 5. Characteristic Surface Temperatures	70
Table 6. Graphite sample properties	72
Table 7. Model parameters	83

DEGRADATION OF CARBON FIBER REINFORCED POLYMER AND GRAPHITE BY LASER HEATING

I. Introduction

Laser weapon systems for strategic missions (missile defense) and tactical missions (point defense and gunship operations) generally rely on high power continuous wave lasers. In a strategic mission, a high power (>100 kW) beam is focused to a small spot size (< 10 cm) on a target to damage or destroy it within a dwell time of < 10 s [1, 2]. Laser systems this large have been pursued for decades without being fielded [3]. The availability of high power, diode pumped solid state and fiber lasers at lower powers (> 10 kW) and shorter wavelengths ($1.07\text{ }\mu\text{m}$) have recently invigorated the development of tactical laser weapons. This shift to tactical missions greatly increases the variety of potential target materials. As their use continues to grow, both in the number of applications and in weight percentage of new vehicles, the high energy laser (HEL) response of composite materials, including fiberglass, carbon fiber reinforced polymers, and related materials are of increasing interest [4, 5].

The HEL irradiation of composite materials is a complex process. Heating is dependent on many spectral- or temperature-dependent material properties, including absorbance, emissivity, thermal conductivity, heat capacity, and density. The material changes throughout the process, melting or decomposing into a complex mixture of volatile compounds and chars which can ignite at the surface. All of these variables

affect the heat distribution throughout the material and together dictate the response of the material. Modeling such a scenario is difficult and satisfactory results require many material-specific inputs for the relevant parameters.

This has historically driven HEL lethality testing towards reliance on data-anchored, empirical models; an approach that requires live-fire HEL testing of representative articles. With the wide variety of possible target materials, as well as different laser systems, engagement geometries, and other variables, the testing requirement with this approach is large.

A hybrid approach may be found using a high-speed thermal camera to record the detailed thermal response of a subset of laser experiments and fitting a simplified thermal model, along with readily available material properties, to estimate unknown properties. Monitoring the plume for spatial and temporal changes in gas concentrations also provides information about gas transport, ignition, and combustion. Once developed, the thermal model can be used to estimate a material's thermal response to untested scenarios and determine outcomes of interest from a lethality standpoint, such as residual strength and the extent of surface combustion.

In the current work, I demonstrate the potential of the adaptation of thermal imagery to the investigation of laser-material interactions. This required: (1) combining multiple integration times to extend the dynamic range of temperature measurement, (2) measurement of phase and temperature dependent surface emissivity, (3) incorporation of real-life laser profiles into thermal models, (4) thermal modeling to estimate the changing material thermal properties as a result of material degradation, and (5) thermal modeling to estimate of decomposition kinetics and heats of reaction.

The accomplishment of this work required collaboration with the Air Force Research Laboratory (AFRL), both the Laser Effects Branch (RDLE) at Kirtland Air Force Base (KAFB), NM and the Laser Hardened Materials Evaluation Laboratory (RXAP) at Wright-Patterson Air Force Base (WPAFB), OH. Their HEL facilities were used to produce and characterize the laser beams and they were instrumental in experimental set-up and recording. In both cases, thermal and hyper-spectral imagers were deployed from the Air Force Institute of Technology (AFIT).

Key contributions to the field are: (1) evolving spatial and temporal surface temperature maps of laser irradiated carbon fiber reinforced polymer (CFRP) and graphite with dynamic range > 3000 K, (2) measurement of evolving spectral emissivity of CFRP and porous graphite as a result of laser-induced decomposition, (3) estimation of decomposition kinetics and heats of reaction of CFRP and porous graphite during HEL irradiation from surface temperature modeling, (4) measurement of HEL-induced compressive strength reduction and estimate of intermediate decomposition phase compressive strength, and (5) characterization of surface ignition conditions during HEL irradiation.

Document Overview

Chapter II provides an introduction to the target materials considered here, including their production and final properties. Heating and decomposition of CFRP materials is covered in some depth, especially the kinetics and volatile products. The basics of radiometric temperature measurements and the method employed here are introduced, as well as the basis for their prediction via thermal models. Previous testing

of thermal strength degradation and the detection of volatile decomposition products via IFTS are introduced as well.

Chapters III and IV are devoted to the thermal modeling of the laser irradiation of a range of CFRP and graphite targets at widely varying laser powers. The purpose of these chapters is to demonstrate the utility of high quality thermal imagery in investigating laser-material interactions during HEL testing.

Chapter V investigates the effects of HEL exposure on the residual compressive strength of CFRP, both at the laser spot and as a function of distance from laser center. Refinements are made to the thermal model to account for surface flames and it is used to predict the resulting material composition and its impacts on measured residual strengths.

Chapter VI investigates the combined role of volatile concentrations near the surface and surface temperature in the ignition of surface flames during HEL exposure. Chapters III-V will be submitted for peer review and contain some redundant experimental details and background development.

Chapter VII summarizes conclusions and key results and offers some recommendations for future work.

II. Background

Introduction

The purpose of this chapter is to introduce the concepts necessary to understand the optical (radiometric) measurement of temperature and to familiarize the reader with CFRP and graphite samples and their interaction with a HEL.

Materials

Carbon Fiber Reinforced Polymers (CFRP)

The majority (over 90%) of carbon fibers are currently made from a polyacrylonitrile (PAN) fiber precursor [6]. PAN fibers start as a copolymer of acrylonitrile (85%) and a comonomer (usually methyl acrylate), with various processing additives. The copolymer (of correct composition and molecular weight) is then dissolved in the proper solvent (at the right concentration and temperature), injected (through the right size/shape hole) into a coagulation bath (of correct composition and temperature) and stretched (under the right conditions) to develop crystallinity and prevent shrinkage. The resulting properties of the carbon fibers depend heavily on these many variables (in addition to later steps), yielding a complex (and largely proprietary) process to optimize [8, 9].

Once formed, PAN fibers are thermally treated to form carbon fibers. There are three general steps: 1) stabilization, 2) carbonization, and 3) graphitization (optional). Stabilization is performed in air, at carefully controlled temperatures between 200 and 400 °C, with the fibers under tension. Over several hours, adjacent polymer chains crosslink with one another. This stabilizes the precursor structure, allowing it to survive

high temperatures in the carbonization step. Oxidizing the polymer chains also increases the process yield [8].

Carbonization is performed in an inert atmosphere, at temperatures ranging from 350 to 1700 °C. During this process, volatile small molecules (H₂O, HCN, NH₃, CO, CO₂, N₂, etc.) are released from the stabilized PAN fibers through condensation, cyclization, chain scission, dehydrogenation, and de-nitrogenation reactions. This eliminates most of the non-carbon elements, producing an interconnected network of hexagonal, graphite-like structures. During graphitization, fibers are heated to even higher temperatures (2500 °C) which increases the crystallinity along the fiber axis, resulting in improved mechanical properties [8].

A last step is to apply a surface treatment to the fibers to enhance the eventual bonding between the fiber and the matrix in a composite material, either through increasing the surface area of the fiber or enhancing their chemical interaction. The exact nature of the surface treatment is in many cases a trade secret, but is generally divided into oxidative treatments (gas-phase, chemical, electrochemical, catalytic) and non-oxidative treatments (carbon deposition, polymer grafting) [7, 9].

This results in a fiber that is greater than 90% carbon by weight, with general properties as summarized in Table 1 [6].

Carbon fibers have a graphite-like structure, with a similar hexagonal bonding pattern. However, in addition to not being fully graphitized, the layers are not planar and are more widely spaced, a form called turbostratic. These layers and the microdomains they form split, twist and fold among themselves to form a carbon fiber, usually less than 10 μm in diameter [7].

Table 1. Summary of carbon fiber properties.

Property	Value
Tensile Strength	High (2-7 GPa)
Compressive Strength	Good (< 3 GPa)
Tensile Modulus	High (200-900 GPa)
Density	Low (1.75-2.18 g/cm ³)
Temperature Resistance	Good
Thermal Expansion	Low
Electrical/Thermal Conductivity	High
Chemical Resistance	Good

Pores exist within the carbon fiber, but are generally inaccessible at room temperature. During carbonization, they initially form to allow the removal of volatiles but close at higher temperatures present in later stages of the process. Some carbon fibers also exhibit a skin-core structure, with differing moduli and coefficients of thermal expansion across their boundary [7].

Epoxy resins are the most commonly used matrix material in CFRPs due to their exceptional mechanical performance at higher temperatures (up to 130 °C), good solvent resistance, low curing shrinkage, and compatibility with carbon fibers. Epoxies satisfy upwards of 85% of CFRP applications (including military aircraft) except where low smoke/flammability or exceptional temperature resistance (above 130 °C) is required [9].

Epoxy is a general term that refers to the three-membered epoxy ring. Epoxy resins are relatively short ($n = 0-3$) straight chained molecules with an epoxy ring on both ends. The chemical structure between the epoxy rings can vary. A very common epoxy resin is diglycidyl ether of Bisphenol A (DGEBA) [10]. In most cases, epoxies are cured through reaction of the epoxy ring with an amine or anhydride hardener (though other

methods exist). Hardener molecules have multiple places where they can react with an epoxy ring. In this way, they form cross-links to lock the epoxy molecules in place and produce a solid material. The hardener is not a catalyst - enough is needed to satisfy the reaction stoichiometry and it forms a significant portion of the cured resin. The optimization of the final material properties depends on the choice of resin and curative (of which there are many), their stoichiometry, as well as any additives [11]. As such, the exact recipe used in commercial products is generally a trade secret.

Bare carbon fibers and unmixed epoxy resin/hardener are generally not used by high performance CFRP part manufacturers. They instead commonly rely on prepregs, a precise combination of unidirectional or woven carbon fibers and pre-formulated resin manufactured into a tape or fabric sheet. The resin contents and tape widths and thicknesses are standardized, but can be varied. The resin is partially cured, requiring a final cure after part lay-up at elevated temperatures in an oven or autoclave. Prepregs offer significant advantages, including the ability to handle unidirectional fiber arrays, predetermined fiber to resin ratio and total weight, no mixing or chemical handling, long pot life, and easier quality control [9]. This makes them attractive for large and complicated part lay-ups. It is also possible to lay-up bare fibers and inject resin under vacuum, which is the method used for the samples tested in this work.

Graphite

Pure graphite is an allotrope of carbon with a hexagonal planar crystal structure. Each carbon atom is sp^2 hybridized and forms three strong bonds (524 kJ/mol, 1.41 Å bond length) with its nearest neighbors in the plane. Hexagonal planes stack on top of

each other but are only weakly bonded via van der Waal forces (7 kJ/mol, 3.35 Å bond length).

Graphite is present in natural deposits but most graphite used commercially is synthetic in nature. Synthetic graphite commonly starts as a blend of (carbon rich) coke and binder (pitch or tar) that is formed into shape via isostatic pressing (yielding relatively isotropic properties) or extrusion molding (producing anisotropic properties). The first stage of heat treatment is carbonization at temperatures of 700-1200 °C to crack and polymerize the binder, slowly releasing impurities and volatiles (approximately 65% binder mass remaining). Production of high density ($>1.7 \text{ g/cm}^3$) graphite requires that the resulting pores be impregnated with additional binder under vacuum and re-carbonized. The final step is graphitization, where the graphite is heated to temperatures in the range of 2500-3000 °C. During graphitization, additional impurities are removed and carbon atoms are energetic enough to re-organize to remove crystal imperfections, grow crystalline regions, remove cross-links, and form graphitic planar stacking. At higher temperatures, the graphitization process is more rapid (several hours at 3000 °C) and complete.

The resulting graphite is very thermally and electrically conductive (similar to metals), has good chemical stability, low thermal expansion, and excellent thermal shock resistance. Its high-temperature strength and tolerance of radiation also make it particularly well suited for use in nuclear reactors. [13, 14]

Laser Material Interactions

Material absorbance of incident radiation varies with wavelength. At 1.07 μm , epoxy resins are highly transmitting. In CFRP, the epoxy absorption depth is much longer than the epoxy thickness between fiber layers [15, 16]. Conversely, the absorbance of the carbon fibers is very high (0.8-0.9) near 1.07 μm and increases gradually with increasing temperature [16]. Under irradiation by a high energy laser near 1.07 μm , most of the energy will be absorbed by the first fiber layer. It will then flow via conduction to the surrounding CFRP material.

Heat flow in a CFRP is dependent on the thermal conductivities of both the polymer matrix ($0.2 - 1.0 \text{ W m}^{-1} \text{ K}^{-1}$) and carbon fibers ($6.8 - 176 \text{ W m}^{-1} \text{ K}^{-1}$) [18–20]. Thermal conductivities for carbon fibers vary widely based on precursor material (PAN-based fibers are generally less conductive than pitch-based fibers [17]) and somewhat less as a result of the many variables of the manufacturing process. Because of the wide disparity between the thermal conductivity of its constituent parts, CFRPs exhibit highly anisotropic heat conduction. In the direction parallel to the fibers, heat conduction is on the order of 30-50 times faster than in the perpendicular direction [19, 20]. In a multi-ply CFRP, the relative angles of the plies have little effect on the perpendicular heat conduction [20]. Off-fiber-axis conduction within a single ply varies as a function of angle with the fibers, from a minimum in the perpendicular direction to a maximum in the parallel direction [18]. As a result, fiber layers experience significant heating outside of the laser spot and a thermal gradient exists between the front and backside of a CFRP panel.

Under one-sided irradiation, a CFRP panel will experience more rapid front-side heating and will reach hotter front-side steady-state temperatures than the back of the panel. At irradiance levels representative of exposure to a fire ($3\text{-}5\text{ W/cm}^2$), front side temperatures reach $550\text{-}650\text{ }^{\circ}\text{C}$ with a corresponding backside temperature approximately $100\text{ }^{\circ}\text{C}$ less [21]. The ultimate temperature of the CFRP panel is dependent on the irradiance level and reaches a steady-state temperature when energy loss mechanisms equalize the absorption of incident radiation. Initial heating rates also increase with increasing irradiance.

Of the two components, the epoxy matrix is far more thermally sensitive. The thermal response of cured epoxy resins has several stages. In the earliest stage, it thermally softens near its glass transition temperature (approximately $120\text{ }^{\circ}\text{C}$). In the first degradation stage ($250\text{-}300\text{ }^{\circ}\text{C}$), water is eliminated through a dehydration process, forming double bonds in the polymer structure. Next the epoxy begins to decompose as a result of random chain scission ($300\text{-}450\text{ }^{\circ}\text{C}$). The weakest bonds are broken first, which are generally the C-N bonds for amine-cured epoxies [10]. At this stage, multiple competing degradation pathways are possible, resulting in many different degradation fragments. A carbonaceous material (char) is left behind, which oxidizes in air.

Several studies have worked to identify the major volatile products from the decomposition of basic epoxy formulations [23, 24]. In these experiments, epoxy samples are heated at a constant rate through decomposition and various means (Subambient Thermal Volatilization Analysis or Gas/Liquid Chromatography) are used to separate their constituents before identifying them using infrared spectroscopy or mass spectrometry. The major constituents are generally found to be bisphenol A (40-50%),

phenol (5%), isopropenylphenol (5%), low boiling pyrolyzates (hydrogen, methane, ethane, propene – 10%), compounds related to the curing agent (10-15%), and all others (20-25%, structure closely related to preceding). The effect of very high heating rates on the identity and relative populations of these volatile products is unknown, as is the effect of their passage through a hot carbon fiber network as they exit the material.

The initial stages of epoxy degradation (up to approximately 40% weight loss) are not affected by the environment, whether air or nitrogen. After this point, the rate of thermal degradation slows. In nitrogen, the slowing continues and reaches a quasi-steady state at a low residual value (volatiles having been exhausted and only char remaining). The amount of residue left decreases as heating rate increases [24]. However, when oxygen is present, a thermo-oxidative process activates, oxidizing the remaining char until the polymer is completely consumed.

Carbon fiber is much more thermally resistant than the epoxy matrix. In both air and nitrogen environments, a small initial loss (300-500 °C) due to the decomposition of the organic sizing compound on the fiber is observed. In nitrogen, the fibers decompose no further. However, in air the fibers oxidize beginning around 500 °C, eventually completely oxidizing with no residual mass [21]. In the case of a composite, it follows that oxidation would be most active on surface fibers. Oxygen access to interior carbon fibers in a rapidly decomposing epoxy matrix composite is unknown, but would presumably be limited by the consumption of oxygen by surface reactions and the outflow of volatile epoxy decomposition products.

Epoxy Decomposition Kinetics

The nature of the epoxy decomposition reaction is commonly studied using Thermogravimetric Analysis (TGA). In TGA, the weights of small samples are recorded while being heated at a controlled (usually linear) rate. Because the samples are small and the heating rates are slow (with experiments taking several hours), the whole sample progresses through the degradation process simultaneously. As the temperature increases, the polymers degrade, releasing volatile molecular fragments that reduce the mass. From the mass-loss profile the number of distinct reactions, their characteristic temperatures, and associated (Arrhenius) kinetic constants can be determined. It is generally recommended to use data obtained at multiple heating rates in calculating Arrhenius constants (A , E_a and n). Using data from a single non-isothermal experiment can create confusion because the data can often be equally described by multiple sets of kinetic triplets (A , E_a , and n). Care must also be taken to select an appropriate kinetic model [25].

These difficulties are mitigated somewhat by alternative methods, called isoconversional methods, that remove the dependence of reaction rate on how much material has reacted. Instead of plotting mass loss vs. temperature, isoconversional methods plot α , degree of conversion. This produces an isoconversional activation energy, E_α , that is constant with temperature, but may change at different α . If it does, it indicates that the reaction being considered is a multistep process [25]. Careful analysis of epoxy degradation in this way reveals that the degradation process is very complex. In fact, Budrugaec and Segal [26] find that the epoxy decomposition actually consists of

three thermo-oxidative processes and the first degradation step is itself complex, consisting of four sub-steps, each with its own Arrhenius constants and functional form.

When heated very slowly, the complexity of the degradation reaction reveals itself. However, as the heating rate increases, the TGA trace changes. Kandare et al [27] find that when the heating rate (in air) of a glass fiber reinforced epoxy is increased from 10 °C/min to 200 °C/min, the decomposition occurs at higher temperatures (peak rate at 430 °C vs. 368 °C) and the degradation mechanism appears to simplify, transitioning from a two-stage to a one-stage pathway. This is significant in the context of fire exposure because the heating rate at the exposed surface is very high (200-300 °C/min) and decreases at locations further from the surface. In an HEL scenario, the heating rates near the surface are many times faster still (700-20k °C/min). Extrapolating the increase in decomposition temperature seen from increasing the heating rate from 10 °C/min to 200 °C/min to the much higher rate of 20k °C/min suggests the possibility of a much higher decomposition temperature (and the justified use of a single-stage reaction). However, the exact behavior of this effect is unknown, as are the appropriate Arrhenius kinetics at such a high heating rate. TGA, the mainstay of these experiments, is unable to achieve these high heating rates. Even if it could, the low thermal conductivities of many polymers would cause a thermal gradient to develop within the sample and the average sample temperature could not keep up with the TGA furnace. This can be mitigated to a degree by ensuring good thermal contact between the sample and its holder (by using sample powders, pellets, or thin films). The sample temperature is also affected by the degradation process itself (endothermic for epoxies), an effect that increases at higher heating rates [25].

Many traditional TGA studies have been done on the thermal degradation of epoxies. However, the kinetic parameters generated vary considerably. Though not advised, many of them have fit Arrhenius constants to one non-isothermal TGA experiment at a single heating rate (permitting a variety of kinetic constants). Even when iso-conversional methods are used, researchers differ as to the appropriate kinetic mechanism to use for the reaction. Some of the varying results are shown in Table 2. Heating rates for these experiments are generally less than 20 °C/min.

Table 2. Some Arrhenius constants reported in the literature for epoxy degradation. *IKP – Invariant Kinetic Parameter Method

Ref	k(T)	A (s ⁻¹)	E _a (kJ/mol)	n	Notes
[24]	A exp(-E _a /RT) (1-α) ⁿ	8.92 x 10 ¹²	172.6	0.4	N ₂
[28]	A exp(-E _a /RT) *(0.23(1-α) ⁿ +0.87α ⁿ)	19.9	128 ± 3	2/3	*IKP
[29]	A exp(-E _a /RT) α ⁻¹	1.12 x 10 ⁹ 1.35 x 10 ⁸	149 ± 4 134 ± 8	- -	*IKP
[30]	A exp(-E _a /RT) m	8.08 x 10 ⁴	92.3	-	-

Another departure from typical TGA experiments present in HEL scenarios is the application of constant radiant heat flux instead of constant heating rate. At a constant heat flux, the sample is heated rapidly and reaches a steady state temperature that depends on irradiance.

TGA, such as it is, is the standard in polymer thermal analysis and provides important insight into HEL material response. However, it does not adequately address two aspects of HEL irradiation of CRFP: (1) very high heating rates and surface temperatures and (2) the role of the carbon fibers. Because the fibers are the dominant absorbers of radiation at 1.07 μm, energy continues to couple into the material near the

front surface (in one-sided heating) even after the thermal decomposition front has moved further into the material (via conduction).

Radiometric Temperature Measurement

All objects with a temperature above absolute zero emit radiation. The maximum energy per unit time per area at a given wavelength that an object at a given temperature can emit is given by Planck's law:

$$M(\lambda, T) = \frac{2\pi hc^2}{\lambda^5 \left[e^{\frac{hc}{\lambda kT}} - 1 \right]} \left[\frac{W}{cm^2 \mu m} \right] \quad (1)$$

where h is Planck's constant, c is the speed of light, λ is wavelength, k is the Boltzmann constant, and T is temperature. This relationship underlies all measurement of temperature via emitted radiation.

Planck's law is derived classically by determining the density of modes within a cavity using the wave equation and the energy in each mode using the Boltzmann probability distribution. A key breakthrough of the early 20th century (and for Planck) was the realization that the energy of each mode must be quantized (rather than along a continuum) in integer multiples of $h\nu$, with each multiple called a photon of frequency ν [31].

An object that emits maximally at all wavelengths according to Eq. 1 is called a blackbody. Blackbody emitters are commonly produced by creating a closed cavity (of any shape as long as its dimensions are much larger than the wavelengths of interest) at a fixed temperature with a small hole. Blackbody radiation is a theoretical upper limit and only closely achieved for carefully designed and controlled conditions [32]. The emission spectra of all other objects are bounded by the blackbody curve. The degree to

which the spectrum for a given emitter approaches the blackbody maximum at each wavelength is described by a dimensionless number between 0 and 1 called emissivity, $\epsilon(\lambda)$. If emissivity is constant for all wavelengths, the object is referred to as a graybody. Graybodies have the same spectral shape as the corresponding blackbody, scaled by the emissivity. Integrating Eq. 1 over all wavelengths yields the Stefan-Boltzmann law (Eq. 2) that describes the total energy emitted per unit time per area by a blackbody at a given temperature. Emissivity scales the total exitance of a graybody (Eq. 2) as well.

$$M = \epsilon \sigma T^4 \quad \sigma = 5.67 \times 10^{-12} \text{ W}/(\text{cm}^2 \text{ K}^4) \quad (2)$$

Real sources are not typically described well as either a blackbody or a graybody. These are called selective emitters and have emissivities that vary continuously as a function of wavelength (and often temperature as well). In this case, knowledge of emissivity over the detector bandwidth is the most important factor is measuring temperature via radiation [32].

Conservation of energy requires that all energy incident on a surface is either absorbed, reflected or transmitted. For opaque surfaces, transmission is zero leaving all energy to be either absorbed or reflected. Under conditions of local thermal equilibrium, the energy absorbed must equal the energy emitted. This principal is called Kirchoff's law, which holds for total (spectrally integrated, $\alpha = \epsilon$) and spectral emissivity and absorptance ($\alpha(\lambda) = \epsilon(\lambda)$). As a result, surfaces that are highly absorbing are also highly emitting. However, in the case of selective emitters, it cannot be assumed in all cases that the absorptance at one wavelength will equal the emissivity at another.

Application of these principles allow careful measurements of emitted radiation over a spectral band to be used to measure surface temperature. In this work, a mid-wave

infrared (MWIR) thermal camera (FLIR SC6000) with a band-pass filter is used to measure the radiation emitted from a surface over the wavelength band from 3.8-4.0 μm . This produces an instrument response (in counts) that is calibrated to produce an equivalent blackbody temperature using predetermined relationships between flux (counts/sec) and integrated radiance (from 3.8-4.0 μm) and an inversion of Planck's law (Eq. 1) at the center wavelength. Relationships between flux and radiance are determined from imagery of a wide-area blackbody calibration source at known temperatures. These blackbody temperatures can be adjusted to include the effect of emissivity (at 3.9 μm) by multiplying radiance by ϵ before converting to temperature.

It should also be noted that the InSb detector in this particular model of thermal camera suffered from a non-linear response at low signal counts (approximately 2200-5000 counts). This nonlinearity was well characterized using the response at a wide range of integration times to a known temperature calibration blackbody and defining functional relationships between the actual response and the expected linear response that were used to "linearize" data at low signal counts before calibration to temperature.

Several publications have recently applied these principles in the investigation of the HEL irradiation of fused silica and other materials in a manner similar to this work [34–36]. In these studies, a CO_2 laser at 10.6 μm was used to heat pristine fused silica surfaces over a small area (250-1000 μm spot diameter) at irradiances of 0.13-16 kW/cm^2 . They measure surface temperatures spatially with a thermal camera at 8.9 μm and correct with measured emissivity. From steady-state temperatures, they deduce the effective thermal conductivity of silica assuming conductive losses only. For other

materials, they determine non-linear conductivity of the form $k(T) = A \times T^b$, with A and b as fit parameters. In other work, similar techniques are used to estimate the evaporation kinetics of fused silica near its boiling point of ~ 3000 K under the influence of gas flow. In these cases, the laser and imaging wavelengths were chosen to complement the sample material properties and allow radiative cooling to be neglected. This allows simplified analytical and semi-analytic solutions to the heat transfer equation.

Previous work investigating the response of CFRP to a $1.07 \mu\text{m}$ HEL primarily recorded precise CFRP penetration times as a function of surface irradiance with less importance placed on measuring surface temperatures [36]. CFRP penetration requires burning through the fiber layers and was conducted with thinner samples and at the high ($200\text{--}1500 \text{ W/cm}^2$) irradiances necessary to produce significant carbon fiber oxidation and sublimation. At these irradiances, the polymer matters little, as it will be completely cooked out of a thin sample in less than a second. However, matrix decomposition is achieved with much less power on target and can have significant material effects. The nature of HEL-induced matrix decomposition can also be investigated by surface temperature maps at high frame rates combined with appropriate modeling.

Thermal Modeling

Many attempts have been made to model the thermal response of composite materials to fire, generally at surface fluxes of $2\text{--}15 \text{ W/cm}^2$ with a maximum of about 30 W/cm^2 [10]. Models have incorporated many physical processes, including transient heat conduction, pyrolysis, flow of reaction volatiles, char formation, internal pressures, delamination cracking, thermal expansion/contraction, and surface combustion [38–40].

Varying levels of effort have been devoted to accurately determining thermal properties (conductivity, heat capacity, density) as a function of temperature or decomposition phase.

The basis for many models was developed in the 1980s by Henderson et al. [37]. Their 1D model incorporates conduction with temperature- and decomposition-dependent thermal conductivity, internal convection due to outflow of volatile decomposition gases, and the heat of decomposition. Surface convection and radiation are also considered. Decomposition kinetics are modeled using an Arrhenius equation with constants that are derived from an iso-conversional kinetic study [40]. Several sets of Arrhenius constants are used as the experiment progresses - one for early polymer degradation, one for late, and one for glass-silica reactions. They achieve good agreement with experimental results, irradiating a glass/phenolic composite at 28 W/cm^2 for 800 seconds).

Henderson devotes much effort to acquiring accurate temperature dependent thermal properties. This is necessary because models to calculate the non-linear temperature dependence of the heat capacity and conductivity are in general not available; polynomials are fit to experimental data instead [10]. However, composite thermal properties can be calculated based on the rule of mixtures, the relative amounts of matrix, fiber, and char, and their component properties.

The Henderson model appears to be a good balance of accuracy and complexity. Other efforts have simplified the model by neglecting the thermal property temperature dependence and assuming a one-step first order Arrhenius decomposition, with good agreement [11, 42]. Some have added processes, including thermal expansion and internal pressure rise, not improving the agreement with experimental temperatures [42],

but permitting additional predictions (porosity, expansion). Along these lines, several recent modeling efforts have focused on the role of internal gas production to predict fracture and delamination and the prediction of volatile gas ignition and surface heating due to combustion [39, 40].

However, deficiencies still exist in the modeling of composite responses to fire in the area of experimental validation (few experiments), the modeling of sandwich composites [10], and the determination of appropriate model parameters [39]. Many of these modeling efforts are also one-dimensional models due to the wide area surface fluxes typical of fire scenarios which is not reflective of focused laser spots. Finally, difficulties with thermocouple surface temperature measurement are cited as motivating a preference a non-contact temperature measurement method.

In addition, the heating rates are much higher for the front surface (even more so for HEL irradiation) than the back surface, with a continuum of heating rates through the interior of the material. Several critical processes (decomposition temperature and rate, volatile formation rate) are heating rate dependent. These processes affect many of the other processes that go on during composite heating and decomposition. The dependence on the heating rate only becomes more important as the heating rate increases further, as in a HEL scenario.

Despite this, models of composite material response to surface heating have been shown to agree quite well with observed temperatures and permit useful predictions to be made. Of particular interest to both the fire science and high-energy laser communities are predictions of residual strength and surface ignition.

The post-fire mechanical properties of composites are modeled quite well using a simple two-layer, matrix-char model [43]. Here, it is assumed that delaminations due to high internal gas pressures are negligible, the decomposition region is small and conversion to char is the dominant weakening mechanism. The change in mechanical properties (σ_t) is then proportional to the extent of char formation (d_c) according to Eq. 3. Because it is generally much smaller, char strength (σ_c) can often be neglected. Despite its simplicity, the two-layer model shows good agreement with experimental data [10].

$$\sigma_t = \left(\frac{d-d_c}{d}\right) \sigma_0 + \left(\frac{d_c}{d}\right) \sigma_c \quad (3)$$

Eq. 3 is the one-dimensional form, with d and σ_0 referring to the original composite thickness and strength, respectively.

Predicting ignition requires the estimation of the instantaneous mass flux of volatiles from the composite surface. McCarthy et al [39] use an improvised volatile diffusion equation (Eq. 4) with the pressure gradient replaced by the temperature gradient:

$$\frac{dm_{vol}(x,t)}{dt} = -\beta_T \rho (1 - f_{char}) \frac{\delta T}{\delta x} \quad (4)$$

where m_{vol} is the mass of volatile decomposition products, β_T is the thermal mass transfer coefficient, ρ is the composite density, $(1-f_{char})$ is the proportion of volatiles being formed, and $\frac{\delta T}{\delta x}$ is the thermal gradient. McCarthy's analysis is somewhat limited for lack of an experimental β_T value for the decomposition of epoxy resin. It is also assumed that the only volatile produced is methane, an assumption that is clearly wrong, but allows volume, density, and heat capacity to be calculated.

Strength Testing

Most of the work done on mechanical properties of composite materials at high temperatures focuses on their performance at elevated temperatures (leading to failure during active fires) rather than their residual, post-fire mechanical properties. The work that has been done shows that the post-fire strengths of carbon/epoxy composites are very poor due to the rapid thermal decomposition and high flammability of the epoxy matrix [10]. Perin et al [44] find that exposure to even moderately high temperatures (540 °C) can reduce post-fire tensile strengths to negligible levels after only approximately 30 seconds. This reduction is due to decomposition of the polymer matrix to form volatile gases (which escape) and char (less than 10% by weight) which has very low mechanical properties (especially in compression).

The tensile and compressive strengths of the polymer matrix decrease rapidly with increasing temperature near the glass transition temperature (T_g) [46, 47]. The epoxies used in CFRPs have a T_g around 128 °C [47]. As temperature increases, any tensile loads carried by a CFRP material are transferred to the fibers alone. However, because compressive strength is a matrix-dominated property, softening and decomposition of the epoxy causes drastic reductions in CFRP compressive strength. If the resin remains below the decomposition temperature, the matrix will re-solidify when cooled below the T_g . Beyond matrix decomposition, it is generally assumed that the matrix has no residual strength [45].

There is some disagreement in the literature regarding the impact of temperature on carbon fiber tensile strength. Sauder et al heat single carbon fibers electrically in a vacuum ($<10^{-3}$ Pa) while performing mechanical tensile testing [49, 50]. They find that

for a PAN-based fiber, modulus decreases with increasing temperature (starting around 1000 °C) but remains constant at temperatures < 1000 °C and that fiber strength actually increases as temperature increases, reaching a maximum around 1800 °C.

Feih and Mouritz use the finding of Sauder et al. that carbon fiber strength and modulus is constant up to 900 °C to justify performing fiber mechanical tests at room temperature (due to experimental difficulties) after heat treating [47]. They heat treat fibers at temperatures of 250 °C up to 700 °C for up to 4 hours before cooling and testing. For these extended temperature exposures, they see strength reductions of approximately 40%, for fibers in both air and nitrogen (with reduced diameter of oxidized fiber accounted for).

Feih and Mouritz also perform time-to-failure tests on cured carbon-epoxy laminate coupons (560mm long, 50 mm wide, 4.3 mm thick) under combined tensile loading and one-sided heating (3.5 or 5 W/cm²). The results show that the laminates retain significant residual tensile strength even after the matrix has totally decomposed (load carried by the fibers). If the applied stress is below a threshold level, failure does not occur [47]. The threshold level is about 50% and 35% of the original ultimate strength for the 3.5 W/cm² and 5 W/cm² case, respectively.

Feih and Mouritz also report a decrease in fiber modulus (in air) with increasing temperature. Oxidation occurs at the surface of the fiber, reducing its diameter. This causes an initial reduction in the elastic modulus of the fiber due to the uniform erosion of the outer layer of the carbon fiber (which is 40% stiffer than the core). Modulus is unchanged when heated in an inert environment. In a heated CFRP material, oxidation is

limited to surface fibers only, as intact fiber layers and out-gassing volatiles from the decomposing matrix limits air access to interior fiber layers [47].

Fourier Transform Spectroscopy

As previously stated, many of the volatile products from epoxy thermal decomposition have been identified. In an HEL scenario, these compounds are produced from decomposing epoxy at 300-500 °C and pass through hot carbon fiber layers as they exit the CFRP material. As these hydrocarbon products generally have auto-ignition temperatures ranging from 500-600 °C, it can be seen that if they are produced at a high enough rate, combustion is likely.

However, the nature of their production during composite surface heating is not well understood. A technique that can be used to detect and track the accumulation of these volatiles is an imaging Fourier Transform Spectrometry (IFTS). IFTS uses the detailed interference pattern of different wavelengths of incoming light in a Michelson interferometer (after undergoing a Fourier transform) to produce an emission spectrum (from 1.5-5 μm for an InSb detector array) at each pixel in a scene. The spectral signatures of different gases can be used to detect and (if the cross-section database exists) quantify the amount present. In recent years, the Telops Hyper-Cam, an IFTS spectrometer, has been used to analyze the constituents of industrial smokestacks [50], jet engine exhaust plumes [51], chemical plumes [52], natural gas flare emissions [53], and HEL material degradation plumes (fiberglass [4], polymethyl methacrylate (PMMA) [54], and graphite [55]). IFTS also makes possible the investigation of dynamics within the gas plumes and determination of mass flow rates and dispersion.

Fig. 1 presents gas-phase infrared spectra for many of the major expected volatile degradation products. In the MWIR, these volatile compounds have peaks generally centered around 3000 cm^{-1} resulting from C-H bond stretching and those around 3700 cm^{-1} due to phenolic O-H stretching. Due to the structural similarities, many of the volatile fragments have similar spectra. These peaks could potentially be used to detect and track the accumulation of volatiles during a HEL experiment. However, cross section databases generally only exist for small, common molecules like CO, CO₂, and H₂O, among others.

In the following chapters, emissivity-corrected surface temperatures of CFRP and graphite samples under HEL irradiation are measured and used, along with a simple thermal model, to estimate changing thermal properties and kinetic parameters during laser-induced thermal decomposition. The residual ultimate compressive strength of CFRP as a function of laser irradiance and distance from laser center is also measured, as well as the surface conditions necessary for ignition of volatile decomposition products.

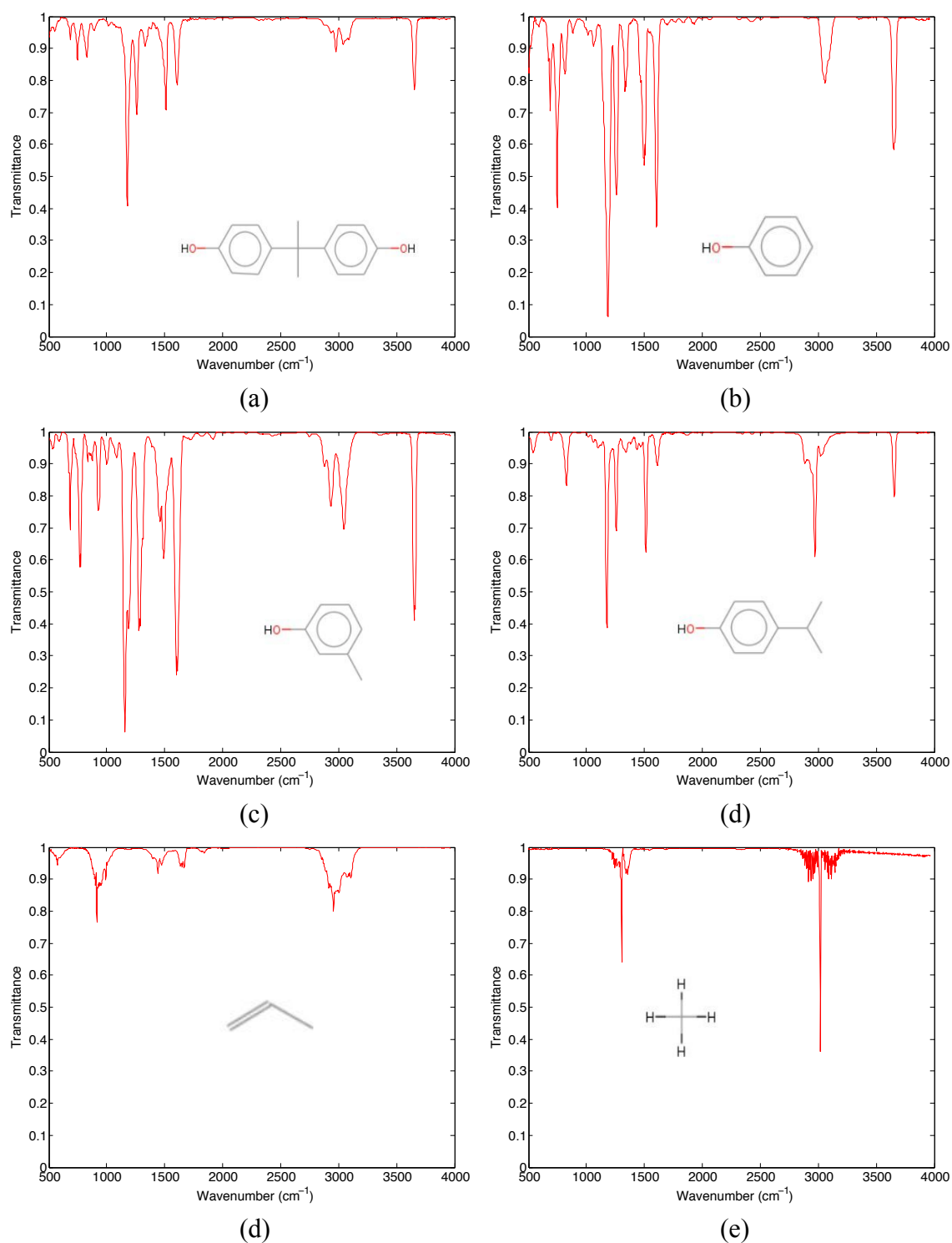


Fig. 1. Gas-phase Infrared Spectra of Volatile Degradation Products [56]. (a) Bisphenol A (b) Phenol (c) m-Cresol (d) 4-Isopropylphenol (e) Propene (f) Methane

III. Thermal Imagery and Modeling of Laser Irradiated Carbon Fiber Composite

The evolving front and backside surface temperatures from laser-irradiated carbon fiber reinforced polymer (CFRP) were measured using a 60-Hz mid-wave infrared (MWIR) camera. Woven carbon fiber-epoxy panels of 1.7-, 2.4-, and 3.1-mm thickness were irradiated with a 1.07- μm , 2-kW ytterbium fiber laser at irradiances of 5-64 W/cm^2 . Temperatures were calibrated using measured emissivity of pre-irradiated and damaged samples. A 3D, explicit finite difference, thermal model based on Fourier's heat diffusion equation with Neumann boundary conditions for laser absorption, surface emission, and convection was used to estimate Arrhenius kinetic rate parameters for a two-step epoxy decomposition reaction and a single stage char oxidation reaction for heating rates of 20-700 $^{\circ}\text{C}/\text{sec}$. Enthalpies and thermal properties of the decomposition stages are estimated.

Introduction

The fielding of tactical high-energy laser (HEL) weapon systems and the proliferation of fiber lasers greatly expands the possible target materials in future laser engagements [1, 57]. Testing many different combinations of materials, lasers systems, engagement geometries and environments, and other variables of laser-material interaction to predict engagement outcomes is impractical. Accurately modeling the laser-material interaction is dependent on the spectral, thermal, and phase-dependent material properties under conditions produced by a HEL. A hybrid approach may be found using a high-speed thermal camera to record the detailed thermal response of a subset of laser experiments and fitting a simplified thermal model, along with readily available material properties, to estimate unknown properties.

The use of carbon fiber reinforced polymer (CFRP) is increasing rapidly in many aerospace, military, and automotive applications [58]. CFRP is a structural composite made of layers of carbon fiber or woven carbon fiber cloth held in place by a thermoset resin (usually epoxy) matrix. The thermal conductivity of CFRP is highly anisotropic due to much higher thermal conductivity along the fiber [17], resulting in heat conduction in the fiber direction being on the order of 30-50 times faster than in the perpendicular direction [18, 20]. At 1.07 μm , the epoxy matrix is highly transmitting and carbon fiber is high absorbing [3], resulting in laser absorption primarily into the first fiber layer followed by conduction to the surrounding epoxy [59]. Cured epoxy softens (120 °C) and dehydrates (250-300 °C) before decomposing via random chain scission (300-450 °C) to produce volatile fragments and char [10]. In air, char and fibers oxidize rapidly above 600 °C and completely consume the fiber, given enough time and oxygen (3 hours at 650 °C) [21]. In inert environments, carbon fibers survive intact to temperatures as high as 2900 °C [60]. In a HEL scenario, CFRPs require very high irradiance to achieve burn through of the thermally resistant carbon fibers but much less to decompose the epoxy resin [36]. Resin decomposition can have damaging effects due to fouling and combustion of volatiles on both interior and exterior panel surfaces and significant reductions in CFRP compressive strength [46].

The stages and kinetics of the thermal decomposition of epoxy resins are well studied at low heating rates (typical < 50 °C/min) using Thermogravimetric Analysis (TGA) [25, 27–30]. At these rates, TGA experiments indicate that decomposition kinetics exhibit a heating rate dependence. Kandare et al. [27] find that the

decomposition temperature of a fiberglass/epoxy composite increases from 368 °C to 430 °C when heating rate is increased from 10 to 200 °C/min and the degradation mechanism simplifies from two stages to one. HELs produce very much higher heating rates (>500 °C/sec) that cannot be studied by TGA and yet may affect decomposition kinetics.

Cured epoxy contains a high concentration of hydrogen-bonded hydroxyl groups that dehydrate to form water and double (C=C) bonds. When heated further bonds within the polymer network begin to break. Many different reaction pathways are possible which leads to product fragments of widely varying size and identity. Weaker bonds are broken first, eventually leaving a residual porous carbon network (char) which oxidizes in air to form CO and CO₂ [22]. Carbon fibers oxidize as well but slowly enough to be considered inert in these experiments [21].

Description of the thermal response of composite materials primarily build on the Henderson model, which includes conduction, volatile convection, and enthalpy of decomposition effects [11, 38]. Kinetics are represented by nth order Arrhenius reactions with one or more steps. Boundary conditions generally account for convection and radiation. Input material properties are usually phase specific with varying degrees of attention paid to temperature dependence. Extensions to the Henderson model are made in efforts to model additional effects including material expansion, volatile combustion, and damage due to internal gas pressure [39, 40, 63]. Temperature measurements are typically limited to thermocouple measurements at a small number of locations with typical response times of several seconds.

This work uses thermal imagery to observe CFRP front and back surface temperatures and extract phase-specific material properties and kinetic parameters as the

samples progress through epoxy decomposition. The decomposition at heating rates of 12 – 330 °C/s is also investigated. Past HEL CFRP studies reported sample burn-through rates of 25 s/mm thickness in air at 500 W/cm² decreasing to 12 s/mm at 1500 W/cm² [36]. This study provides detailed characterization of CFRP thermal response to laser heating.

Experimental

CFRP testing panels from Protech Composites of 10.38 x 10.38 cm² and thicknesses of 1.7, 2.4, 3.1 mm were irradiated by a 2-kW cw IPG Photonics ytterbium doped fiber laser at 1.07 μm, as shown in Fig. 2. Panels were manufactured by layering multiple plies of 6K (6000 filaments per tow) 2x2 twill weave carbon fiber fabric in a mold and injecting epoxy resin under vacuum. The samples contain 4, 6, or 8 plies, in order of increasing thickness. The epoxy used was a Bisphenol A based epoxy resin blend. The hardener is unknown, cited as proprietary by the manufacturer.

The panels of 3.1-mm thickness were irradiated at 5, 10, 36, and 64 W/cm², with the 1.7-and 2.4-mm panels irradiated at 10 and 36 W/cm². The laser spot diameter was 6 cm (1/e²) for all but the 64 W/cm² shot (2.3 cm diameter). A beam splitter was used to illuminate a stationary scatter plate and the spatial and temporal laser beam variation was recorded by a calibrated near infrared (NIR) camera. Irradiance reached peak levels in approximately 0.5 s and irradiance σ per pixel varied from ±0.4-1.7 percent, peaking near laser hot spots. Spot size was stable and measured at 1/e² of peak value. Reported irradiance values are the average irradiance within 0.5 cm of laser center. Tests were run

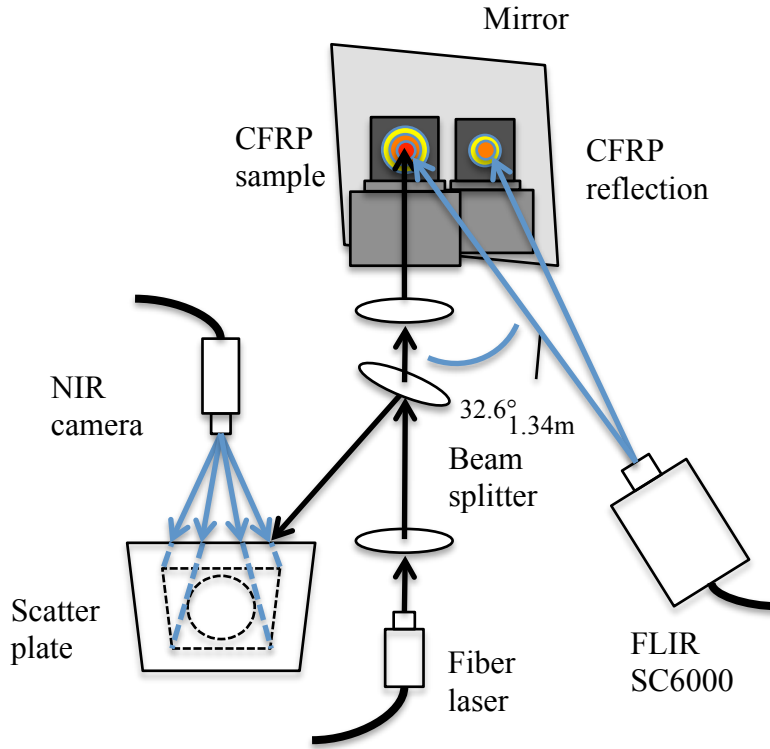


Fig. 2. Experimental Schematic

for two minutes or until surface ignition occurred. Surface cool-down after laser off was also recorded for > 60 s. Tests were set up on an open optical table with ceiling mounted ventilation hood (upward flow speed approximately 0.2 m/s). Experiments were recorded with a 30-Hz visible witness camera.

Thermal imagery was recorded using a FLIR SC6000 MWIR camera. The SC6000 has a 640 x 512 element InSb detector array but was windowed to 160 x 128 pixels to increase the frame rate. The camera was operated with a band pass filter from 3.8-4.0 μm and a neutral density filter of O.D. 1.0. A silvered mirror was placed behind the sample and angled to allow the SC6000 to view both the front and backside of the panel side-by-side in the same frame. The test panels were imaged at an angle of 32.6° off normal, in the same horizontal plane. Spatial resolution per FLIR pixel was 1.49mm

x 1.22 mm for the front and 1.61 x 1.48 mm for the back when accounting for off-axis viewing and reflection.

The mid-infrared imagery was corrected for detector non-uniformity, non-linearity, bad pixels and detector response on a pixel-by-pixel basis using a (Electro-Optical Industries CES600-06) wide area blackbody at $T = 50\text{--}600\text{ }^{\circ}\text{C}$. Images were collected sequentially at four integration times (0.1, 0.3, 2, and 4 ms for laser irradiance of 10 W/cm^2) at frame rates of 120-240 frames per second (30-60 fps per integration time). The multiple integration times extended the dynamic range to 300 – 2500 K.

The spectral emissivity of undamaged and damaged CFRP samples was observed from 2-25 μm with an SOC-100 HDR (Hemispherical Directional Reflectometer) manufactured by Surface Optics Corp. The SOC-100 uses a blackbody source at one focus of a hemi-ellipsoidal mirror to illuminate a sample at the other focus from every angle. The reflectance is sampled at a particular angle and sent to a Nicolet FTIR and along with measurements of a reference sample used to produce the hemispherical directional reflectivity (HDR). The HDR is converted to spectral emissivity (DSE) through the use of Kirchoff's law and conservation of energy. A heated sample stage allowed temperature dependence to be investigated up to $500\text{ }^{\circ}\text{C}$ [62]. Absorptivities of undamaged material, charred material, and bare fibers at $1.07\text{ }\mu\text{m}$ were also measured using a Cary 5000 UV-Vis-NIR spectrophotometer.

Results and discussion

Sample response to laser radiation.

A sequence of visible images during laser irradiation of a 3.1-mm panel at 35.7 W/cm² is shown in Fig. 3. Decomposition produced billowing clouds of volatile products and soot beginning at surface temperature of approximately 430 °C and continued from the panel as a whole until ignition or the end of the two-minute test. Ignition produced a large initial fireball before settling to a front surface flame corresponding to areas of removed resin. The test was terminated shortly after ignition and the laser spot cooled rapidly after laser off but the flame did not immediately extinguish, slowly diminishing as thermal volatile production decreased. Once ignited, the surface flame extended well beyond the top edge of the panel. At 35.7 W/cm² and 6-cm spot size, there were enough volatiles being produced on the backside of the panel to be ignited by the front side flames at surface temperatures well below those necessary for initial front side ignition (approximately 600 °C less). The resulting CFRP panel had a concentric-ring appearance. Working outward, laser center was reduced to bare carbon fiber with no apparent fiber damage, next to a ring of porous char, then a ring of discolored resin and finally undamaged resin. The radius of visible change ranged from approximately 2-3.5 cm for 5-35.7 W/cm² using the 3 cm laser beam radius. Given enough laser power and time, similar trends were observed on the panel backsides as well. The top panel edges suffered additional degradation from burning volatiles. Some panels also exhibited a ring of black tar-like deposits outside the laser spot from condensing volatiles.

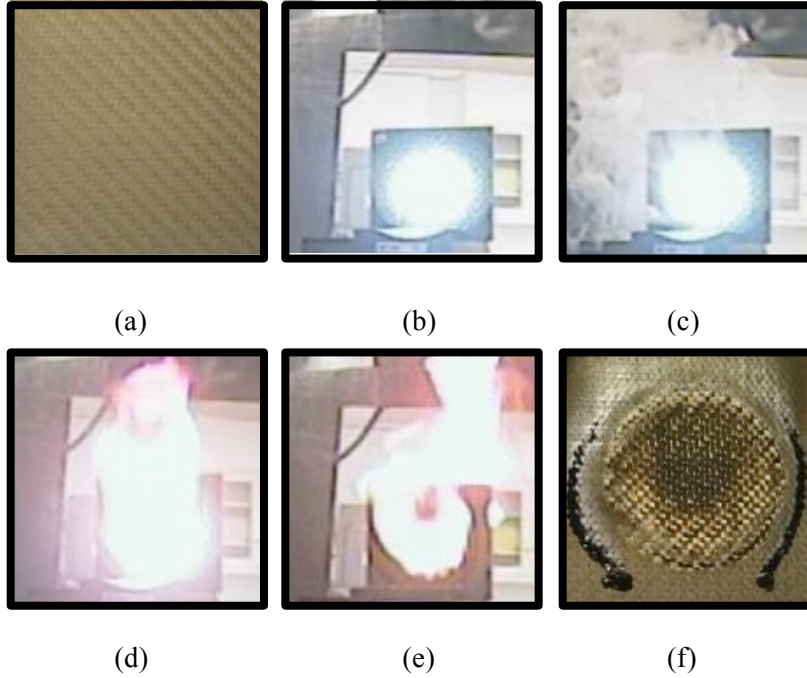


Fig. 3. Visible images of 3.1 mm panel, 35.7 W/cm^2 : (a) undamaged CFRP panel, (b) laser spot (1 sec), (c) smoky decomposition plume (5 sec), (d) surface flame (45 sec), (e) flame after laser-off (58 sec), and (f) final damaged panel. Panel dimensions are $10.2 \times 10.2 \text{ cm}$.

Mass loss increased with total incident laser energy with an increased rate of mass removal both for cases that achieved ignition and smaller laser spot size (Fig. 4). No significant mass loss is observed for total incident energies $E < 7.7$ and 5.2 kJ for non-ignition and ignition cases, respectively, at 6-cm laser spot diameter (average fluences of 290 and 195 J/cm^2). When the laser spot diameter is reduced to 2.3 cm, no mass loss is observed for $E < 2.8 \text{ kJ}$ (average fluence of 663 J/cm^2). The mass loss above this threshold increases approximately linearly with incident energy at rates of 109, 158, and 224 mg/kJ for non-ignition (6 cm) and ignition at 6-cm and 2.3-cm spot sizes, respectively (and with fluence at rates of 2880, 4180, and $950 \text{ mg/(J/cm}^2)$). The appearance of combustion flames increases the mass loss rate by 45 %.

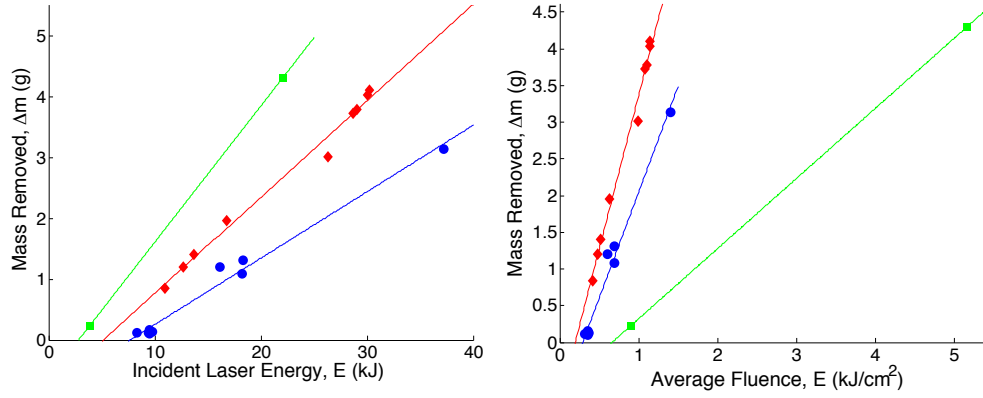


Fig. 4. Sample Mass Loss under (♦) ignition and (•) non-ignition conditions at 6 cm spot size and ignition at 2.3 cm spot (■).

Thermal imagery.

Laser irradiance and surface temperature profiles for a 3.1 mm CFRP sample are provided in Fig. 5. The laser spot at 9.9 W as imaged at the scatter plate is non-Gaussian with two major hot spots near beam center. In Fig. 5 (d), the corresponding calibrated temperature map is shown. A slight camera misalignment produced an internal reflection of approximately 1% that displaces laser center 34 mm to the right and 22 mm upward (temperatures from this region are not used). After 30 s of irradiation at 9.9 W/cm², the peak temperature is 634 °C and the edges of the sample are near 100 °C. The surface temperature distribution is generally radially symmetric and mirrors the laser input with broadening due to thermal diffusion. The impact of convection on relative temperatures above and below the laser spot is minimal.

The calibration and merging of multiple integration times is illustrated in Fig. 5(b) and (c). The 14-bit camera saturates at 16,384 counts, and saturation is realized at $r < 2$ cm for the 4-ms integration time. For the 0.1- and 0.3-ms integration times, the entire

image is unsaturated. After correcting the image for nonlinear response, the background (dark) signal is about 2200 counts. The detector noise, defined as the 1σ variance, is 67 counts for a signal of 3184 counts. Each of the four integration times was processed separately to yield temperature and then merged into a single surface temperature map. In Fig. 5(c), the vertical temperature profile along the laser centerline is shown assuming sample emissivity $\epsilon=1$ for each of the integration times. In regions of overlap, multiple temperature readings were averaged to yield a single temperature at each pixel. The average difference between temperatures produced from multiple integration times was generally small and ranged from 2-3 K (noise floor) up to 11-12 K. For cases where the difference is greater, discontinuities may be visible in the temperature history of a given sample location, indicating when integration time switchover occurred.

Surface emissivity and absorptivity.

Transmission of the surface epoxy at both 1.07 and 3.9 μm is greater than 90% [15]. However, once the epoxy begins to char the absorption at both wavelengths increases rapidly. The absorption depth of a carbon fiber is much less than the fiber diameter [59]. Thus, the primary absorbers in a CFRP are the first few surface fibers of the surface ply and initial surface temperature measurements are of these surface fibers. As the epoxy begins to char, the charred material begins to contribute to the surface emission.

The accuracy of the surface temperature is primarily dependent on surface emissivity at the 3.9- μm wavelength of the thermal camera. The emissivity of the CFRP samples was studied using the SOC-100 reflectometer. The temperature dependence of the

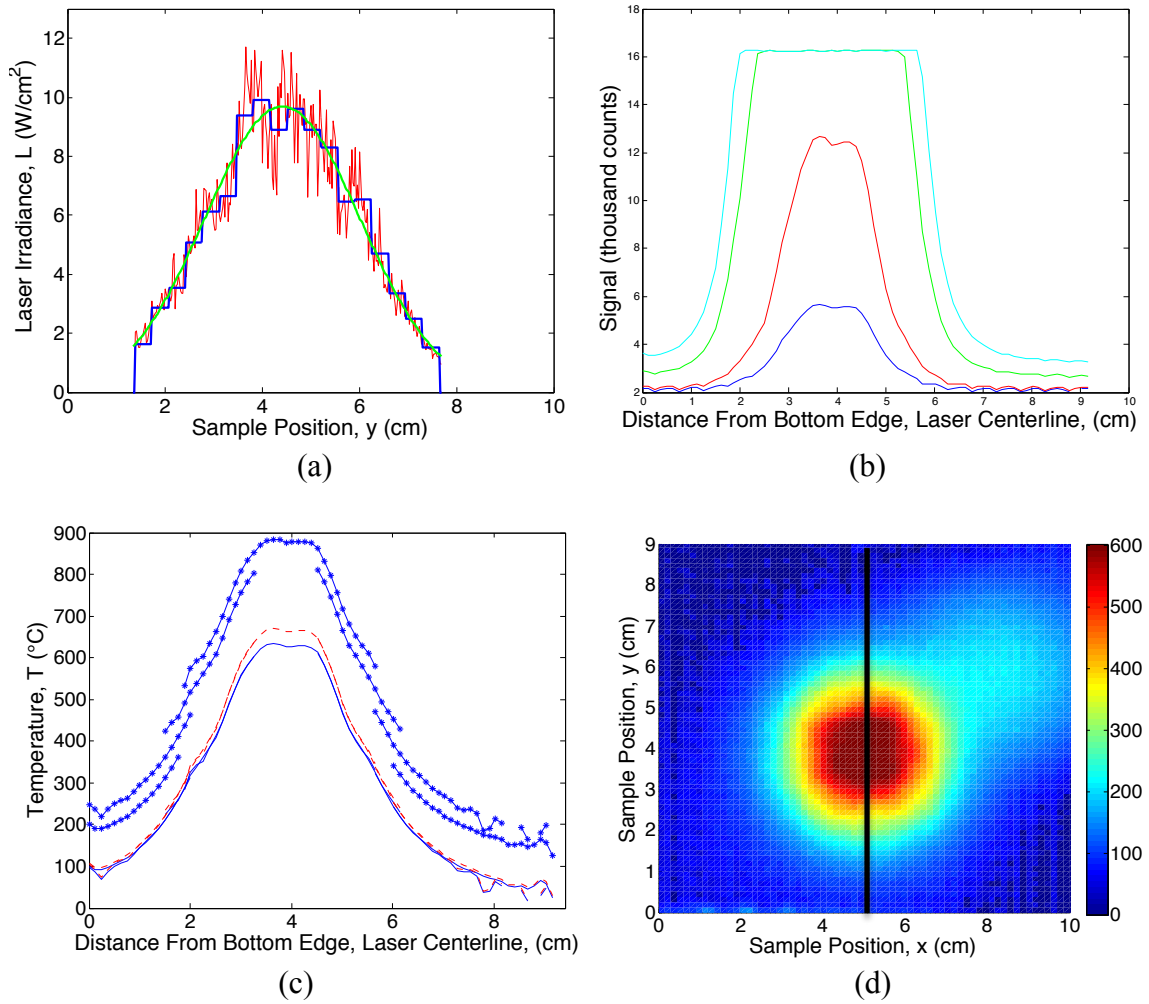


Fig. 5. (a) Temporally averaged laser center irradiance profile in vertical direction at $9.9 \text{ W}/\text{cm}^2$ spatially averaged irradiance at measured and modeled spatial resolution, (b) uncalibrated FLIR signal at 4 integration times (0.1, 0.3, 2, and 4 ms) for a vertical slice through laser center at $9.9 \text{ W}/\text{cm}^2$ and 30 s, (c) signal from part (b) calibrated for absolute temperature at: $\epsilon = 1$ (solid line) with offsets to illustrate overlap from different integration times (dotted lines) and $\epsilon = 0.85$ (dashed line) with all integration times overlaid, and (d) final FLIR front surface temperature map ($^{\circ}\text{C}$) showing vertical temperature slice used for parts (a-c).

emissivity for undamaged and damaged samples is provided in Fig. 6. The emissivity of the undamaged CFRP samples is high and largely independent of wavelength, and graybody approximation would be appropriate. However, as the surface evolves due to

laser irradiation, the emissivity declines and exhibits stronger wavelength dependence. The decrease in emissivity with wavelength is consistent with the general trend often observed for carbon-based materials [65–67]. As shown in Fig. 6(b), the emissivity is constant over the 3.8–4.0 μm bandwidth of the MWIR camera, allowing a constant ϵ value to be used across the bandwidth. The temperature dependence of the observed emissivity at 3.9 μm is illustrated in Fig. 6(c). The undamaged CFRP samples were measured from room temperature up to a maximum of 125 °C to avoid decomposing the resin and contaminating the mirror of the SOC-100. Over this range, the emissivity of undamaged CFRP shows little temperature dependence. Contamination from outgassing volatiles also precluded high temperature measurement of partially decomposed CFRP resin. However, the emissivity of both surface (sooty, used as pseudo-char) and interior (bare) fibers from fully decomposed CFRP were measured up to 500 °C. A larger decrease in emissivity occurs during phase changes, with smaller reductions within a given phase. The narrow bandwidth of the thermal camera used here only requires knowledge of the emissivity at 3.9 μm and is not sensitive to varying wavelength dependence, but also prevents the simultaneous determination of temperature and emissivity from the thermal imagery. Multi-wavelength or hyper-spectral imaging instruments could potentially determine both parameters but would require knowledge of the shape of the emissivity curve as a function of wavelength.

Fig. 6(d) illustrates the sensitivity of temperature determination to emissivity at 3.9 μm . For this example, ϵ is 0.75 and varies as much as ± 0.1 . This error in ϵ produces measured temperatures ranging from 1275–1500 °C for true temperatures of 1400 °C.

As temperatures increase and ϵ decreases, the same absolute error in ϵ produce greater systematic error in measured temperature. The statistical error is defined by detector noise and is much lower, typically 2-3 °C.

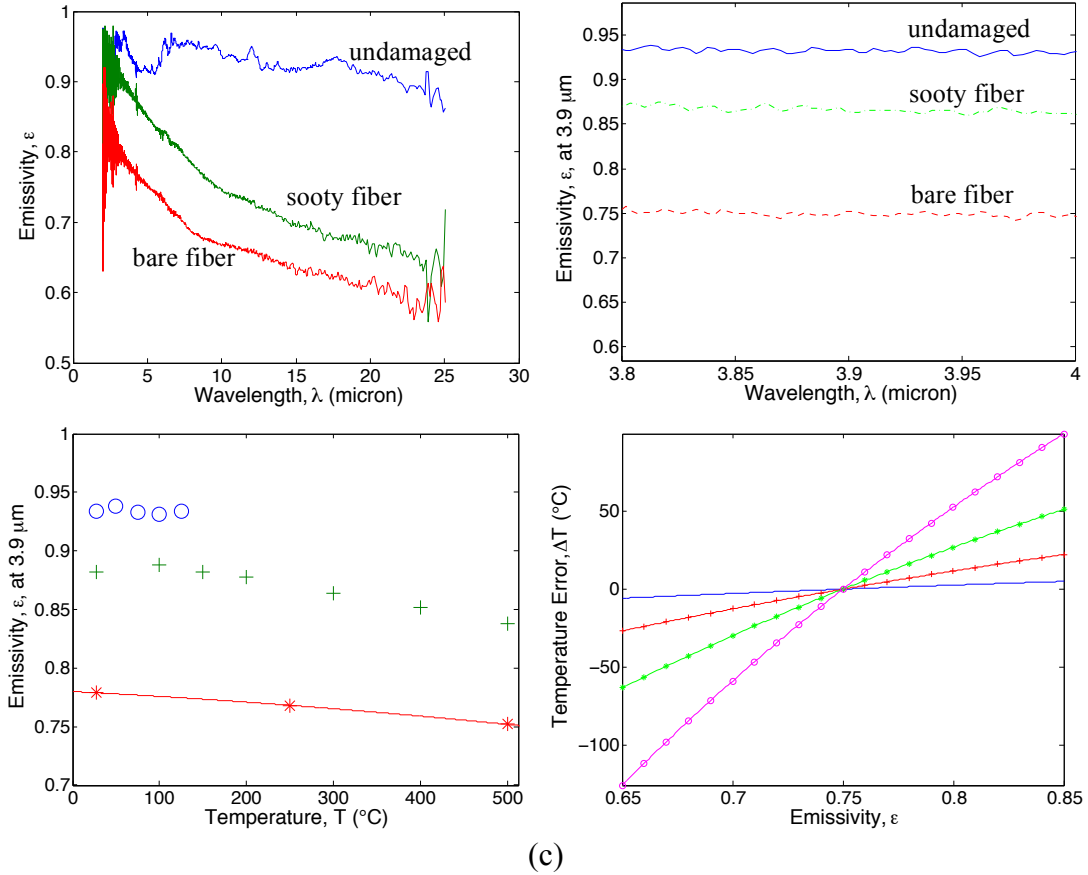


Fig. 6. Emissivity (a) decreases with wavelength and as decomposition progresses from [—] virgin resin to [—] char to [—] bare fiber, (b) emissivity is constant over the bandwidth of the MWIR camera, (c) emissivity at 3.9 μm decreases slowly as temperature increases and (d) temperature error due to incorrect emissivity (true $\epsilon = 0.75$) at 3.9 μm at [—] 100 °C, [+] 500 °C, [*] 900 °C, and [o] 1400 °C.

The emissivity data was combined to yield a single temperature-dependent emissivity curve at 3.9 μm , taking into account CFRP phase transitions at characteristic temperatures and distinct transition points in this testing. For all temperatures below 300 °C, I choose $\epsilon = 0.93$, reflective of undamaged CFRP. From 300-400 °C, emissivity

decreases from $\varepsilon = 0.93$ to 0.86 linearly with temperature to simulate decreasing emissivity as the resin decomposes. From 400-500 °C, emissivity is held constant at 0.86 but decreases further to 0.77 from 500-600 °C as the char is oxidized to leave bare carbon fiber. From 600 °C onward emissivity decreases linearly with temperature, $\varepsilon = 0.792 - 0.06 (T/1000 \text{ K})$, as summarized in Table 3.

As shown in Fig. 7, the measured room temperature absorptivity (α) of undamaged CFRP at 1.07 μm was equal to the emissivity at 3.9 μm , as expected from the relatively flat ε curve in Fig. 6(a). The absorptivity of dehydrated resin was assumed to

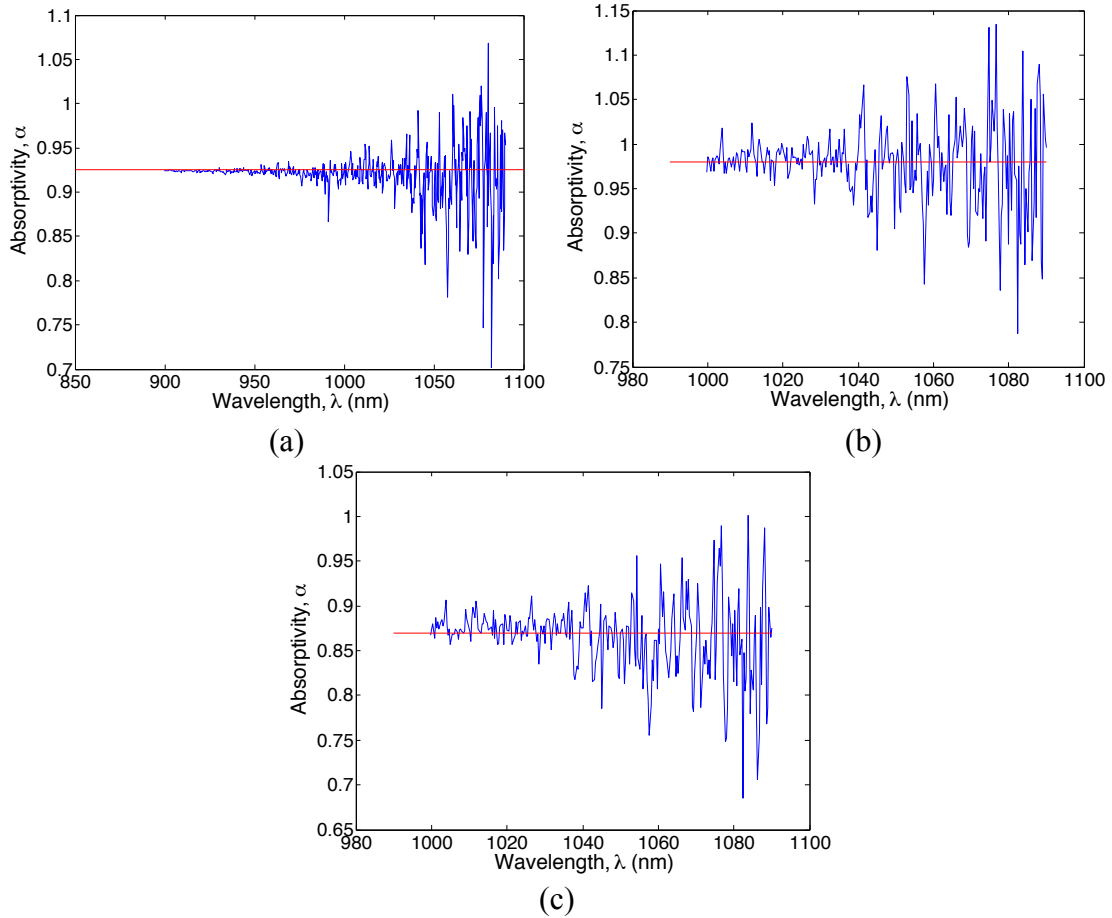


Fig. 7. Measured absorptivity of (a) undamaged CFRP (b) charred CFRP and (c) bare fiber at 1.07 μm and surrounding wavelengths.

be 0.93 as well. Surface charring produced an absorptivity increase, to 0.98, and a bare fiber room temperature $\alpha = 0.86$. These absorptivities are in general agreement with other measurements and simulations [61, 68] and assumed to be temperature independent for resin, dehydrated resin, and char. In the case of bare fiber, it was assumed that the rate of decrease of absorptivity with increasing temperature was the same as that observed for emissivity decrease at $3.9 \mu\text{m}$.

Evolving surface temperatures.

Fig. 8 compares the evolution of the front and backside temperatures at laser center for several laser irradiances. Higher irradiance produced higher steady-state surface temperatures ($>1300^\circ\text{C}$), higher initial heating rates ($\geq 330^\circ\text{C/s}$), and higher final backside temperatures ($> 450^\circ\text{C}$). The onset of ignition occurred at $T = 1100 - 1250^\circ\text{C}$, which is generally achieved under these buoyant conditions for irradiances exceeding 20 W/cm^2 . Ignition was observed on the front side only, except in cases of piloted backside ignition from front surface flames.

At lower irradiance, distinct changes in material properties were visible. At 5 W/cm^2 , several regions are observed: (1) initial heating of undamaged material (0-26 s $27-260^\circ\text{C}$), (2) start of decomposition with increased heating rate (26-32 s, $260-400^\circ\text{C}$), (3) peak decomposition with momentary cooling (32-41 s, $400-430^\circ\text{C}$) and (4) gradual heating for remainder of test (41-120 sec, $400-550^\circ\text{C}$). At 9.9 W/cm^2 , a similar behavior was exhibited, only at a faster rate and a higher steady-state temperature, $T = 780^\circ\text{C}$, was reached. At 35.7 W/cm^2 , surface decomposition occurs rapidly and the surface reaches a momentary steady state condition at 10 s and $T = 1020^\circ\text{C}$ before

resuming heating. Ignition occurs at 44 s and $T = 1203\text{ }^{\circ}\text{C}$. Finally, At 63.7 W/cm^2 , heating is very rapid, combustion occurs after 3.7 seconds and reaches a temperature of $T > 1400\text{ }^{\circ}\text{C}$. Rapid cool down is observed for all samples with the front side cooling more rapidly than the backside of the panel, leading to a crossover point with a temperature differential that increases with irradiance. Backside temperatures show a steep initial increase but level off around $175\text{ }^{\circ}\text{C}$ momentarily for all irradiance levels. However, increasing irradiance shortens this interval, followed by heating to higher temperatures. Fig. 9 compares the temperature profiles for decreasing sample thicknesses at a constant 9.9 W/cm^2 irradiance. As sample thickness decreases, front side steady state temperatures increase modestly. Backside temperatures show a similar progression, reaching an irradiance-dependent steady state temperature more quickly as irradiance is increased. Thinner samples display little temperature gradient during sample cool-down. Radial temperature distribution at 60 and 120 s are shown in Fig. 9 for 5 and 9.9 W/cm^2 . Temperature profiles through laser center at several temperatures are shown later in conjunction with model results.

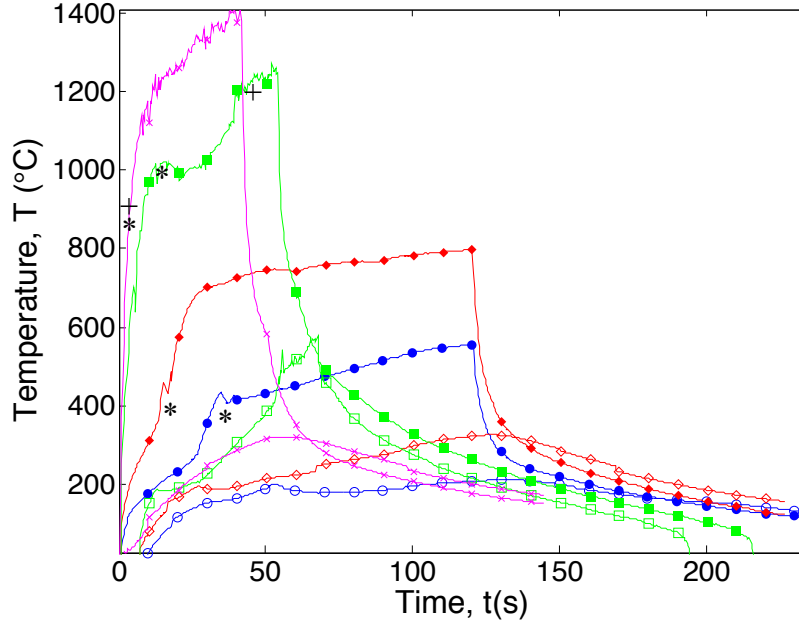


Fig. 8. (filled symbols) front and (open symbols) backside temperatures for a 3.1 mm thick panel at (\bullet) 5 W/cm², (\blacklozenge) 9.8 W/cm², (\blacksquare) 35.7 W/cm², and ($*$) 63.7 W/cm². Markers are included at point of maximum decomposition ($*$) and ignition ($+$).

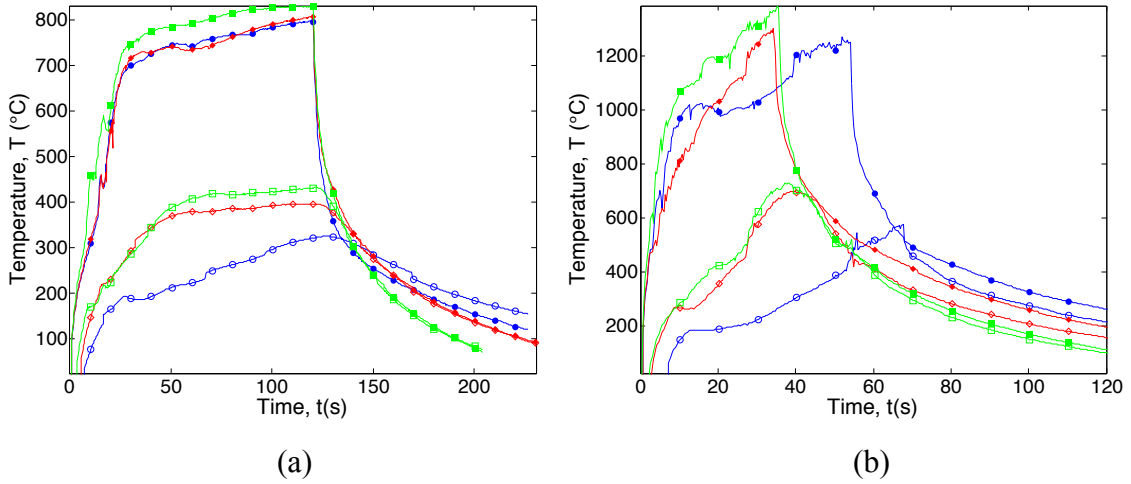


Fig. 9. Evolving temperatures at laser center for (a) 9.9 W/cm² and (b) 35.6 W/cm². Comparisons are made between (filled symbols) front surface and (open symbols) back surface laser center temperatures for sample thicknesses of (\bullet) 3.2 mm (\blacklozenge) 2.4 mm, and (\blacksquare) 1.7 mm.

Thermal model.

A 3D thermal model (coded in MATLAB®) was used to interpret the laser-CFRP interaction and resulting heating and decomposition [66, 67]. I used a 3D explicit finite difference model based on Fourier's heat diffusion equation and appropriate reaction source/sink terms:

$$\rho C_p \frac{\partial T}{\partial t} = k_x \frac{\partial^2 T}{\partial x^2} + k_y \frac{\partial^2 T}{\partial y^2} + k_z \frac{\partial^2 T}{\partial z^2} + \frac{Q_{rxn}}{V} \frac{dm_{rxn}}{dt} + \frac{dm_{flow} C_{p_{gas}} \partial T}{V} \quad (5)$$

with Neumann boundary conditions for laser absorption, surface emission, and convection:

$$k \frac{\partial T}{\partial x,y,z} = -h(T - T_{\infty}) - \varepsilon \sigma (T^4 - T_{\infty}^4) + \alpha L \quad (6)$$

where ρ , C_p , k , ε , α , and T are the composite density, specific heat, thermal conductivity, emissivity, absorption, and temperature of each element and h , σ , and T_{∞} are the convection coefficient, Stefan-Boltzmann constant and ambient temperature.

Conductivity (k) for CFRPs is anisotropic, with a much higher conductivity along the fiber direction. The 2x2 twill fiber weave of these samples provide equal conductivity in the plane perpendicular to the incoming laser (x and y directions). The conductivity in the thickness (k_z) direction, parallel to the incoming laser, is much less due to the much lower conductivity of the resin matrix. This anisotropy is reflected by different values for k_x , k_y , and k_z in Eq. (5).

The Stefan-Boltzmann law, modified by the same temperature and phase-dependent surface emissivity curve used to determine the surface temperatures, is used to model radiation losses. The integrated spectral emissivity, as shown in Fig. 6(a), could be used instead, but this approximation simplifies the model and introduces < 5% error in

radiated power at these temperatures. The affect of varied emissivity on radiated power in CFRP simulations is shown in Fig. 46 in Appendix A. Convection loss is approximated using calculated surface temperatures, ambient room temperature and a convective heat transfer coefficient calculated from natural convection from a vertical plate with average surface temperatures ($h_{\text{conv}} = 1.5 \times 10^{-4} \text{ W/cm}^2 \text{ K}$) [67].

The model mesh was 30 x 30 uniform elements in the plain perpendicular to the incoming laser, with an element for each carbon fiber ply in the parallel direction (8, 6, and 4 elements for 3.2, 2.4, and 1.7-mm thick samples, respectively). Computational stability was maintained by continually updating the time step according to the Courant-Friedrichs-Levy (CFL) condition [68]:

$$dt \leq \frac{\rho C_p \Delta}{2k_{\text{max}}} \quad \Delta = \frac{dx^2 dy^2 dz^2}{dx^2 dy^2 + dy^2 dz^2 + dx^2 dz^2} \quad (7)$$

as material properties changed with decomposition. Time steps generally ranged from 50-150 ms.

Changing material properties are assumed first to be a function of evolving CFRP decomposition phase, in proportion to the relative amounts of each decomposition phase (virgin resin, dehydrated resin, char, and bare fiber) present in each cell. The fibers were assumed to be inert at these temperatures and exposure times. Temperature dependencies derived from outside sources were used when available. Most notably the heat capacity, $C_p(T)$ and thickness conductivity, k_z , of the virgin CFRP material were measured by Kalogiannakis et al. using a modulated-temperature differential scanning calorimetric technique [69]. They provide three linear equations for both properties that describe $C_p(T)$ from -30 to 165 °C and $k(T)$ from -50 to 125 °C.

$$C_p(T): T < 77.7 \text{ }^{\circ}\text{C} \quad 3.692\text{E-}03 * T(^{\circ}\text{C}) + 8.043\text{E-}01 \quad (8)$$

$$77.7 \text{ }^{\circ}\text{C} < T < 100.5 \quad 9.761\text{E-}03 * T(^{\circ}\text{C}) + 3.567\text{E-}01 \quad (9)$$

$$100.5 \text{ }^{\circ}\text{C} < T \quad 1.858\text{E-}03 * T(^{\circ}\text{C}) + 1.172 \quad (10)$$

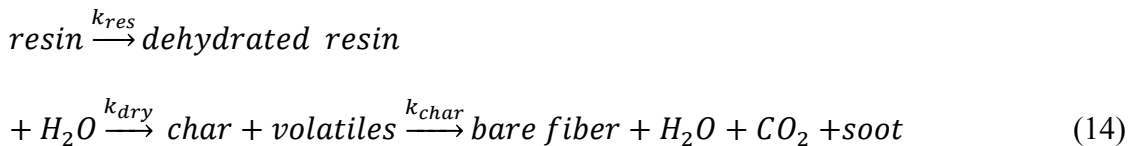
$$k(T): T < 73 \text{ }^{\circ}\text{C} \quad 7.57\text{E-}04 * T(^{\circ}\text{C}) + 5.6835\text{E-}01 \quad (11)$$

$$73 \text{ }^{\circ}\text{C} < T < 99 \text{ }^{\circ}\text{C} \quad -2.69\text{E-}03 * T(^{\circ}\text{C}) + 8.291\text{E-}01 \quad (12)$$

$$99 \text{ }^{\circ}\text{C} < T \quad 1.23\text{E-}03 * T(^{\circ}\text{C}) + 4.402\text{E-}01 \quad (13)$$

A different region (before, during, and after glass transition) is described for each property. I use the after-glass-transition equation to extrapolate values for temperatures beyond those reported, until the resin begins to decompose. Heat capacity and thermal conductivity values for decomposition phases were estimated from comparison of my experimental temperatures and model results. Resin, char, and fiber densities were derived from literature [38] and supplier values and were used with measured sample densities to estimate sample fiber fraction. Phase emissivities were measured as previously described.

Epoxy decomposition progresses sequentially from cured resin (res) to dehydrated resin (dry) to char with full char oxidation to leave bare carbon fiber [29–31, 69, 70]:



Resin decomposition kinetics were assumed to be first-order Arrhenius reactions:

$$\frac{dm_{res}}{dt} = -A_{res}m_{res}e^{-E_{res}/RT} \quad (15)$$

$$\frac{dm_{dry}}{dt} = r_{dry}A_{res}m_{res}e^{-E_{res}/RT} - A_{dry}m_{dry}e^{-E_{dry}/RT} \quad (16)$$

$$\frac{dm_{char}}{dt} = r_{char}A_{dry}m_{dry}e^{-E_{dry}/RT} - A_{char}m_{char}e^{-E_{char}/RT} \quad (17)$$

where A_{res} , A_{dry} , A_{char} , E_{res} , E_{dry} , and E_{char} are the Arrhenius pre-exponential factors and activation energies for epoxy resin, dehydrated resin, and char decomposition. Branching ratios, r_{dry} and r_{char} , are used to account for associated mass loss due to dehydrated water and volatile products produced during decomposition. Fibers were assumed to be inert at these relatively low-temperature, short-term exposures, having a sublimation temperature well above validate or improve accuracy of the value 3000 °C [72]. Energy produced or consumed by the dehydration and char-forming decomposition reactions:

$$q_{rxn} = Q_{rxn} \frac{dm_{rxn}}{dt} \quad (18)$$

was assumed to be proportional to mass loss [38]. This simplified approach is in line with prior kinetic studies [29, 30] and mass loss modeling [30] of epoxy decomposition. Comparisons are made to previous modeling efforts in Table 4 with the following differences: (1) single step decomposition [36, 37] is compared to dehydrated resin decomposing to char, (2) different rates used for dehydrated resin decomposition and char production in lieu of a branching fraction, [30] (3) different kinetics for different phases of the same reaction, [37] and (4) higher order mechanisms [37]. New kinetic parameter estimates are derived in this work from fitting the thermal model simulation to measured temperatures from the mid-IR imagery, as discussed below.

The heat capacity of the departing decomposition products produce a cooling effect as well. Mass loss due to dehydration, decomposition and char oxidation occurs throughout the material and products are heated as they exit. Taking a back-to-front approach, it is assumed that each model element must heat up the mass produced in it and all previous elements (in a given time step) over the temperature difference between the previous and current element. In this model, it is assumed that all mass loss has a constant heat capacity and that all mass exits through the front (laser incident) face. The value heat capacity of departing gas ($C_{p_{\text{gas}}}$) is assumed to be similar to literature values [37] and is listed in Table 3.

The incident laser intensity distribution was measured throughout each experiment, combined into an average irradiance map and used directly as an input into the thermal model. The scatter plate image resolution was reduced to match the front surface model mesh (shown in Fig. 5(a)) and assumed to be absorbed by the first few layers of individual carbon fibers of the topmost ply throughout the experiment in accordance with high fiber absorption and scattering models [59]. Surface absorptivities at $1.07\text{ }\mu\text{m}$ of undamaged material, char, and bare fiber were measured with a spectrophotometer at room temperature as previously described. For the purposes of this work, it was assumed that the absorptivity of the bare carbon fibers began at the room temperature value measured with a spectrophotometer and decreased at the same rate as the fiber emissivity with increasing temperature (equation in Table 3).

The measured room temperature absorptivities at $1.07\text{ }\mu\text{m}$ into the surface layer seem adequate for lower irradiance tests. However, as irradiance increases, large amounts of volatiles and soot are produced at the surface, absorbing and scattering the

incoming beam to an unknown extent. This effect is estimated by modifying the absorptivity by an additional constant (α_c). At 35 and 64 W/cm², values for this constant of approximately 0.7 and 0.55, respectively, produce observed laser-center heating rates.

Fig. 10 and 11 show comparisons between predicted and observed temperatures at laser center throughout the whole experiment. Fig. 10 also shows radial profile comparisons through laser center at 30, 60, and 120 seconds.

Initial heating until the start of decomposition (approximately 150 °C) is described well by conduction using the temperature dependent conductivity and heat capacity measured by Kalogiannakis et al [69]. The conversion from virgin resin to dehydrated resin is accompanied by a significant reduction in thickness conductivity, leading to an increased surface heating rate (best illustrated by 5 W/cm² case in Fig. 8). This brings about the primary decomposition step in which many of the bonds in the resin chemical structure are broken, producing volatile products and char. Both the dehydration and decomposition reactions are endothermic [10] and play a primary role (in addition to reduced thickness conductivity) in reducing the backside temperature increase. Further energy loss is provided by heat capacity of the departing volatiles. Together this produces a large temperature gradient between the front and back surfaces and provides a heat sink that provides a momentary backside cooling effect. Modeling CFRP without the endothermic reaction enthalpies or volatile heat capacity increases the final backside temps by 100 and 90 °C at 5-and 10-W/cm² laser powers, respectively. Once decomposition has completed, char remains and begins to oxidize, which slowly

increases surface temperatures further due to reduced material density and thickness conductivity resulting from material swelling and enlarging of voids within the material. Initial cooling after the laser is turned off is rapid and dominated by radiation losses.

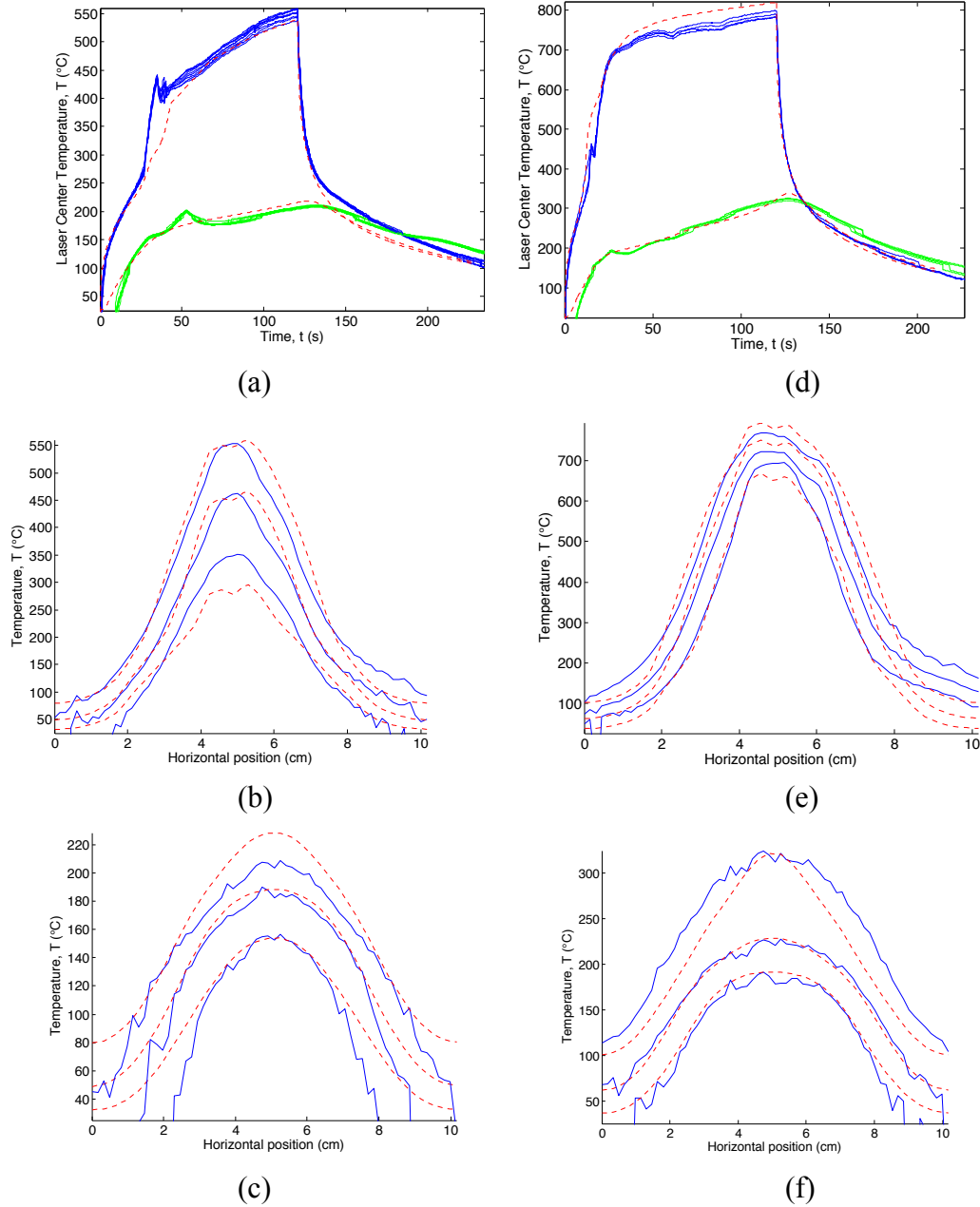


Fig. 10. Front (—), backside (—), and modeled (---) laser center temperatures of 3.2 mm thick panels at (a-c) 5 W/cm² and (d-f) 10 W/cm². Radial temperature profile comparisons are shown at 30, 60, and 120 seconds (increasing throughout).

Later stages are driven by the distribution of conductivities remaining from the laser-induced material changes.

The rate of volatile production increases with irradiance. Under buoyant conditions, ignition occurs at measured surface temperatures of 1103 ± 73 °C for all irradiances studied here. Volatile production is heaviest at laser center as surface temperatures pass through 375-425 °C (marked by * in Fig. 8). The size of the surface plume decreases as surface resin at laser center is exhausted. Resin at the edge of the laser spot decomposes more slowly as heat is conducted radially outward. In tests where ignition is delayed, these volatiles condense at the edges of the laser spot into a black, sticky tar-like deposit. This volatile cloud appears to produce thermal emission that is not captured in this model.

The thermal model thus described was used to infer the type and degree of material property changes necessary to produce the observed temperatures. Only one set of thermal properties and kinetic parameters (Tables 1 and 2) describe the behavior of CFRP under all irradiance levels studied here.

Prior TGA studies [27] conducted at lower heating rates (0.2-3.3 °C /s) indicated that decomposition kinetics varied with heating rates. Heating rates leading to decomposition varied widely (12-330 °C/s) over the irradiance levels studied here, but did not require different kinetic rates to model. It appears that the mechanism responsible for the heating rate dependence saturated somewhere between the lower rates studied previously and the very high rates of the present study.

The agreement between the model and data is better for lower irradiance tests where decomposition stages are delayed, allowing more to be inferred from the data.

This model does not include gas phase combustion effects, which decreases the agreement in higher irradiance tests.

A notable discrepancy occurs in Fig. 10 during peak surface decomposition (especially at 5 W/cm²), which is modeled as an endothermic process and cools the sample. However, observed temperatures spike during peak decomposition. This may be due to thermal emission from the smoky plume. Plume emissivity is estimated to be

Table 3. Thermal parameters derived in this work compared with prior studies.
^afiberglass/epoxy, ^b properties reported for isolated components, not resin phase and fiber in composite, ^ctemperature dependent [69], ^dphenol resin with glass filler (random orientation)

Parameter	[39] ^a	[38]	[37] ^d	This work
Resin density (g/cm ³)	-	0.9	-	1.1
Fiber density (g/cm ³)	-	1.76	-	1.76
Composite density (g/cm ³)	-	-	1.81	1.463
Fiber fraction (w/w)	0.5	-	.605	0.55
k _{xy} res (W/m K)	-	-	-	5
k _{xy} dry (W/m K)	-	-	-	5
k _{xy} char (W/m K)	-	-	-	3
k _{xy} fib (W/m K)	-	-	-	3
k _z res (W/m K)	0.162	0.246	0.81-0.91	0.59-0.47^c
k _z dry (W/m K)	-	-	-	0.2
k _z char (W/m K)	0.1	0.062	1.25-1.6	0.15
k _z fib (W/m K)	-	-	-	0.1
C _p res (J/kg K)	1540	2500 ^b	1100-1500	900-1470^c
C _p dry (J/kg K)	-	-	-	1330
C _p char (J/kg K)	1300	1589 ^b	1250-1600	1150
C _p fib (J/kg K)	-	794	-	794
h _{conv} (W/cm ² K)	-	-	-	1.5 x 10⁻⁴
ε _{res}	-	1	-	0.93
ε _{dry}	-	1	-	0.93
ε _{char}	-	1	-	0.86
ε _{fib}	-	1	-	0.792 – 0.06 (T/1000 K)
α _{res}	-	-	-	0.93
α _{dry}	-	-	-	0.93
α _{char}	-	-	-	0.98
α _{fib}	-	-	-	0.882 – 0.06 (T/1000 K)
C _{p,gas} (J/kg K)	-	0.72 x 10 ³	9.63 x 10 ³	2.0 x 10³
α _c	-	-	-	0.55-1

approximately 0.015-0.03 at 3.9 μm for 5 W/cm^2 during the period of maximum surface decomposition using data collected with an imaging Fourier Transform Spectrometer. Using modeled and measured temperatures at the peak of decomposition (30 seconds in Fig. 10(a) along with measured surface emissivity allows the estimation of the plume emissivity necessary to explain the observed effect. The necessary plume temperatures and emissivities range from $\epsilon = 0.055\text{-}0.1$ at 3.9 μm and $T_{\text{plume}} = 1080 - 1300\text{K}$.

Table 4. Kinetic parameters derived in this work compared with prior studies.

Parameter	[39]	[38]	[30]	[37]	This work
$A_{\text{res}} (\text{s}^{-1})$	-	-	3.6×10^8	-	1.8×10^8
$E_{\text{res}} (\text{kJ/mol})$	-	-	125	-	89
$A_{\text{dry}} (\text{s}^{-1})$	2.16×10^6	3.15×10^{11}	8.1×10^4	1.98×10^{-29} 8.16×10^{18}	9.7×10^9
r_{dry}	-	-	0.98	-	0.98
$E_{\text{dry}} (\text{kJ/mol})$	117	182	92	260	120
n_{dry}	-	1.344	-	17.33 6.3	-
$A_{\text{char}} (\text{s}^{-1})$	-	-	1.1×10^5	2.61×10^7	1.8×10^8
r_{char}	0.53	-	-	-	0.4
$E_{\text{char}} (\text{kJ/mol})$	-	-	120	354	150
n_{char}	-	-	-	0.53	
$Q_{\text{p res}} (\text{J/kg})$	-	-	-	-	-1.3×10^6
$Q_{\text{p dry}} (\text{J/kg})$	-0.198×10^6	-0.9×10^6	-	-0.234×10^6	-1.0×10^6
$Q_{\text{p char}} (\text{J/kg})$	-	-	-	-2.093×10^6	0

Another discrepancy exists in the backside temperatures of thinner samples at 9.9 W/cm^2 . The model predicts gradual backside heating as the decomposition reactions proceed, leading to steady state temperatures at full backside char. Decomposition is incomplete with the thickest sample and completed quickly in the thinnest one, with good prediction. For medium thickness, the model predicts intermediate behavior, but the data is more reflective of the thinner samples.

During the higher irradiance tests, temperatures rise through surface resin dehydration and decomposition very quickly and ignite when the surface temperature reaches approximately 1170 °C. Surface combustion is turbulent and contributes to the thermal emission and produces an apparent surface heating of an additional 100-200 °C. As before, backside temperatures reach a quasi-steady state during dehydration and decomposition reactions (with a duration proportional to sample thickness), increasing after the reaction completes. In Fig. 11(a)-(c), the laser spot size fills almost the entire

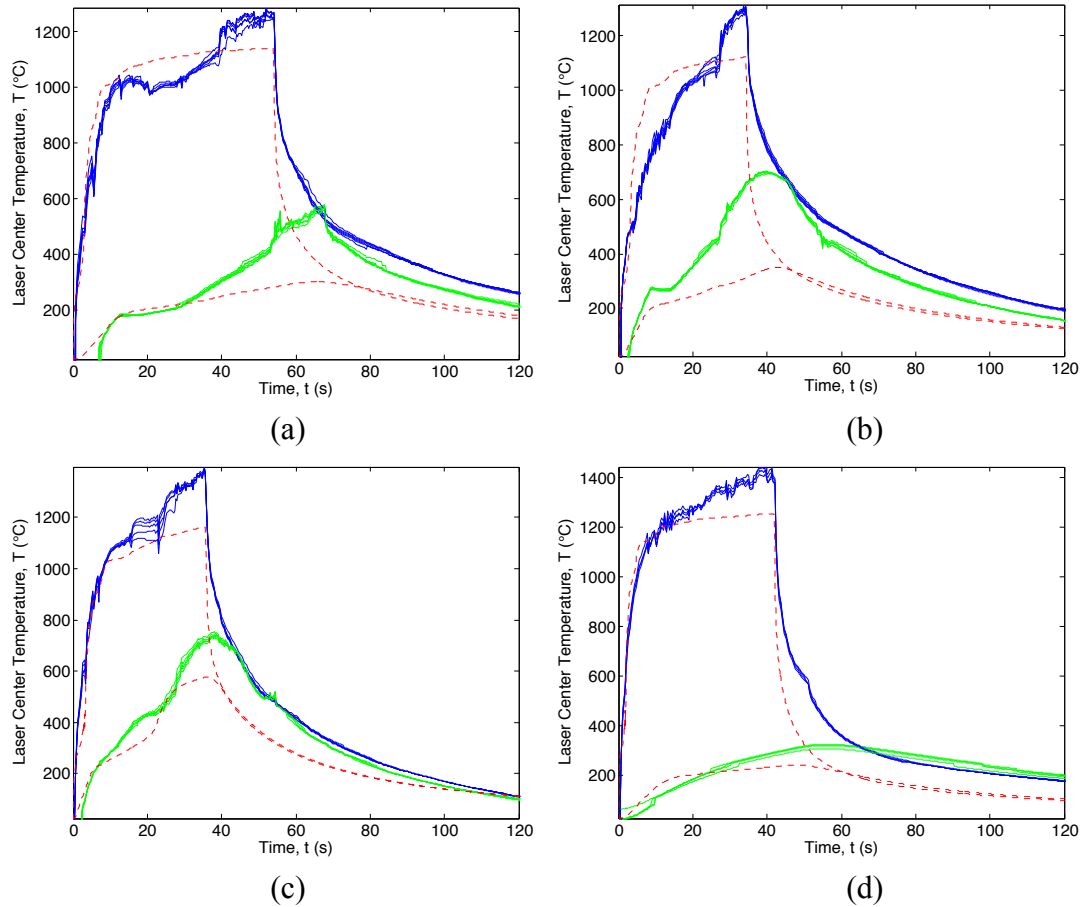


Fig. 11. Model fit (dashed) of front and back side temperatures at laser center. Multiple pixels near laser center are plotted for laser irradiances and sample thickness of: (a) 35.7 W/cm², 3.1 mm thick, (b) 35.7 W/cm², 2.4 mm thick, (c) 35.7 W/cm², 1.7 mm thick, (d) 63.7 W/cm², 3.1 mm thick.

test panel, allowing the front surface flames to extend beyond the sample and ignite backside volatiles well before self-ignition. This leads to a similar increase in backside surface temperatures. In the case of Fig. 11(d), the laser spot size is reduced (2.3 cm) and the irradiance is higher, preventing premature backside ignition and progressing rapidly through surface decomposition, decreasing thickness conductivity more rapidly. In all combustion cases, model temperatures during cool down are underestimated due to combustion being neglected in the heat transfer model.

Conclusions

Front and backside temperature maps at 30-60 Hz frame rates for the laser irradiation of CFRP at $1.07\text{ }\mu\text{m}$ at $5\text{-}64\text{ W/cm}^2$ are observed and modeled to estimate resin decomposition kinetic parameters, the enthalpies of decomposition, and the thermal properties of decomposition reaction stages at high heating rates.

The model is a three-dimensional explicit finite difference model based on Fourier's heat diffusion equation, Neumann boundary conditions for laser absorption, surface emission, and convection and internal loss terms for heat of decomposition and heat capacity of departing volatile products. Combining front and backside thermal imagery at high frame rates over a range of target thicknesses and laser powers, combined with supplementary measurements and literature values, constrains potential model parameters. Results are most sensitive to absorptivity, emissivity, heats of reactions, and conductivity of virgin resin, dehydrated resin, char, and bare carbon fiber as CFRP undergoes thermal decomposition. Knowing these parameters allows

complex phenomenology of laser-material interactions to be adequately modeled with reduced dimensionality, yielding rapid progress on characterizing laser lethality.

Decomposition kinetics do not appear to be heating rate dependent at the heating rates studied here. An increase in decomposition temperature is observed when transitioning from TGA heating rates (0.1-0.5 °C /s) to moderate heating rates (3-4 °C/s), but little additional increase appears to be produced by the very high rates (12-330 °C/s) studied here.

Resin matrix removal from CFRPs as a result of HEL heating does not completely compromise the material, but does have detrimental effects including (1) the substantial production of decomposition products that can foul optics and electronics and provide a fuel source for combustion on both the exterior and interior of a CFRP panel and (2) severe reduction in the compressive strength of the CFRP. Material burn through is not necessary to severely damage the material as resin is completely removed at $T = 450\text{ °C}$ at an energy deposited cost of approximately 9 kJ/gm. This produces volatile decomposition products that ignite at surface temperatures of $1147 \pm 76\text{ °C}$.

IV. Thermal Imagery and Modeling of Laser Irradiated Graphite

The evolving front-side temperatures of graphite samples irradiated at 780-3000 W/cm² with a 1.07- μ m 10-kW fiber laser for 120 seconds were measured at 87.5 Hz and 0.32-mm/pixel spatial resolution using a MWIR thermal camera. Raw blackbody temperatures were calibrated using measured emissivities of irradiated and un-irradiated graphite samples (emissivity data collected by Capt William Bauer). Final temperatures ranged from 2250-3500 K with initial heating rates of 400-1800 K/s. A numerical 3D heat transfer model was used to estimate Arrhenius kinetic parameters and heats of reaction for graphite binder removal and sublimation reactions.

Introduction

Laser weapon systems for strategic missions (missile defense) and tactical missions (point defense and gunship operations) generally rely on high power cw lasers. In a strategic mission, a high power (>100 kW) beam is focused to a small spot size (< 10 cm) on a target to damage or destroy it within a dwell time of < 10 s [1, 2]. Laser systems this large have been pursued for decades without being fielded [3]. The availability of high power, diode pumped solid state and fiber lasers at lower powers (> 10 kW) and shorter wavelengths (1.07 μ m) have recently invigorated the development of tactical laser weapons. This shift to tactical missions greatly increases the variety of potential target materials. Composite materials, including fiberglass and carbon fiber reinforced polymers, are of particular interest [4], [5]. The oxidation and sublimation of carbon has recently been studied in some detail [56, 75]. The thermal response of carbon surfaces to laser irradiation drives the oxidation and sublimation processes, and is the

topic of the current work. By studying fiber laser irradiated graphite, a more complete understanding of carbon fiber materials can be developed.

Combustion plumes from graphite surfaces begin with strong surface oxidation to primarily produce CO at surface temperatures above ~ 1800 K with subsequent gas reactions to produce CO₂ [56, 76]. Strong combustion plumes have been observed for laser intensities below 1 kW/cm^2 [55]. Surface reaction kinetics are driven by both elevated surface and gas plume temperatures with poorly determined activation energies [77, 78]. Plume and surface temperatures can differ by more than 1000 K, particularly when oxygen is highly depleted in the reacting layer [77]. A key objective of the current work is to characterize heating rates, emissivity, and thermal diffusion for graphite surfaces of varying porosity. Significant graphite mass removal and sublimation occurs for irradiances above $\sim 2 \text{ kW/cm}^2$ and surface temperature exceeding 4000 K [55]. Several studies have investigated the sublimation temperature and triple point of graphite using a cw laser at irradiances of 50 kW/cm^2 and pressures as high as 100 atmospheres [80, 81]. In the present work, I observe differences in sublimation for binder and filler material in non-ideal graphite samples.

Pulsed laser ablation (PLA) of graphite has been studied in considerably more detail for carbon nanotube and carbon-containing thin-film manufacturing [82–84] as well as cleaning graphite surfaces in experimental fusion reactors [83]. Laser beam machining (LBM) also commonly makes use of pulsed Nd:YAG lasers to cut and shape a wide array of different materials and has been studied more extensively [84]. Thermal modeling of graphite was used to detect the presence of a thin surface layer with

properties different from the bulk [83] and to characterize the effect of porosity on bulk thermal conductivity [85].

The thermal response of metal surfaces to irradiation by solid state lasers for weapons applications has been recently developed to infer optical and thermal material properties [86]. Material absorption (spectral emissivity) may evolve dramatically, particularly during high laser irradiance testing. I report on the effects of graphite porosity on spectral emissivity at elevated temperatures during the removal of binder material. The optical pyrometry used to characterize surface temperatures requires this knowledge of the evolving surface emissivity.

In the present study, I measure surface temperatures of graphite plates of varying porosities at laser irradiances of 780 – 3000 kW/cm² under buoyant conditions. Temperatures are corrected by initial and irradiated emissivities measured with a hemispherical directional reflectometer (HDR) and used to infer thermal properties, informed by literature values. Graphite sublimation is included as well, with inferred and literature values for reaction parameters. My goal is to include the necessary elements in a model to capture most of the material response of the laser-material interaction at reasonable computational expense, and to validate and refine the model against several experiments.

Experimental

A 10-kW IPG Photonics YLS ytterbium fiber laser at 1.07 μm was used to irradiate graphite targets as shown in Fig. 12. The laser delivered a flat-top profile with 1.8 cm spot diameter containing 86% of the power at average irradiances ranging from 780 –

3000 W/cm². Properties of the graphite plates (10.62 cm x 10.62 cm x 1.27 cm) of different porosities are summarized in Table 5. The samples were mounted vertically in air with no forced flow (buoyant lofting only) conditions. The spatial laser intensity distribution and temporal evolution was imaged on a scatter plate with an IR camera. Graphite surface temperatures were recorded with a FLIR SC6000 mid-infrared camera from 3.8-4 μ m at 0.32-mm/pixel spatial resolution and 87.5-Hz frame rate. Additional diagnostics were used as a part of this test in support of other research objectives, including imaging and non-imaging Fourier Transform Spectrometers (IFTS), visible grating spectrometers, high-speed visible camera, and real-time radiograph (RTR) and are reported on elsewhere [73].

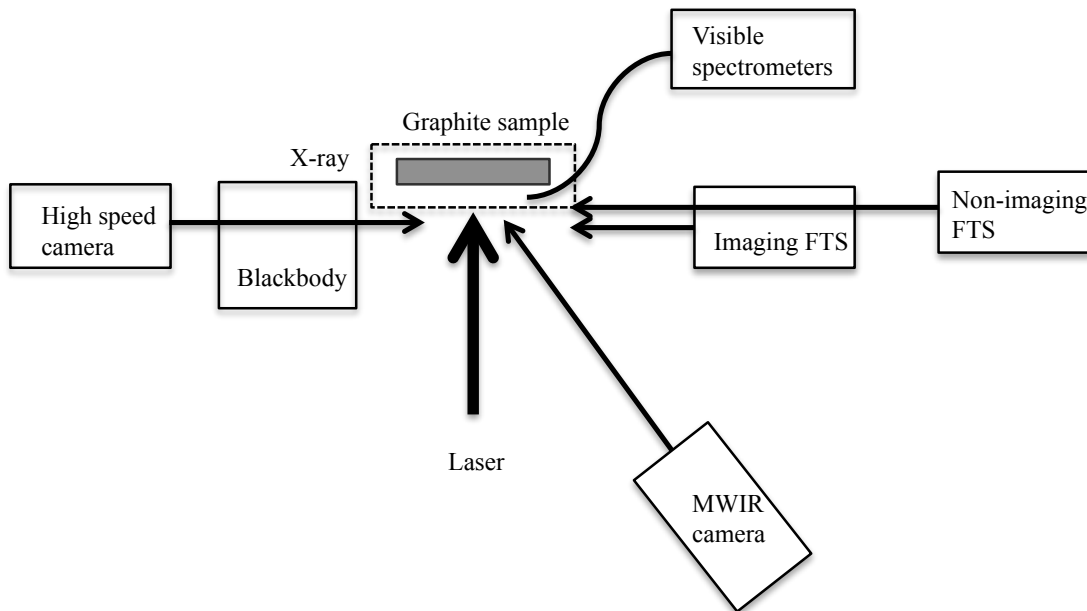


Fig. 12. Experimental set-up

Graphite emissivity measurements were made to determine radiometric temperatures. Hemispherical reflectance measurements were conducted on a Surface

Optics Corp (SOC) 100 Hemispherical Directional Reflectometer (HDR) using a 30° angle of reflection and radiation from a 500°C blackbody. A polarization filter was inserted into the path of the reflected emissions before entering the spectrometer to create either in-plane polarized or perpendicular polarized radiation. Samples were cut into 1"x1"x0.25" squares of each porosity type for measurement in the SOC-100. Post-experiment irradiated samples were cut from spatial locations slightly below the laser spot to obtain reflectance (emissivity) data from as close to hottest laser spot as possible without having to account for the emissivity of re-deposited material above the laser spot. The imaging spot from the SOC-100 reflectance measurements is 1.5-cm diameter. Each reflectance measurement included twelve perpendicular polarized and twelve parallel polarized measurements, which are averaged to form one emissivity measurement. If available, average emissivity measurements were combined to obtain a final average emissivity. Emissivities are reported as averages of perpendicular and plane polarized emissivity. The resulting statistical error was 3.9% for isomolded and less than 2.5% for all other porosities. The largest variation seen between the plane and perpendicular polarized irradiated spectral emissivities was 4.3% observed for coarse porosity graphite; irradiated emissivity variations for all other graphite porosities were less than 1.6%. Using a 3.9% error in the emissivity and assuming a temperature of 3500 K, the standard deviation in the temperature due to emissivity is $\sim \pm 90$ K.

The FLIR SC6000 MWIR camera has a 640 x 512 element InSb detector but was windowed to 320 x 256 pixels to increase the frame rate. The camera was operated with a band pass filter from 3.8-4.0 μm and a neutral density filter of O.D. 1.0 or 2.0 at a stand-off distance of 40 cm and 30° angle relative to the sample surface in the same

horizontal plane. Spatial resolution per pixel was 0.326 mm x 0.316 mm when accounting for off-axis imaging. The camera was calibrated for absolute temperature measurements by observing a wide area blackbody at 323 – 873 K (Electro-Optical Industries model CES600, 6 x 6 in). Characterizing the relationships between detector response, flux, and integrated radiance across the camera's effective bandwidth allowed the equivalent blackbody temperature at the center wavelength (3.9 μm) to be determined. Signal response for the 14-bit readout ranges from approximately 2200 (dark signal) to 16400 counts (saturation), dependent on integration time. At 3600 counts, the SNR was approximately 1800. The temperature dynamic range was improved (600-3500 K) by sequencing through four overlapping integration times ranging from 0.03 to 1.5 ms, reducing the effective framing rate by a factor of 4 to 75-87.5 Hz. The standard deviation in temperature across the camera is $T = \pm 0.4 \text{ K}$.

Results and discussion

Surface Emissivity

Fig. 13 shows the wavelength dependence of the average emissivity for coarse, medium, fine, and isomolded samples before and after laser irradiation. The general trend is one of decreasing average emissivity with increasing wavelength and is observed in a similar manner for all porosities. This trend is consistent with other graphite emissivity studies [17, 66, 89]. Emissivity increases after irradiation for all porosities. Larger scatter is observed in the data at low wavelengths due to lower intensity in this region of the electromagnetic spectrum of the blackbody source.

Fig. 14 shows emissivity as a function of surface temperature for coarse, medium, fine, and isomolded graphite porosities at $\lambda=3.9 \mu\text{m}$. All emissivity measurements are made at true temperatures up to 773 K (SOC-100 heated sample stage) and un-irradiated graphite emissivity is reported at this temperature. Irradiated graphite emissivity is reported at the maximum surface temperature attained during irradiation. Irradiated sample surface temperatures were obtained by averaging the surface temperatures obtained from the FLIR in a 1.5 cm diameter square below the laser spot (the approximate area measured). These temperatures were then corrected for the corresponding average spectral emissivity determined from the SOC measurement of the sample. The general trend observed in the data is an increasing spectral emissivity with temperature.

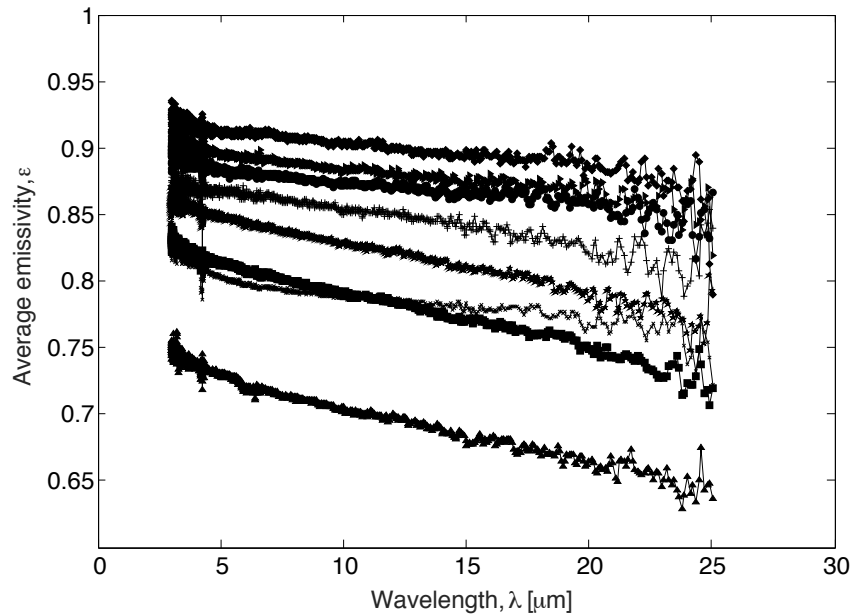


Fig. 13. Dependence of average emissivity (ϵ) on wavelength (λ) for (from top to bottom at 5 μm) fine graphite irradiated (\blacklozenge), isomolded irradiated (\blacktriangleright), medium irradiated (\bullet), fine unirradiated ($+$), isomolded unirradiated (\blackstar), medium unirradiated (\blacksquare), coarse irradiated (\times) and coarse unirradiated(\blacktriangle).

The emissivities at high surface temperatures ($>1500\text{K}$) were utilized to correct surface temperatures recorded from the FLIR. In doing so, I have assumed that the emissivity observed at the highest surface temperatures in Fig. 14 is constant above these temperatures.

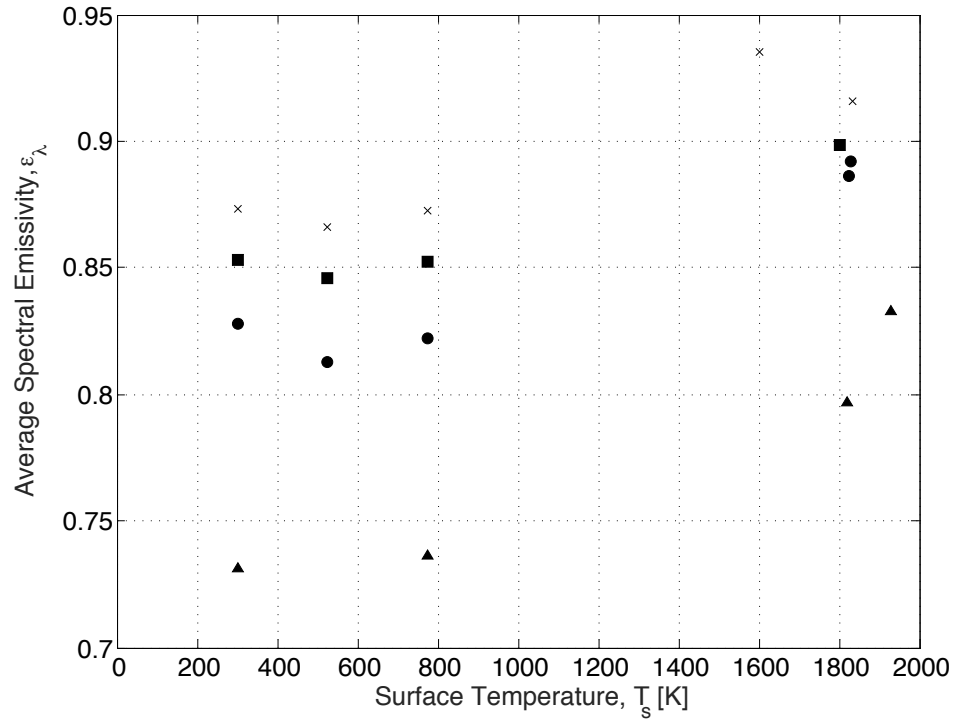


Fig. 14. Dependence of average spectral emissivity, ϵ_λ , at $\lambda=3.9\ \mu\text{m}$ on sample surface temperature, T_s for (●) medium, (▲) coarse, (×) fine, and (■) isomolded graphite samples.

These measurements indicate that laser irradiation produces a permanent emissivity increase at all wavelengths for the graphite porosities studied here. I assume that graphite emissivity has no additional temperature dependence. Increased surface porosity and roughness has been shown to increase surface emissivity [88]. Synthetic

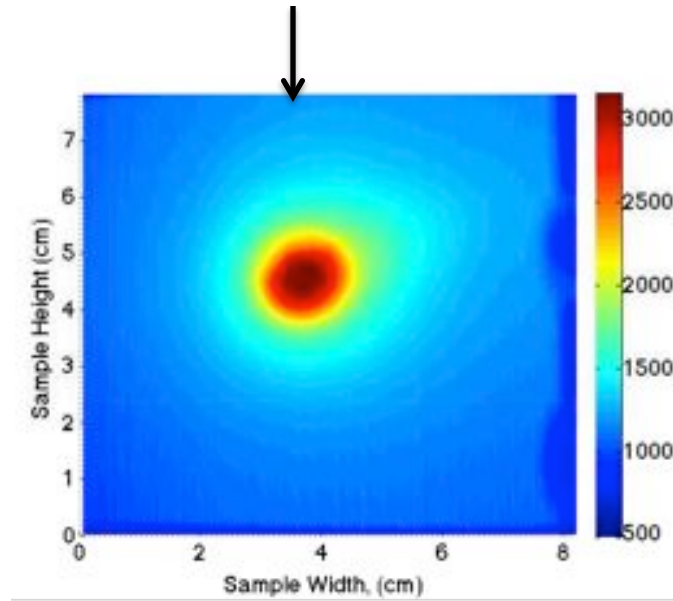
graphite is made by combining graphite particles with coal tar pitch binder and graphitizing the binder at high temperatures. Mass loss during graphitization creates pores in the finished graphite. Further heating during laser irradiation appears to continue this process, removing more binder material and increasing surface porosity, roughness, and emissivity.

Surface temperatures

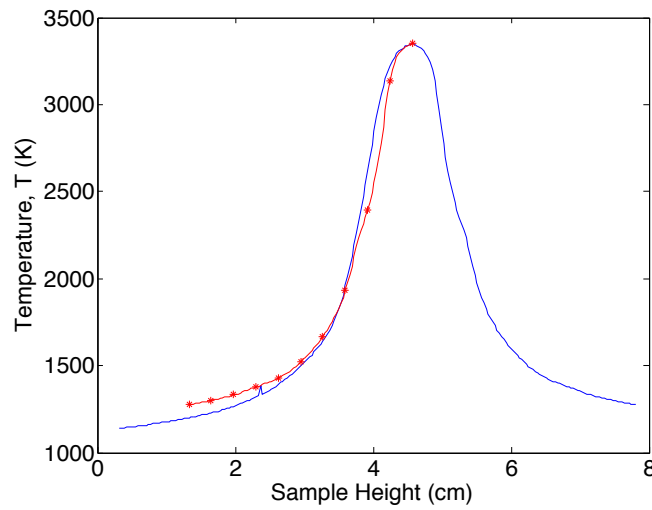
An emissivity-corrected front-surface temperature map of an isomolded plate, irradiated at 1500 W/cm^2 for 120 seconds, is shown in Fig. 15(a). A vertical temperature slice through laser center is shown in Fig. 15(b). Together they show that temperatures are steeply peaked near laser center. Temperatures are within 100 K of the peak (3345 K) out to a radius of 0.27 cm but fall to 1990 K at the 0.9-cm laser spot radius. A slight camera misalignment produced an internal reflection of <1% that artificially increases measured temperatures above and to the right of laser center (temperatures from this region are not used).

The calibrated and emissivity adjusted maximum temperatures at laser center are shown throughout the 120 second test in Fig. 16 for isomolded graphite and laser powers ranging from 780-3000 W/cm^2 . As laser power increases, initial heating rates become increasingly rapid (ranging from 400-1800 K/s) and reach steady state temperatures of 2500-3500 K more quickly. There is an intermediate transitional period between the initial linear heating rate of the graphite sample and the gradual heating rate, leading up to steady state temperature that is likely due to residual binder removal. It appears that this reaction is endothermic, momentarily slowing the surface heating rate.

At laser center, temperatures and mass removal rates are sufficient to support surface combustion, a reaction that could produce an apparent surface temperature



(a)



(b)

Fig. 15. (a) Surface temperature map and (b) vertical temperature profile (at arrow) of isomolded graphite (7.62 cm x 7.62 cm x 1.27 cm) irradiated at 1500 W/cm² for 120 seconds (0.06, 0.2, 0.6, and 1.5 ms integration times). Temperatures above laser center are reflected about the peak to illustrate symmetry (*).

increase. However, in other work [77], we investigate laser irradiated graphite surface plumes with an imaging Fourier Transform Spectrometer and find that emission at $3.9\text{ }\mu\text{m}$ is very low, indicating that observations are of surface temperatures.

Higher porosity graphites (medium and coarse) were found to have a heating response similar to isomolded graphite under the same conditions (Fig. 17). Isomolded and medium graphite results agree particularly well, likely a function of the similarity in their irradiated emissivity. Irradiated coarse graphite emissivity is significantly lower (0.81) and adjusts observed temperatures upward. An emissivity of 0.9 is required to

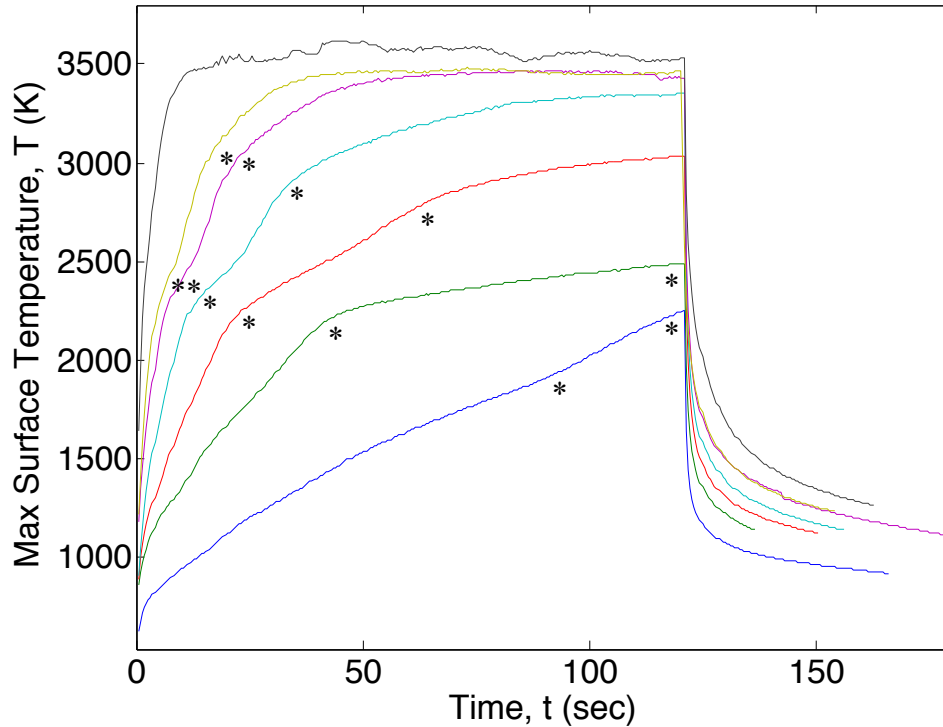


Fig. 16. Temperatures at laser center during 120 second test at laser powers from 780-3000 W/cm². Best labeling scheme? Isomolded graphite plates at 780 W/cm², 1000 W/cm², 1250 W/cm², 1500 W/cm², 1750 W/cm², 2000 W/cm², and 3000 W/cm². Beginning and end of binder removal is labeled with *.

bring steady-state temperatures of coarse graphite into agreement with isomolded and medium porosity graphite for the 1500 and 2000 W/cm² cases. However, at 2000 W/cm², $\varepsilon = 0.81$ leads to better temperature agreement.

As shown in Table 5, the beginning of the binder removal period appears to begin at lower temperatures at lower laser powers, reaching a consistent initial temperature of approximately 2250 K. This may signal a shift in the binder removal reaction mechanism. At lower laser powers, the transition is not completed before the end of the test. Heating is so rapid at 3000 W/cm² that the effect of the transition region is difficult to detect. The increase in temperature after 120 s is non-linear with laser power and appears to reach a maximum surface temperature limit by approximately 1750 W/cm².

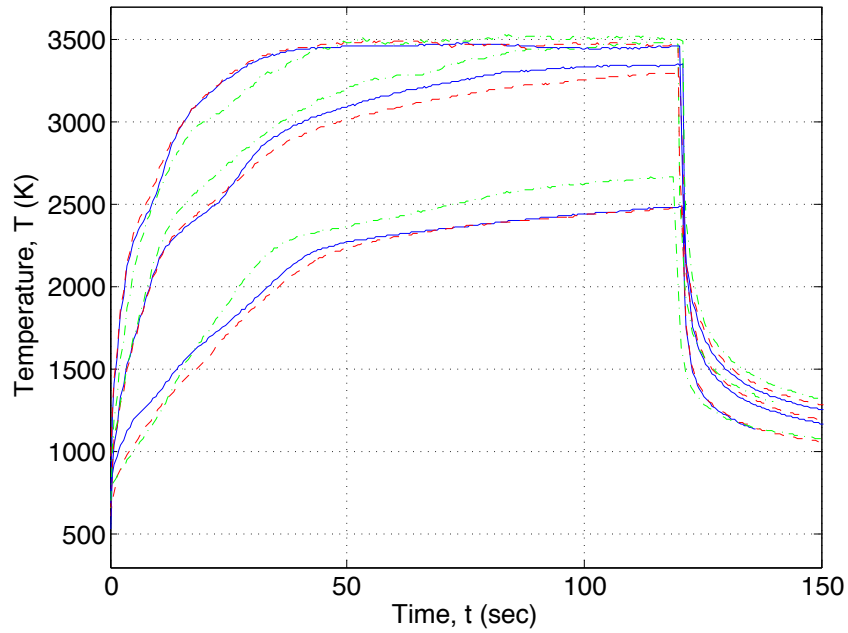


Fig. 17. Temperatures at laser center during 120 second test at laser powers of 1000 W/cm², 1500 W/cm², and 2000 W/cm² for isomolded (solid blue), medium (red --), and coarse (-.-) porosities.

Table 5. Characteristic Surface Temperatures
(Estimated from plot, from * locations)

Graphite Type	Laser Intensity (W/cm ²)	Binder Removal Begin (sec, K)	Binder Removal End (sec, K)	Final Max Temp (K)	Increase (ΔK)
Isomolded	780	89.1, 1896	120, 2249	2249	---
Isomolded	1000	41.6, 2193	120, 2485	2484	235
Isomolded	1250	20.6, 2180	61.3, 2762	3034	550
Isomolded	1500	11.9, 2241	32.5, 2860	3348	314
Isomolded	1750	7.8, 2314	18.7, 2885	3428	80
Isomolded	2000	5.0, 2277	13.3, 2873	3464	36
Isomolded	3000	---	---	3527	63

As shown in Fig. 18 these smaller temperature increases coincide with a decrease in the fraction of incident laser energy that is re-radiated from the surface according to the Stefan-Boltzmann law. The initial stage of cool down after the laser is turned off is very rapid due to radiative cooling. Later on, the cool down rate decreases drastically and is independent of laser power, instead controlled by thermal diffusion away from the laser spot. The average temperature of the entire sample increases with incident laser

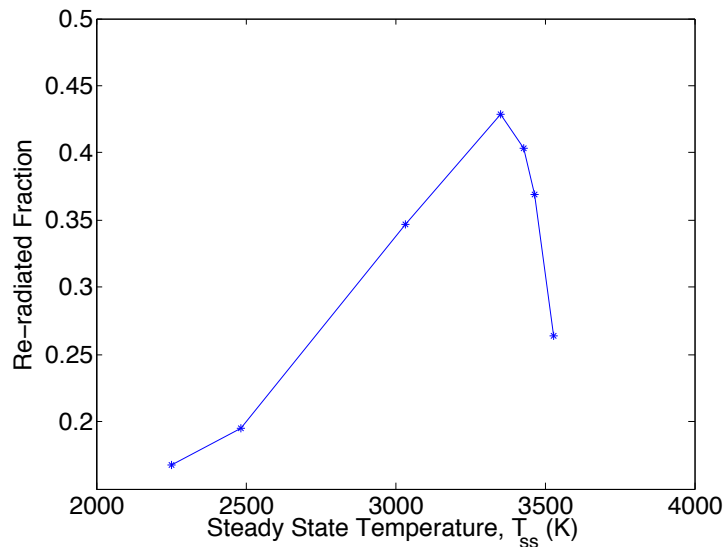


Fig. 18. The fraction of incident laser energy that is re-radiated from the graphite surface peaks at 3350 K (1500 W/cm²).

power due to being thermally isolated by small mounting points. The entire sample is red-hot for several minutes after the laser is turned off.

Thermal modeling.

A simple thermal model was used (coded in MATLAB®) to interpret the laser-graphite interaction and resulting heating. I used a 3D explicit finite difference model based on Fourier's heat diffusion equation with source terms for binder removal and graphite sublimation kinetics (Eq. 19) and Neumann boundary conditions for laser absorption, surface emission, and convection (Eq. 20).

$$\rho C_p \frac{\partial T}{\partial t} = k_x \frac{\partial^2 T}{\partial x^2} + k_y \frac{\partial^2 T}{\partial y^2} + k_z \frac{\partial^2 T}{\partial z^2} + \frac{dT_s}{dt} + \frac{dT_b}{dt} \quad (19)$$

$$k \frac{\partial T}{\partial x, y, z} = -h(T - T_\infty) - \varepsilon \sigma (T^4 - T_\infty^4) + \alpha I \left(1 - \frac{dm_s}{dt} \frac{C_s}{dx dy} \right) \quad (20)$$

where ρ is density, C_p is specific heat, k is thermal conductivity, h is the convection coefficient, ε is the grey body emissivity, σ is the Stefan-Boltzmann constant, T_∞ is ambient temperature, α is the surface absorptivity, and I is the laser intensity. The computational mesh was 30 x 30 uniform elements in the plane perpendicular to the incoming laser, with 5 elements in the parallel, thickness direction.

The power distribution of the laser spot was recorded throughout the experiment by imaging the beam on a spinning scatter plate on 1-s intervals. The raw image signal was calibrated to laser intensity using total power measurements. This calibrated image was resized to match the model mesh and used directly as the laser input to the model. The absorption depth of graphite is controlled by porosity but in all cases is much thinner than, and completely absorbed by, the surface element.

Graphite densities, particle sizes, conductivities, and porosities as reported by the manufacturer are reproduced in Table 6. Specific heat, C_p , of graphite has strong temperature dependence, starting from a room temperature value of approximately 710 J/kg K and increasing non-linearly to reach a value of near 2200 J/kg K at 2500 K.

Table 6. Graphite sample properties

Graphite	Density, ρ (g/cm ³)	Grade, Particle size (mm)	Reported Cond. (W/m K)	Surface Emissivity, ϵ ($\lambda=3.9 \mu\text{m}$)		Porosity (% vol)
				RT	Irradiated	
Coarse	1.55	GR-250 6.35	---	0.735 ± 0.004	0.809 ± 0.02	----
Medium	1.72	GR-060 1.524	130	0.818 ± 0.007	0.899 ± 0.017	21
Isomolded	1.82	GM-10 0.2032	83	0.852 ± 0.007	0.899 ± 0.035	12
Theory	2.26	----	----	----	----	----

Various measurement techniques, functional forms, and temperature ranges are reported in the literature. Two results are used here in combination (Fig. 19) to cover the temperatures encountered in these experiments [91, 92].

298–2500K:

$$C_p(T) = 1405.13 + 39.748 \times 10^{-2}T - 71.128 \times 10^6 T^{-2} \quad \text{J / kg K} \quad (21)$$

1500–3000 K:

$$C_p(T) = 1619.83 + 30.179 \times 10^{-2}T - 3.702 \times 10^{-5}T^2 \quad \text{J / kg K} \quad (22)$$

The two curves intersect near 1500 K. The more recent values given in reference [90] are used for temperatures greater than 1500 K and are extrapolated to 4000 K. The resulting composite $C_p(T)$ relation is fit with a 8th-order polynomial.

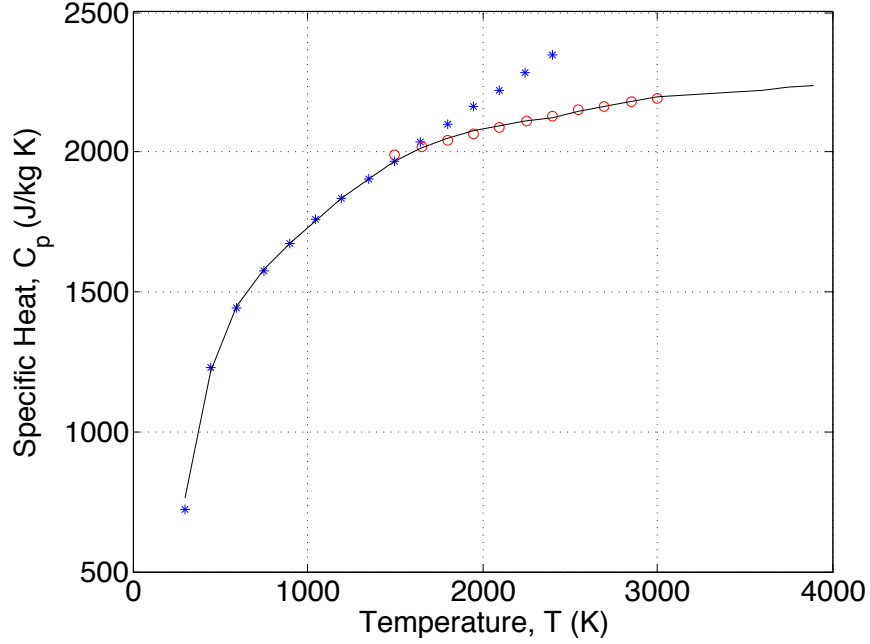


Fig. 19. Temperature dependence of specific heat used in model. (*) Equation 1 (o) Equation 2, and (—) composite equation

Thermal conductivity, $k(T)$, has a strong temperature dependence as well.

Graphite conductivity has a peak value near room temperature and a steep drop-off at both low and high temperature. Several overlapping data sets at elevated temperatures [91] were combined and fit to a function of the form $k(T) = AT^b$. This data is shown in Fig. 20 and indicates an approximate temperature dependence as

$$k(T) = 3600T^{-0.6} \quad (23)$$

High-temperature conductivities (above 3000 K) are extrapolated from this relationship. Most available thermal properties data is for AXM-5Q1 POCO graphite, which is similar in density to isomolded and medium porosity graphite used in this work. Conductivity is assumed to be isotropic.

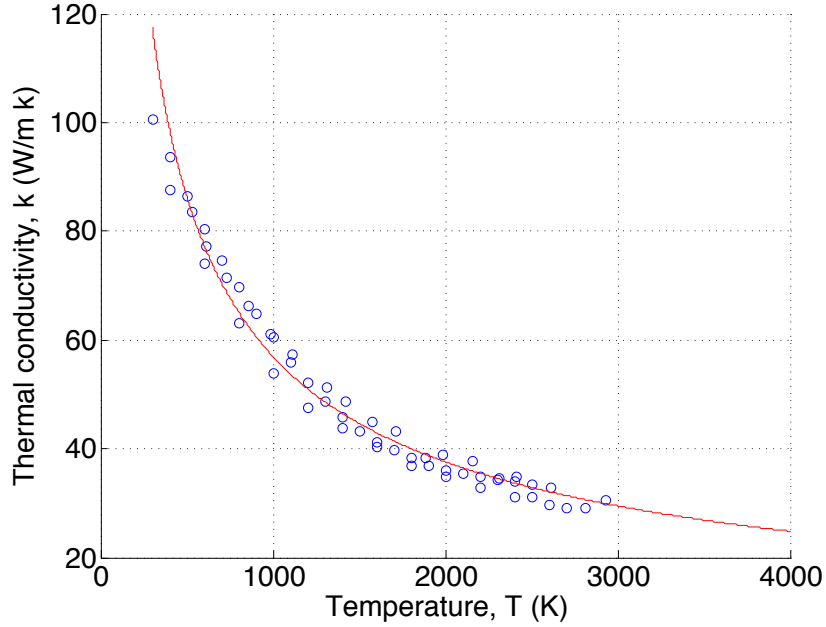


Fig. 20. Thermal conductivity temperature dependence (o) from reference [91], and (—) power law fit

Energy flow due to conduction is governed by the material thermal diffusivity (α_d) which combines material density (ρ), specific heat (C_p), and thermal conductivity (k) as

$$\alpha_d = k / \rho C_p. \quad (24)$$

Thermal diffusivity, with functional values for k , ρ , and C_p defined above, decreases rapidly from a room temperature value of approximately $1.0 \text{ cm}^2/\text{s}$ to values in the range of $0.1\text{-}0.2 \text{ cm}^2/\text{s}$ at temperatures $> 1200 \text{ K}$. These values are comparable to aluminum (Al 6061-T6, $\alpha = 0.6 \text{ cm}^2/\text{s}$) but significantly less than in-plane diffusivity of high-purity pyrolytic graphite ($\alpha = 12 \text{ cm}^2/\text{s}$).

Values related to boundary conditions include emissivity (ϵ), convection coefficient (h_{conv}), and absorptivity (α). As previously described, the spectral emissivities of both irradiated and un-irradiated samples of each porosity were measured at temperatures up to 773 K. The graphite sample is assumed to be a grey body with an emissivity as measured at 3.9 μm , seemingly at odds with the spectrally dependent emissivity in Fig. 13. However, this assumption preserves the use of the Stefan-Boltzmann law in calculating total emission for simplicity and computational efficiency. Furthermore, as described by the Wien displacement law, the wavelength of maximum emission shifts from approximately 10 μm at room temperature to < 3.9 μm by 740 K (and 1 μm at 2900 K). Along with the relatively small variation in ϵ at wavelength < 3.9 μm in Fig. 13, this supports the approximation that the emissivity at 3.9 μm is a reasonable value for the bulk of the thermal emission under the conditions studied here and is used in the model to estimate boundary losses due to radiation according to the Stefan-Boltzmann law. For similar reasons the emissivity at 3.9 μm is also used as an absorptivity value for laser surface absorption according to Kirchhoff's law.

Convection loss is approximated using calculated surface temperatures, ambient room temperature and an estimate of convective heat transfer coefficient under free convection. The free convection coefficient is reported in the range 2-25 W/cm²K [67]. A more precise value can be calculated for only the simplest flow situations and in practice heavy reliance is placed on empirical results. Empirical relationships do exist for free convection of a vertical isothermal plate [67]. However, in this work the graphite plate is not isothermal and the gas boundary layer around the laser spot is likely heavily

influenced by turbulence, surface flames, formation of a buoyant jet, and mass transfer from binder and graphite sublimation in varying amounts [67]. These factors all serve to increase airflow and mixing at the surface, increasing the apparent convection coefficient. A factor of two increase from the maximum value of 25 W/cm²K quoted above is estimated here and agrees reasonably well with the model and radial surface temperatures. In the absence of the laser and its associated convective effects, cool down rates suggest a more appropriate value of 10 W/cm²K.

Graphite is thermally robust, but does begin to degrade under high laser power and high steady state temperatures. Mass loss under these conditions could be caused by surface oxidation, graphite binder removal, or graphite sublimation. Oxidation near the sample surface is a complex process but is generally limited by the concentration of surface oxygen. The pitch that binds graphite particles during manufacture is partially graphitized during treatment at high temperature (2500-3000 °C) [12]. At laser powers above 1500 W/cm² and surface temperatures from 3400-3600 K, material removal forms a visible crater at laser center. At atmospheric pressure, the sublimation temperature of graphite has been reported to be 3800-4000 K [94, 95] with an endothermic heat of sublimation of 711 kJ/mol [94].

Graphite binder (*b*) removal and sublimation (*s*) reactions were incorporated into the model as shown in Equations 9-10 and calculated as separate first order Arrhenius reactions with energy loss proportional to mass loss:

$$\frac{dm_b}{dt} = m_b A_b \exp\left(\frac{-E_b}{RT}\right) \quad (25)$$

$$\frac{dT_b}{dt} = \Delta H_b \frac{dm_b}{dt} \quad (26)$$

$$\frac{dm_s}{dt} = m_g A_s \exp\left(\frac{-E_s}{RT}\right) \quad (27)$$

$$\frac{dT_s}{dt} = \Delta H_s \frac{dm_s}{dt} \quad (28)$$

The mass of each model element is assumed to be either graphite or binder with a relative proportion determined as a part of the model fit. To simplify the model and reduce the number of independent parameters, it was assumed that the activation energies (E_b and E_s) are equal to the enthalpies of the binder removal (ΔH_b) and sublimation (ΔH_s) reactions. It was reasoned that the activation energy required to liberate the carbon atom from the sample, with formation of products in the gas phase, thermally isolated from the solid sample, is the same energy that is consumed during the reaction.

Decreasing cell density was used to represent binder removal and the reaction ceased for a given element when all binder was removed. Mass loss due to sublimation was recorded throughout the simulation, but for simplicity, the physical dimensions of the model mesh were not changed to reflect a laser-formed crater.

The inclusion of graphite sublimation into the thermal model provides a mechanism to limit surface temperatures at high irradiance to approximately 3600 K as observed in Fig. 16 – when more energy is available, more graphite is sublimated, potentially leading to laser burn-through. However, this approach, while producing observed temperatures, leads to total mass removal approximately 2X that which is observed. To address this inconsistency, another term is incorporated into the model that only activates at very high irradiance (last term in Eq. 20). This term incorporates reduced laser transmission to the graphite surface due to absorption and scattering of a vigorous surface sublimation plume and flame. It reduces laser surface absorption in

proportion to high surface sublimation rates per area. This modification is in agreement with hyper-spectral imaging of graphite sublimation plumes that finds that at high temperatures, with significant sublimation, plume temperatures increase beyond that of the adjacent surface temperatures [55], possibly due to increased plume absorption. The proportionality constant, C_s , is determined by fitting the model results to both observed steady-state temperatures at high irradiance and observed total mass removal, and is given in Table 7. It provides a measure of how absorptive the sublimated graphite particles are.

Model results

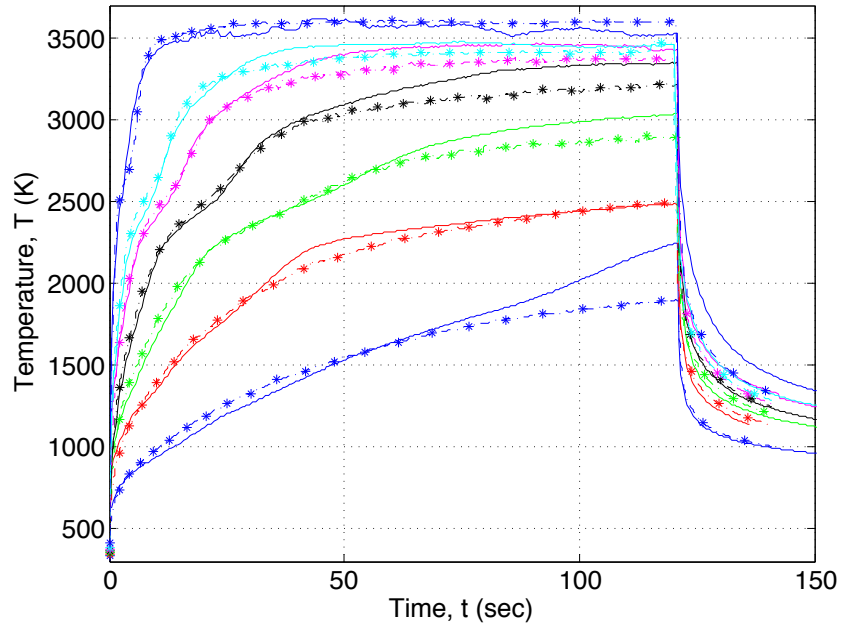
To constrain the model, it was assumed that graphite specific heat is less variable as a function of grade than either density or conductivity. It was reasoned that specific heat is largely dependent on the local nature and number of C-C bonds, which is driven by the electronic structure of the carbon atom and more consistent for all graphite materials. In contrast, density varies based upon the number and size of macroscopic voids and conductivity is driven by the long-range order and purity of the graphite, which can vary widely. In fitting the model to the experimental data, $C_p(T)$ is fixed as described in Eq. 21 and 22 above, ρ is based initially on reported values (Table 6, decreasing as binder is removed), and $k(T)$ is varied within a literature derived functional form, $k(T) = AT^b$. The commercial grades of graphite studied here were found to require slightly higher conductivities than the graphite reported in the literature. Model agreement was much improved for $k(T) = 4800T^{0.6}$.

Energy transfer between the graphite and the environment is primarily through absorption and emission. As previously covered, emissivity was measured and found to

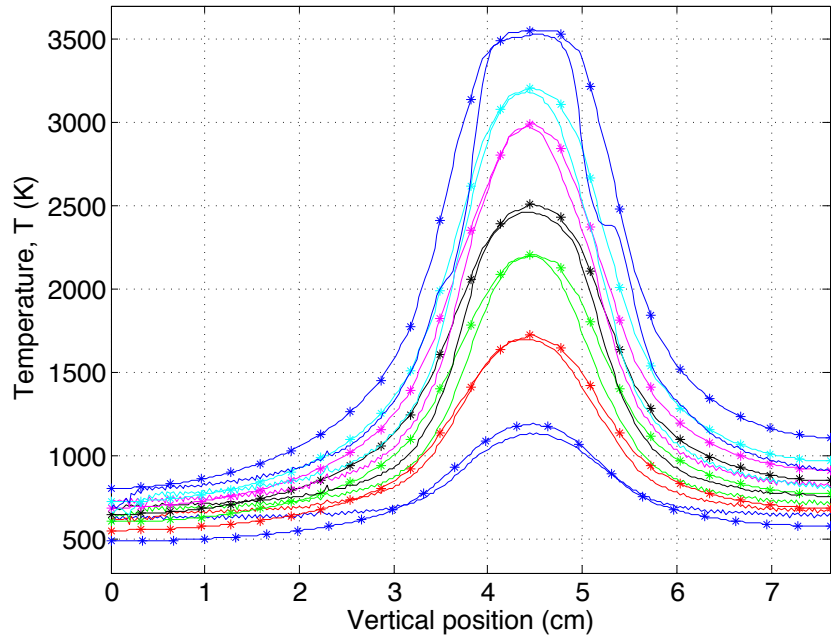
differ for pre and post-irradiated graphite. I assume that the emissivity change results from the binder removal, estimated to occur between approximately 1700-2400 K (see Fig. 16). The emissivity change was phased in linearly through this temperature range. Changes in emissivity were assumed to be permanent and did not revert back to previous values upon cool-down. No additional temperature dependence is assumed here apart from that produced by the binder removal.

The observed and modeled temperatures are compared in Fig. 21. Part (a) compares temperatures at laser center as a function of time and part (b) shows the agreement in radial temperature, vertically from bottom to top, through laser center. Only isomolded porosity is shown here – medium and coarse porosity graphite have similar temperature profiles (see Fig. 17), and the temperatures of all are predicted reasonably well with the same model though somewhat less in the case of coarse graphite.

The necessary kinetic parameters for binder removal as outlined above were determined iteratively, subject to several simplifying constraints. The first constraint is that the activation energy equals the heat of reaction, as previously mentioned. The second is that the binder removal reaction near laser center must follow the momentary cooling trend observed in the transitional region between initial heating and steady state temperatures as seen in Fig. 21(a). Third, total mass loss throughout the experiment must agree with that observed, with special emphasis on irradiances between 1250-2000 W/cm². This produces three values that must be balanced to satisfy these constraints: percent binder initially present, binder removal activation energy (which equals the heat of reaction), and the pre-exponential factor for the binder removal reaction. The



(a)



(b)

Fig. 21. Isomolded graphite comparison between measured (—) and modeled (-*-) temperatures at laser powers of 780 W/cm^2 (*), 1000 W/cm^2 (*), 1250 W/cm^2 (*), 1500 W/cm^2 (*), 1750 W/cm^2 (*), 2000 W/cm^2 (*), and 3000 W/cm^2 (*) at (a) laser center during entire test and (b) vertical temperature profile through laser center at 21 seconds.

temperature at the start of the transitional region primarily defined the activation energy. The total amount of cooling available was determined by the amount of binder present and the overall rate (depth of cooling feature) was determined by the pre-exponential factor, A_s .

Kinetic parameters for graphite sublimation were determined similarly. In this case, the heat of sublimation of graphite is well established in the literature and was not varied. As before, it was used as the activation energy of graphite sublimation as well. Without the inclusion of sublimation, predicted steady-state temperatures at irradiances $> 2000 \text{ W/cm}^2$ are higher (4200 K at 3000 W/cm^2) than those observed, which appear to reach a ceiling around 3600 K. Sublimation is an endothermic reaction that provides an energy sink to cool the surface to observed temperatures. The rate of sublimation (and thus the pre-exponential factor) can be estimated from the amount of cooling required to produce observed temperatures. However, cooling via sublimation alone produces values for total mass loss approximately 2X higher than those observed. Including the sublimation screening term reduces the energy reaching the graphite surface during heavy sublimation and reduces the rate of sublimation necessary to consume it, more closely matching the observed mass losses. Values for final model parameters are summarized in Table 7. Predicted and observed total mass loss during these experiments is provided in Fig. 22 and has been described in further detail recently [73].

In general, the model slightly underestimates mass loss at lower irradiance, possibly due to omission of lower energy reactions that produce small amount of mass loss. This may also explain anomalous temperature increases at lower irradiances. At

higher irradiance, the model slightly overestimates mass loss, perhaps due to binder re-arrangement reactions that consume energy but do not necessarily result in mass loss.

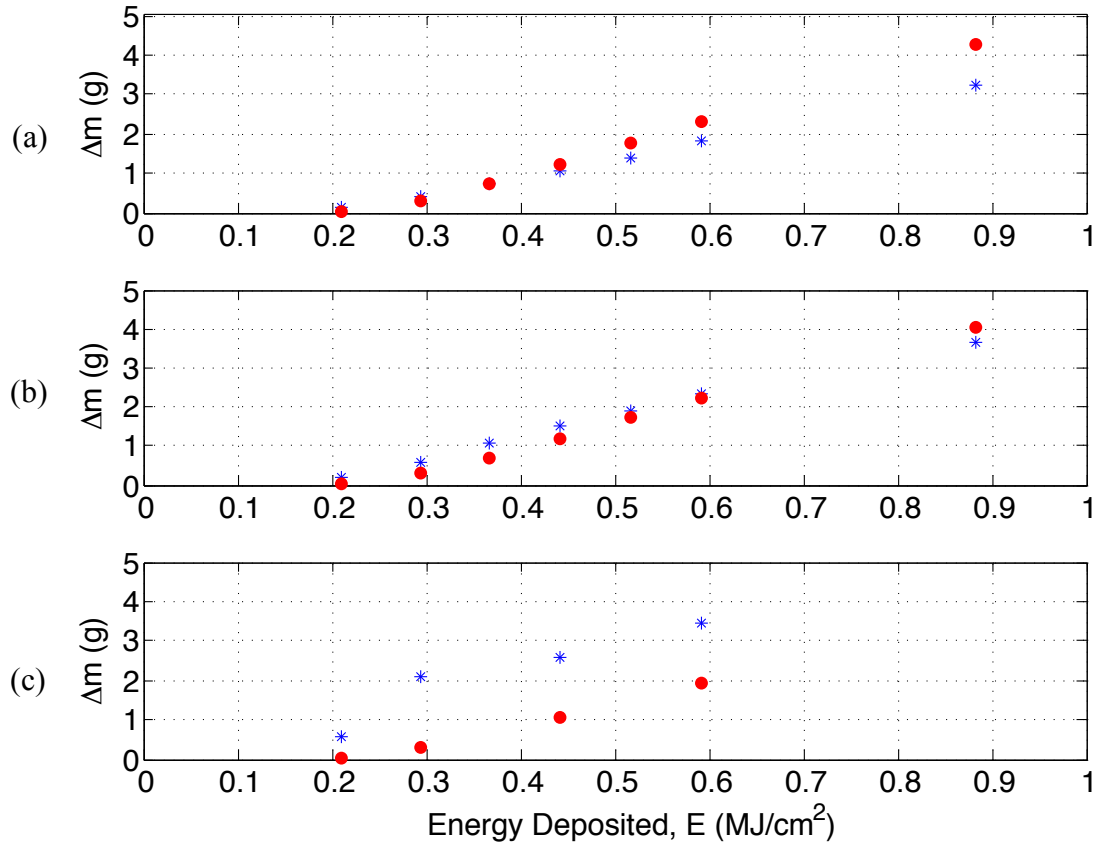


Fig. 22. Total actual (*) and modeled (•) graphite mass loss as a function of total energy deposited for (a) isomolded (b) medium and (c) coarse porosity.

Table 7. Model parameters

Parameter	This work
Thermal conductivity (W/m K)	$4800 \cdot T^{(-0.6)}$
Specific Heat (J/kg K)	720 - 2240
	8th order polynomial
Density (g/cm ³)	1.55 – 1.82
Binder fraction (w/w)	0.4
A_b (s ⁻¹)	4×10^6
E_b (J/mol)	3.5×10^5
ΔH_b (J/kg)	$- 29.2 \times 10^6$
A_s (s ⁻¹)	3×10^9
E_s (J/mol)	7.116×10^5
ΔH_s (J/kg)	$- 59.3 \times 10^6$
h_c (W/m ² K)	50 (laser on) 10 (laser off)
ϵ	0.74 – 0.9
α	0.74 – 0.9
C_s (s cm ² /kg)	60×10^3

Conclusions

Front-side temperature maps of high power laser irradiation of graphite targets of varying porosities at 1.07 μm and irradiances ranging from 0.78 – 3 kW/cm² were recorded at high frame rate and spatial resolution. Emissivity of un-irradiated graphite up to 773 K and graphite irradiated at temperatures up to 1800 K was measured from 2-25 μm . Emissivity ranged from 0.6 to 0.8, decreased with wavelength, increased after laser irradiation, and is generally higher for less porous grades of graphite. Consideration of the evolution of surface emissivity is critical to the accuracy of surface temperature maps, with a temperature uncertainty of approximately 20 K for each 0.01 difference ($\Delta\epsilon$) from a true value of $\epsilon = 0.9$ at 3000 K. Surface gas plume emissivity at 3.9 μm is < 0.01 and does not significantly contribute to measured temperatures.

Initial heating rates at laser center of 400 –1800 K/s and steady-state temperatures of 2500 – 3500 K are achieved. Radiative cooling dominates with as much as 43 % of the laser power re-radiated for surface temperatures of 3350 K. Heating rates temporarily decline for surface temperatures of 2200 – 2900 K, due to binder removal. Temperatures reach a steady state temperature when absorbed laser energy balances loss mechanisms, with a maximum temperature approximately 3600 K, approaching the sublimation temperature. The radial distribution of temperatures is dramatic, with surface temperature declining by as much as 2000 K or 60%, at distances of three times the laser spot radius, despite graphite thermal diffusivity greater than typical metals. Edge temperatures can be as high as 1500 K.

Temporal and spatial temperature changes throughout the 120-s test were modeled to determine temperature-dependent conductivity and kinetic parameters of graphite binder removal and graphite sublimation. The model was most sensitive to emissivity, which controlled laser absorption, temperature measurement, and radiative cooling. This set the steady-state temperature for each laser power and determined target temperatures. Spatial temperature profiles are most dependent on the proper temperature dependence of thermal conductivity. First-order Arrhenius pre-exponential factors and activation energies for binder removal and graphite sublimation were found to be $4 \times 10^6 \text{ s}^{-1}$ and $3 \times 10^9 \text{ s}^{-1}$ and 3.5×10^5 and $7.1 \times 10^5 \text{ J/mol}$, respectively.

V. Carbon Fiber Composite Laser-induced Compressive Strength Reduction

Residual compressive strength of laser-irradiated CFRP was tested as a function of both irradiance and distance away from laser center during a 120 s laser exposure and as a function of irradiance level at the laser spot for a 10 s laser exposure. Visibly undamaged CFRP directly adjacent to the laser damaged area was found to have compressive strength reductions of 10-50% with no further reductions beyond this region. All laser damage is localized within a radius approximately 2-4X that of the laser spot, with smaller damage zones for shorter duration laser exposure. At the laser spot, residual compressive strengths of 27-59% remained when combustion was limited to the front side only, decreasing to 5-10% for both front and backside flames. In both cases, samples ignited in 0.1-2.5 s.

A previously developed thermal model incorporating matrix decomposition reactions and changing thermal and optical properties was used to model the resulting compressive strength of the irradiated strips. The additional heat flux from surface combustion was required to accurately predict CFRP strength, particularly when backside combustion is present. The modified model was used to predict final distributions of virgin resin, dehydrated resin, char, and bare fiber and estimate the compressive strengths of intermediate states dehydrated resin and char to be 128 MPa and 48 MPa, respectively.

Introduction

The use of polymer composite materials continues to grow, both in the number of applications and in weight percentage of new vehicles. As such, the response of polymer composite materials to radiant heating and high temperatures continues to be of great

interest for the purposes of predicting and improving their fire resistance and has been studied extensively [10]. Increased usage of polymer composites has also encouraged the development of new and more efficient manufacturing methods, including laser beam cutting and machining [84].

The increasing adoption of composite materials also increases the likelihood that these materials could comprise a target of interest in a laser lethality scenario. This requires the work done in composite fire properties and laser machining to be extended. High power lasers deliver energy at very high rates ($> 1000 \text{ W/cm}^2$), much higher than the $5\text{-}10 \text{ W/cm}^2$ delivered to a composite surface by a hot surface fire [10]. This produces very high surface heating rates and temperatures that are better measured optically than with embedded thermocouples as is typical in fire testing. Lasers are also monochromatic with well-defined spatial beam profiles. This requires a more thorough understanding of the optical properties of composites. High power lasers are also typically continuous (cw), not pulsed as is typical in laser beam cutting and machining. This is desirable in machining as laser pulses produce very high peak irradiances to vaporize material while limiting the total energy imparted and resulting thermal damage to surrounding material. However, pulses are more difficult to propagate through the atmosphere.

Interest in high power laser weapon systems has shifted in recent years from strategic missions such as missile defense to tactical missions including gunship operations and port defense. This greatly increases the number of potential target materials and engagement scenarios, complicating efforts to empirically test and measure laser effects. However, the response of composite materials is complex complicating

modeling efforts. A hybrid approach may be found by using a subset of experiments with enhanced diagnostics to refine models developed by the fire science community. These models can then be adapted for untested scenarios and materials.

Experimental

Carbon fiber reinforced polymer (CFRP) composite panels from Protech Composites of 3.2-mm thickness were irradiated by a 2-kW cw IPG Photonics YLS ytterbium doped fiber laser at 1.07 μm in two configurations as shown in Fig. 23. In the first configuration, large panels (30.48 cm x 15.24 cm) were irradiated with a central spot of 2.4-cm ($1/e^2$) diameter at total powers ranging from 243-1401 W, producing average irradiances of 84-492 W/cm^2 for 120 s. In the second configuration, the large panels were cut into strips (2.54 cm x 15.24 cm) and irradiated with a 1.65-cm ($1/e^2$) diameter central spot at total powers ranging from 129-664 W, producing average irradiances (75% of $1/e^2$ radius) of 100-525 W/cm^2 for 10 s. Both sample types were irradiated with the long sample axis parallel with the horizontal. All the panels were manufactured by layering 8 plies of 6K (6000 filaments per tow) 2x2 twill weave carbon fiber fabric in a mold and injecting a Bisphenol-A-based epoxy resin system under vacuum (final thickness 3.2 mm).

The spatial distribution and temporal dependence of the fiber laser was recorded using a beam splitter and a calibrated InGaAs NIR camera (Goodrich SU320KTS-1.7RT) to illuminate and record a stationary scatter plate. Irradiance reached peak levels in approximately 0.5 s and irradiance σ per pixel varied from ± 0.4 -1.7%, approximately Gaussian in shape with several hot spots near laser center. Tests were set up on an open

optical table with ceiling mounted ventilation hood (upward flow speed approximately 0.2 m/s) and recorded with a 30 Hz visible witness camera. More detail can be found in Chapter III.

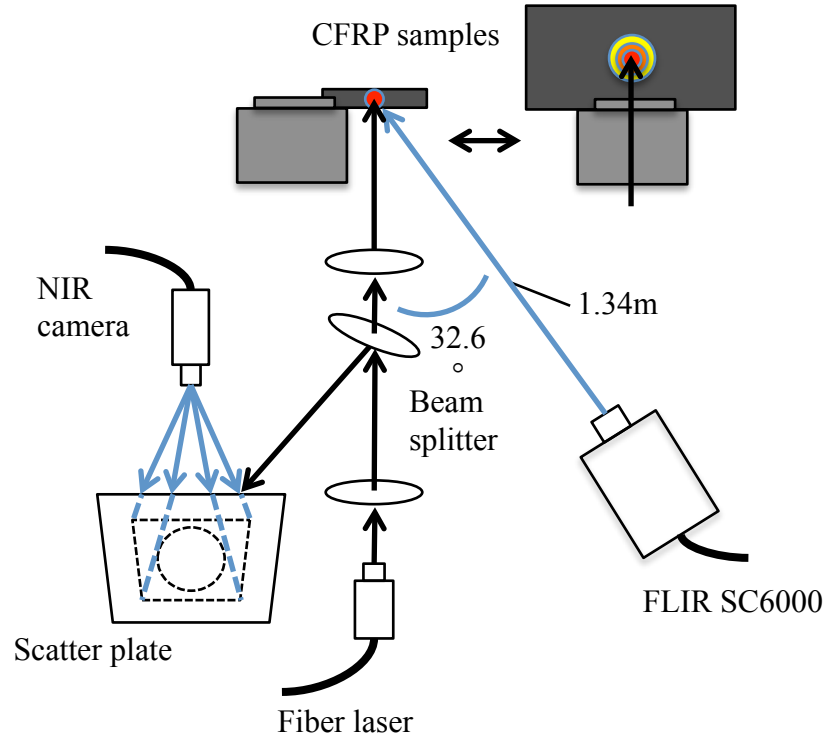


Fig. 23. Testing Schematic

Surface temperatures were measured with a FLIR SC6000 MWIR camera from 3.8-4.0 μm . Calibrations were performed with a wide area blackbody and corrected using previously measured emissivities. Emissivity at 3.9 μm is 0.93 for virgin resin and dehydrated resin, drops to 0.86 for char and decreases with temperature for bare fiber according to $0.792 - 0.06 (T(K)/1000)$. For more detail, please refer to Chapter III.

The irradiances tested here ignited the sample surface in 0.1 - 2.5 s. For the larger panels, the flame was extinguished manually 20-30 s after laser off. For the smaller

strips, the flame was allowed to burn, sustained by volatiles from the decomposing sample, until it cooled and self-extinguished at the end of the test. For lower irradiances (100-205 W/cm²) flames self-extinguished after 2-5 s; for higher irradiances (295-525 W/cm²) it took 45-50 s. The significant increase corresponds to backside combustion, which is absent at the lower irradiances.

The residual compressive strength of the irradiated CFRP panels was tested on a 5 KIP MTS mechanical testing machine. Prior to testing, the large panels were cut into strips with dimensions matching the pre-cut strips (2.5 cm x 15.24 cm) as shown in Fig. 24. The panel area on both sides of laser center (2.4 – 3.1 cm depending on irradiance) could not be machined due to extensive material degradation from the laser and surface flame. Approximately 2.3 mm of material was lost due to each cut. The long edges of all testing samples were smoothed with diamond tooling to eliminate initiation sites for premature testing failure.

All testing samples were shortened to resist buckling failure, with 2.5 cm of material removed from each end, and fitted with a 2.5 cm tab, leaving a gauge section of approximately 5 cm with the laser damaged area in the center. Compression tests were run in displacement control, with a ramp rate of 0.025 mm/sec, and terminated after a sharp drop (> 50%) of sustained load.

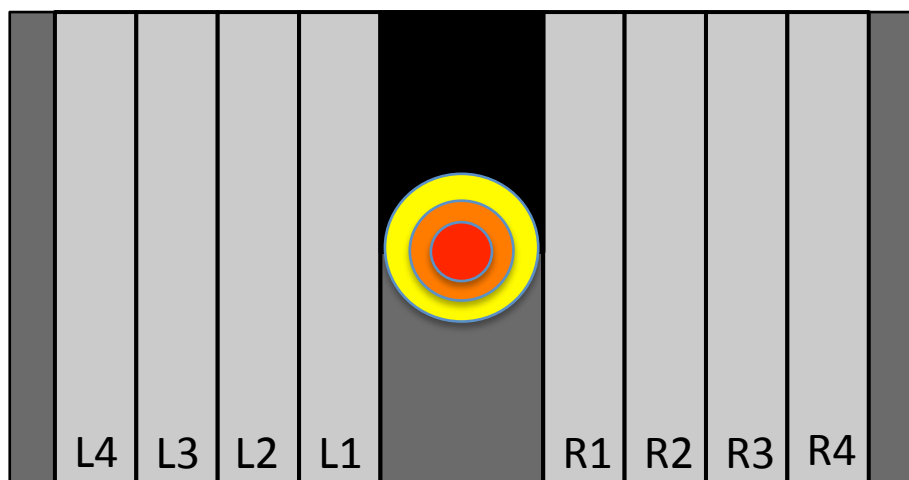


Fig. 24. Large panel cutting diagram. Resin is completely removed from black region above laser spot. Samples at the same distance from laser center are considered to be equivalent (i.e. L1 = R1, L2 = R2, etc.)

Results and Discussion

Irradiated strip samples (front and back) are shown in Fig. 26, in order (left to right) of increasing irradiance, from 100 – 525 W/cm². Surface ignition occurred after 2.5 s at 100 W/cm², decreasing to 0.1 s at 525 W/cm². As irradiance increased, volatile resin decomposition products were produced at greater rates and pressures, producing larger ignition plumes. Evidence of the extent of the surface flame can be seen by the soot deposits in Fig. 26 and Fig. 27, which grow to cover progressively more of the nearby un-irradiated surface. Fig. 28 shows thermal imagery of the flame jets. At lower irradiance (<205 W/cm²), the surface flame is confined to the front side of the sample only, but at higher irradiance, the flame is large enough to migrate to the backside where it is sustained by volatile products from the backside resin and depletes the



Fig. 25. MTS Testing Machine with sample.

backside surface resin as well. As irradiance increases, resin is completely removed from a larger area around the laser spot as heat conducts to the surrounding material.

Examples of the large irradiated panels at 85, 284, and 490 W/cm² are shown in Fig. 27.

Irradiance ranged from 85 – 490 W/cm² (2.4-cm spot diameter) for 120 s. In all cases, the resin was completely removed from the laser spot through the full thickness of the panel. At laser center, significant fiber damage began to occur at 150 W/cm². The region where fibers are visibly ablated appears darker with a radius that increases with irradiance, ranging from $r = 6.5$ to 11 mm. Effects of heat conduction away from the laser spot are more evident in the larger panels, appearing as concentric rings around laser center for each phase. Just outside the region of ablated fibers is a ring of lighter-

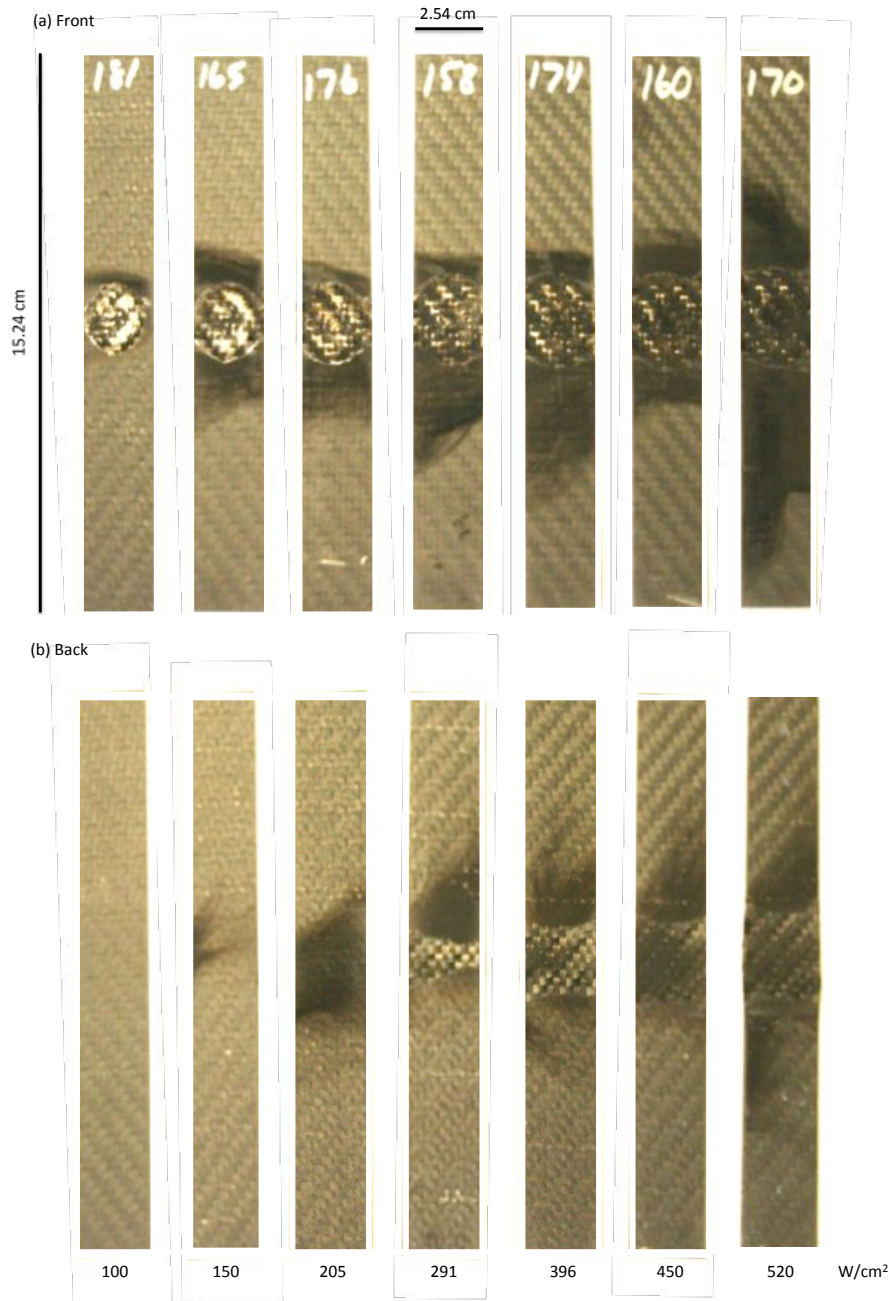


Fig. 26. Strips in order of (left to right) increasing irradiance (100, 150, 205, 291, 396, 450, and 520 W/cm²). (a) Front side (b) Back side

colored bare carbon fiber, then sooty bare fiber, then a ring of charred material, and finally a ring of discolored resin and the visibly undamaged panel. Ignition times ranged from 0.1 – 2.5 s for these panels as well, and the flames burned out the resin above the laser spot, requiring the first test sample to be cut outside this region.

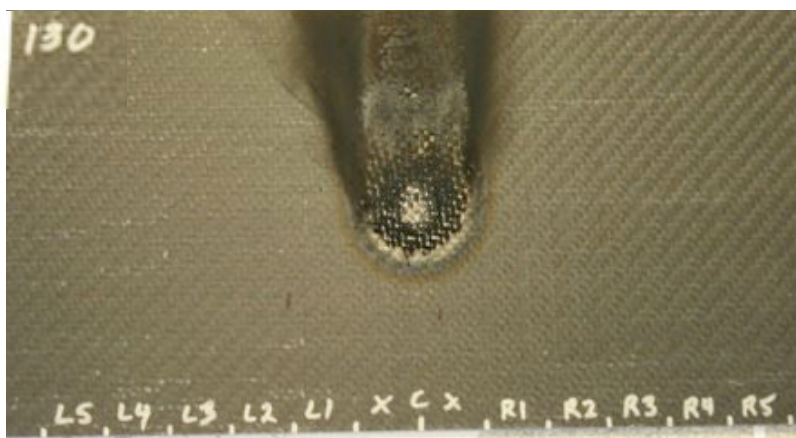
Surface Temperatures

Front surface temperatures at laser center for the pre-cut testing strips are shown in Fig. 29 with final temperatures ranging from 1535 °C to 2830 °C. Laser center temperatures for the large panels are shown in Fig. 30 with steady-state temperatures that range from 1027 °C to 1760 °C. Raw FLIR temperatures ($\epsilon = 1$) were corrected by SOC-100 emissivity measurements of the decomposition phases (virgin, char, bare fiber) up to 500 °C and extrapolated temperature dependent emissivity for bare fiber for higher temperatures as shown in Fig. 6 and Table 3.

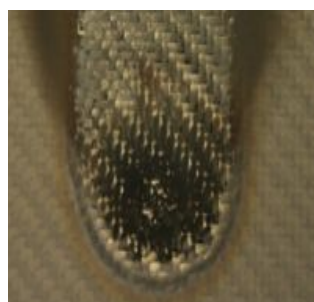
Mass Changes

Mass removed from the pre-cut strips as a function of total deposited energy and peak irradiance is shown in Fig. 31. The data indicates a mass removal threshold of 1.08 kJ and a rate of 0.15 g/kJ. The peak irradiance to energy deposited ratio is $0.078 \text{ s}^{-1}\text{cm}^{-2}$.

Front



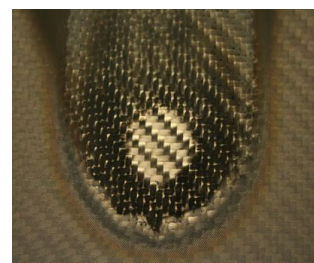
Back



(a) 85 W/cm²



(b) 284 W/cm²



(c) 490 W/cm²

Fig. 27. Large test panels at 85, 284, and 490 W/cm². Backside in inset. Markings are guidelines for cutting into testing strips (later widened strips, allowing only 4 to be cut).

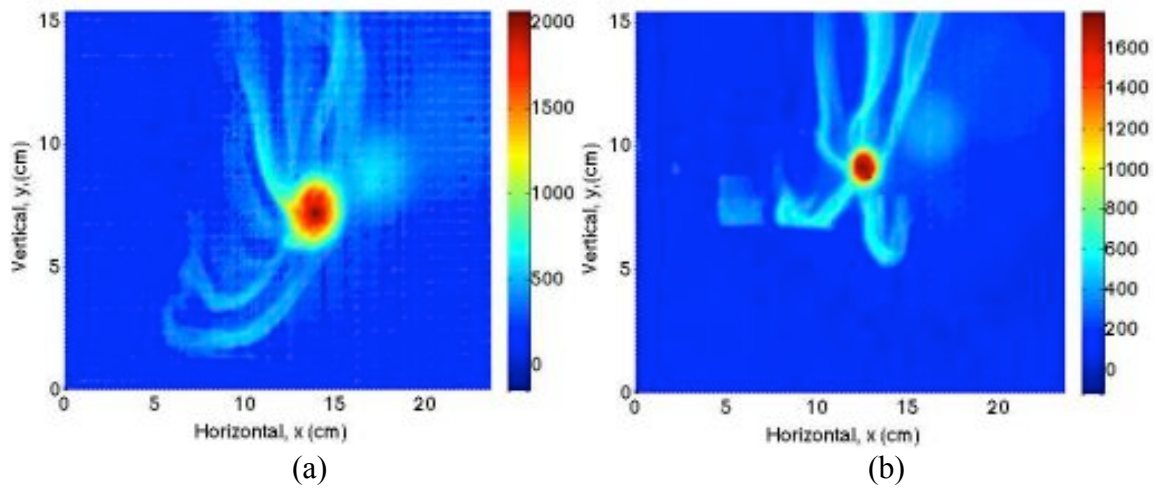


Fig. 28. Thermal image of flame jets (a) large panels at 490 W/cm^2 after 6 seconds and (b) pre-cut strip at 520 W/cm^2 after 1.6 seconds

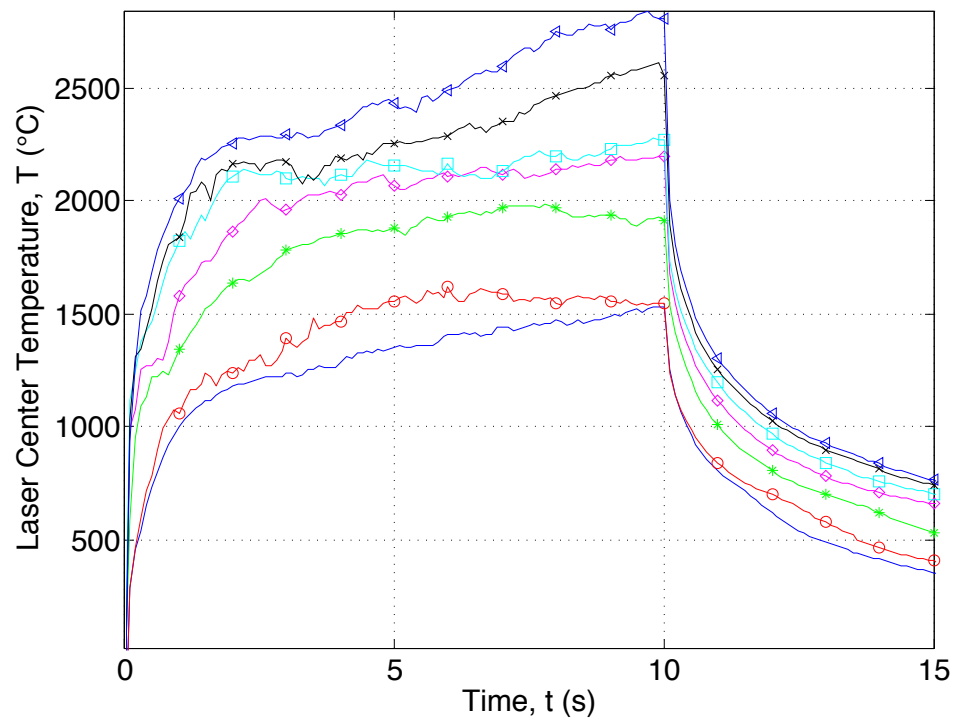


Fig. 29. Pre-cut strip laser center temperatures at 100 W/cm^2 (—), 152 W/cm^2 (○), 205 W/cm^2 (*), 296 W/cm^2 (◇), 396 W/cm^2 (□), 450 W/cm^2 (×), 520 W/cm^2 (△)

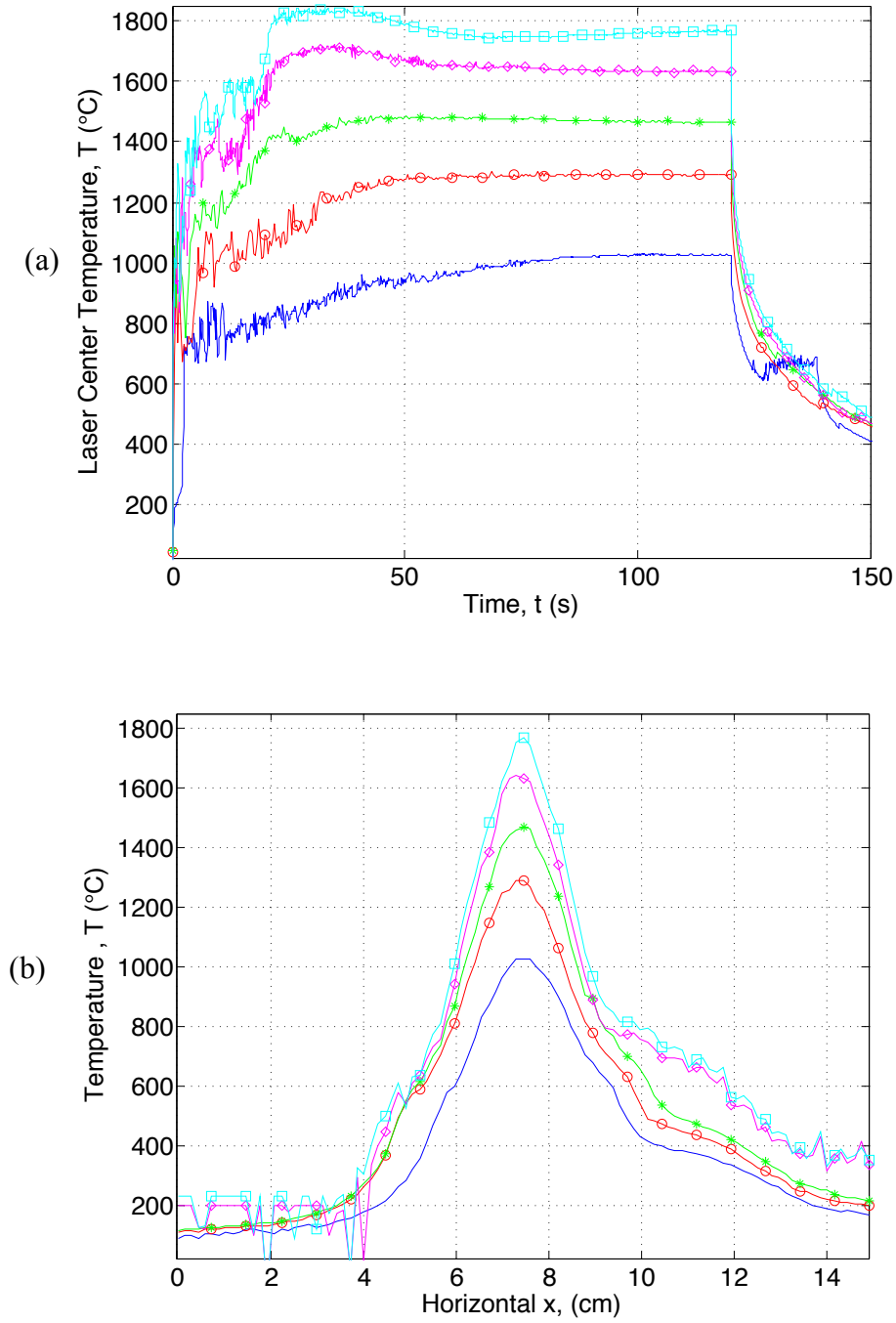


Fig. 30. Panel temperatures at 85 (—), 189 (○), 285 (*), 396 (◇), and 490 (□) W/cm² at (a) laser center and (b) horizontal profile through laser center. Steady state temperatures increase with irradiance.

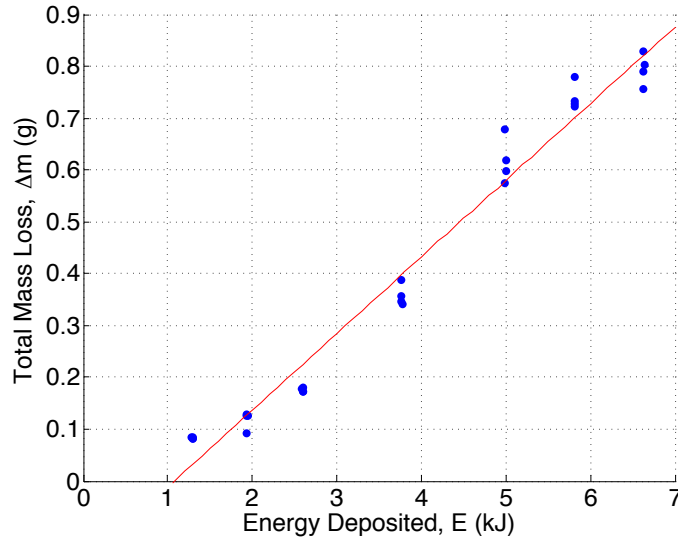


Fig. 31. Mass removed from thin strips as function of total energy deposited.

Strength Loss

Eleven undamaged specimens, cut from similar panels of the same batch and identical in size, shape, fiber orientation, tabbing and testing conditions, were tested to establish a baseline ultimate compression strength of 270.3 ± 6 MPa. Undamaged samples failed suddenly at random locations throughout the gauge section at an approximate 45° relative to the fiber direction, as shown in Fig. 32. On the pre-cut samples, limiting the gauge length to the laser spot and a minimum (approximately 1 cm) of surrounding material minimized the buckling nature of the failure. As the degradation of the samples increased, failure was less sudden, transitioning to a more gradual, crunching failure mode (Fig. 33).

A marked decrease in ultimate compressive strength was observed between samples that exhibited front-side combustion only and those that burned from the backside as well (Fig. 34). Mass loss is also well correlated with laser power.

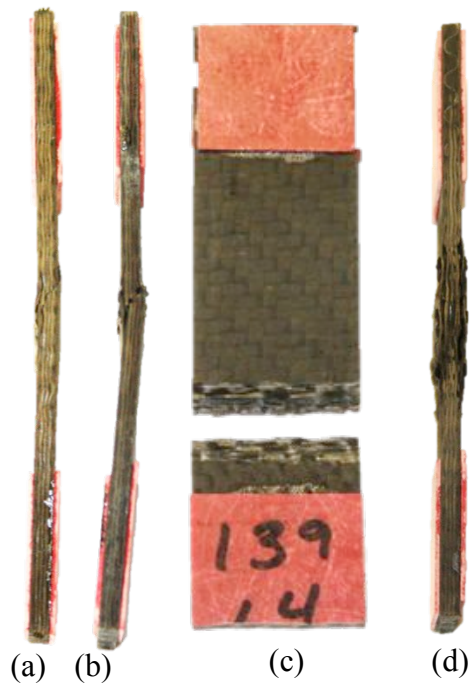


Fig. 32. Failure modes of CFRP. Undamaged material (a-c) failed dramatically in compression at 45° relative to applied stress. Test was terminated after sharp reduction (>90%) in sustained load. Heavily damaged material (d) failed gradually in brooming-type failure.

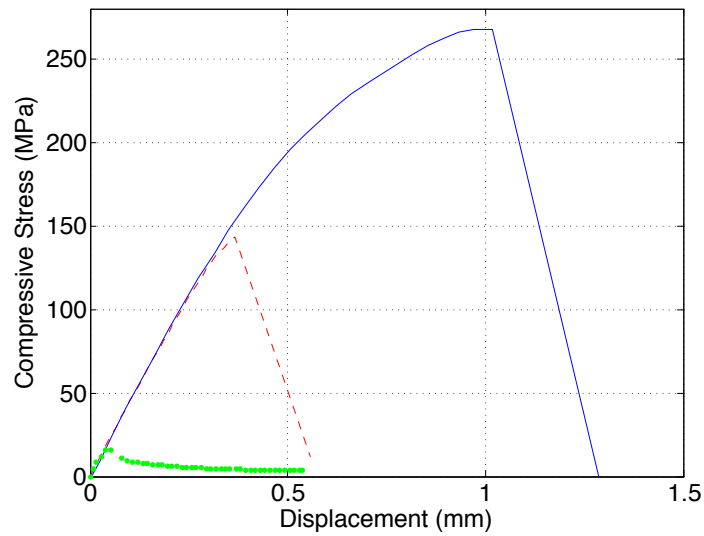


Fig. 33. Testing behavior of baseline (—), 130 W (---), and 500 W (•) strength testing samples.

As shown in Fig. 35, significant reductions in compressive strength were localized to approximately twice the laser spot radius. Within this region, the strength is assumed negligible as the CFRP was too damaged to machine into a test strip. The first 25 mm wide region immediately outside this region suffered typical strength degradation of 10-33%, reaching approximately 50% at 520 W/cm². All measured compressive strengths beyond this area were undiminished.

Model

The 3D thermal model as developed in Chapter III was used to predict the strength remaining in the laser irradiated pre-cut strip samples. The same evolving thermal properties and kinetic parameters were used as previously determined. The model mesh was resized to 45 x 9 elements to match the length and width of the strip, with 8 elements, one for each ply, in the thickness direction, parallel to the incoming

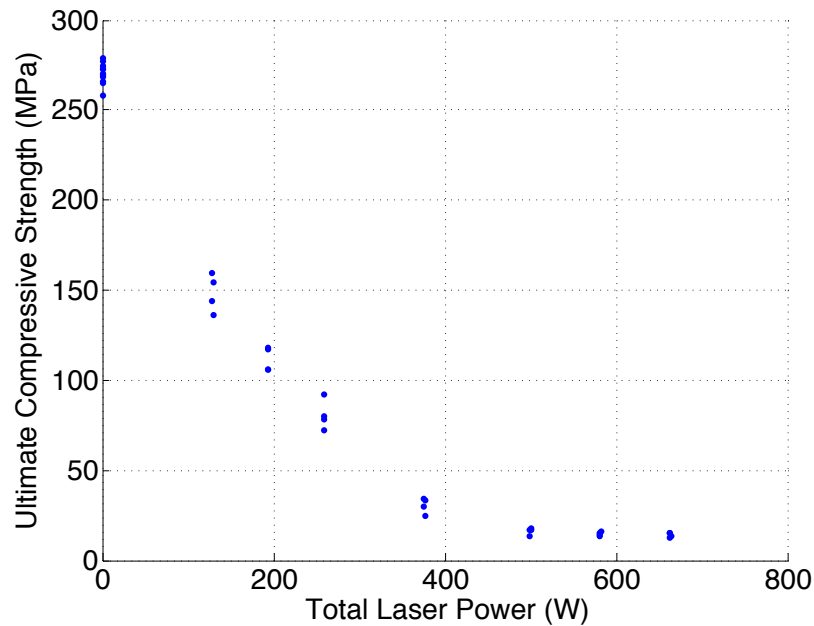


Fig. 34. Ultimate compressive strength decreased with increasing laser power.

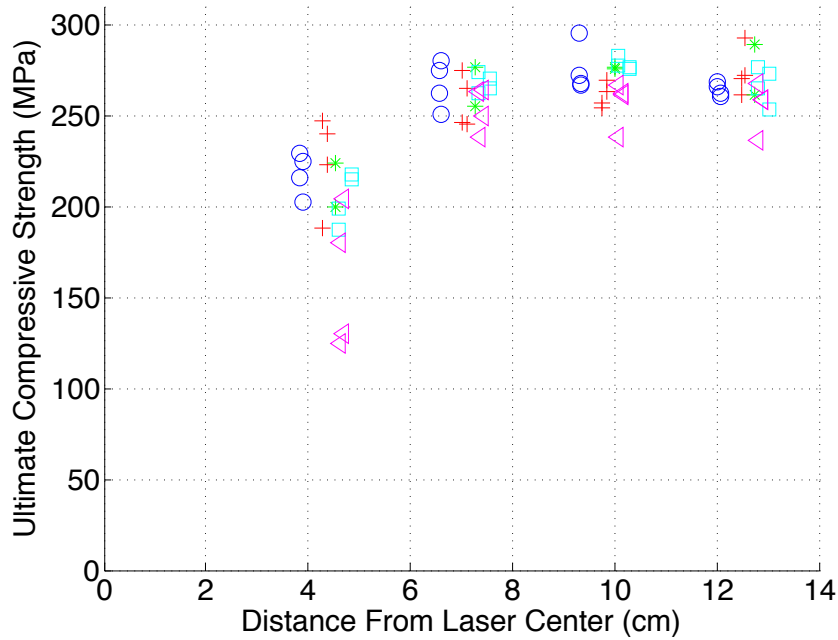


Fig. 35. Strength reduction away from laser center at 85 W/cm² (○), 189 W/cm² (+), 285 W/cm² (*), 396 W/cm² (□), and 490 W/cm² (△).

laser. The laser spot from the IR camera was calibrated to total laser power and introduced directly to the model, as before. The simulation was run for 30 s to allow for CFRP degradation due to both the 10 s laser shot and heat conduction into the surrounding material during cool-down. The model includes a multi-step decomposition reaction, transitioning from virgin resin to dehydrated resin (with minimal mass loss) to char (with significant volatile production) to bare fiber (with char oxidation). At the end of the simulation, the proportion of remaining virgin resin, dehydrated resin, char, and bare fiber throughout the sample were recorded.

One modification was made to the existing model to account for surface heating due to volatile combustion. An additional boundary condition term was added to Eq. 2 (Chapter III) of the following form:

$$\frac{m_v HRR_{max}}{m_{v,max}} \quad (29)$$

where m_v is the instantaneous volatile mass release rate with units of kg/s cm². This is calculated as the sum of all the volatiles produced during the current time step at each position on the incident face through the whole sample thickness divided by the time step and the element surface area. HRR_{max} is the maximum heat release rate for an epoxy matrix. Heat release rate (HRR) is a commonly measured quantity in the fire science community and it describes the heat flux imparted to a surface when decomposition products from that surface ignite and burn in close proximity. HRR increases with incident heat flux in response to an increased rate of volatile fuel production up to a threshold. At higher fluxes, volatiles are generated very quickly, and at higher pressure, (see flame jets in Fig. 28) and this increases the size of the plume but not necessarily the intensity of energy feedback into the surface. Mouritz reports that the peak HRR for an epoxy matrix reaches a limiting threshold of approximately 24 W/cm² [10] by 10 W/cm² incident flux. The maximum instantaneous volatile mass release rate ($m_{v,max}$) at 10 W/cm² is calculated using the model described in Chapter III to be approximately 6×10^{-6} kg/s cm². At the high irradiance levels used here, volatiles are produced at even higher rates, but due to the threshold effect present in HRR, these high values are adjusted to a maximum of HRR_{max} (24 W/cm²). For m_v rates below that required to sustain HRR_{max} , HRR is proportional to the current m_v rate. It should also be noted that this effect is only present when the surface has ignited. The surface temperature at ignition was found to be 1470 ± 30 K for the strip samples. When surface temperatures reach this threshold, ignition is assumed to occur and the HRR flux contribution is added to the model. For

cases where only front side combustion is observed, the full HRR is added to the incident face of the modeled sample. In cases of both front and backside combustion, the volatiles (and resulting HRR) are assumed to be split evenly between front and backsides.

Combustion continues until the m_v rate drops below $7.5 \times 10^{-7} \text{ kg/s cm}^2$, the mass loss rate reported by Gibson to be the minimum value able to support piloted ignition [11, 97].

For these samples, compressive strength is limited by the composition of the sample cross section perpendicular to the compressive force with the least amount of matrix material remaining – at laser center. The final predicted percentages of virgin resin, dehydrated resin, char, and bare fiber remaining at the end of the test through the cross section at laser center is shown in Fig. 36 as a function of laser intensity. Surface maps of each component remaining through the laser center cross-section for the 100 W/cm² and 525 W/cm² cases are shown in Fig. 37. A linear system of equations having

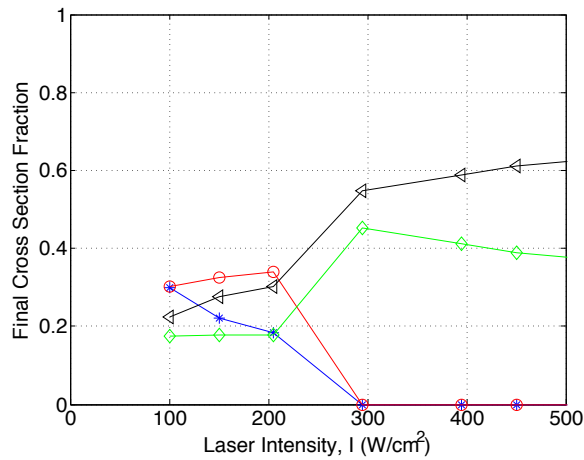


Fig. 36. Relative amounts of decomposition phases at end of simulation: virgin resin (*), dehydrated resin (o), char (◆), and bare fiber (Δ).

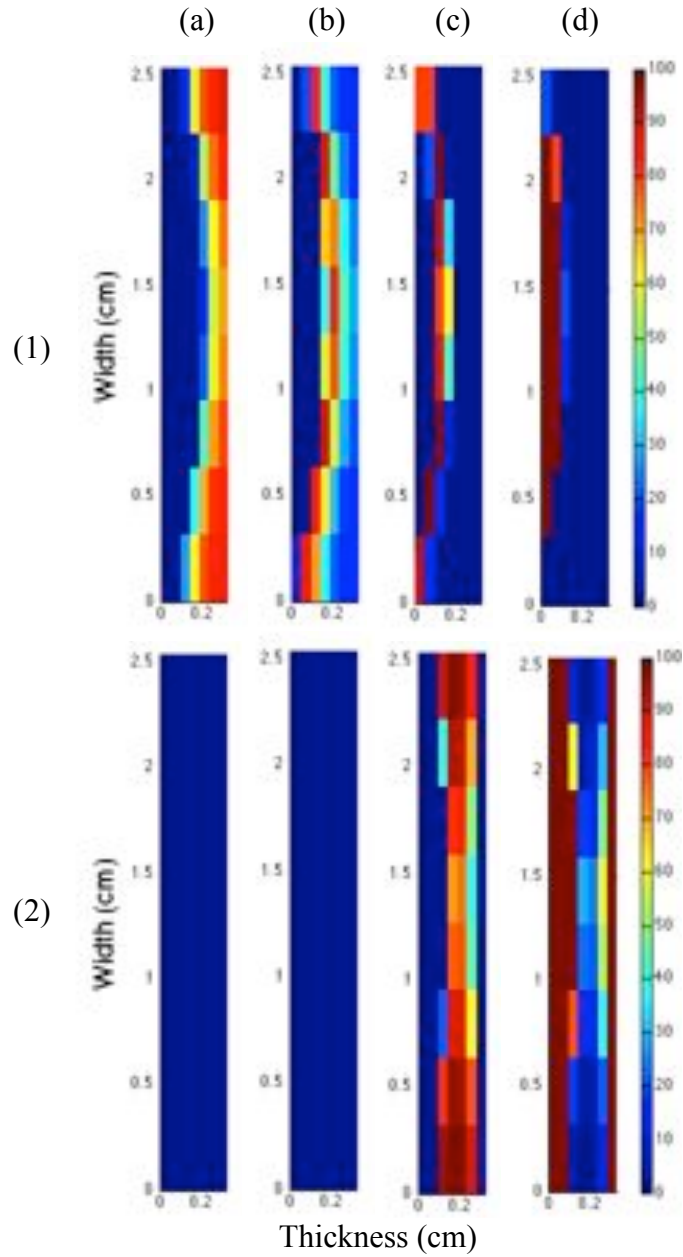


Fig. 37. Proportions of resin, dehydrated resin, char, and bare fiber (columns a–d) remaining after 10 seconds irradiation at 100 W/cm^2 (row 1) and 525 W/cm^2 (row 2). At lower irradiance, a reaction front mirroring the laser spot is visible midway through the sample thickness. At high irradiance, all the virgin resin and dehydrated resin has decomposed, with a core of char and bare fiber on both faces.

the form,

$$\sigma_c = \sigma_{res}f_{res} + \sigma_{dry}f_{dry} + \sigma_{char}f_{char} + \sigma_{fib}f_{fib}, \quad (30)$$

was used to estimate the strength of each decomposition phase, with σ_c , σ_{res} , σ_{dry} , σ_{char} , and σ_{fib} being the measured ultimate compressive strength of each irradiated sample and undamaged samples, and the unknown strengths of the dehydrated, charred and bare fiber decomposition phases, respectively. Here, it was assumed that virgin resin had compressive strength as measured and bare fiber had zero compressive strength, leaving only σ_{dry} and σ_{char} as unknowns. Solution of the system of equations yielded estimates for σ_{dry} and σ_{char} of 128 MPa and 48 MPa, respectively.

Conclusions

Residual compressive strength of laser-irradiated CFRP is tested in two configurations: (1) compressive strength as a function of irradiance level and distance away from laser center during a 120-s laser exposure and (2) compressive strength as a function of irradiance level at the laser spot for a 10-s laser exposure.

In the first configuration, 30 cm x 15 cm panels were irradiated with a central 2.4-cm diameter laser spot at irradiances ranging from 84-492 W/cm². Test samples (2.5-cm wide) were cut as close as possible to the damaged area (inner edge 2.4-3.3 cm from laser center) and found to have a compressive strength reduction of 10-50%. No reductions in strength were observed beyond this region. In a laser lethality scenario, all damage is expected to be localized within a radius that is 2-4X the laser spot radius, with smaller damage zones for shorter duration exposures.

In the second configuration, 15 cm x 2.5 cm CFRP strips were irradiated with a central 1.65-cm diameter laser spot at irradiances ranging from 100-525 W/cm² for a 10-s exposure. Samples ignited in 0.1-2.5 s with flames spreading to the backside of the sample for higher irradiance tests. Residual compressive strengths of 27-59% remained when combustion was limited to the front side only, decreasing to 5-10% for both front and backside flames.

A previously developed thermal model incorporating matrix decomposition reactions and resulting changes to thermal and optical properties was used to model the laser irradiation and predict the resulting compressive strength of the irradiated strips. The additional heat flux from surface combustion was found to be a necessary component to accurately predict CFRP decomposition, particularly when backside combustion is present. The modified model was used to predict final distributions of virgin resin, dehydrated resin, char, and bare fiber and estimate the compressive strengths of intermediate states dehydrated resin and char to be 128 MPa and 48 MPa, respectively.

VI. Carbon Fiber Composite Laser-Induced Surface Ignition

Hyper-spectral imaging of laser-heated CFRP decomposition plumes at irradiances of 5-40 W/cm² was conducted under buoyant conditions. Thermal imagery at 30-240 Hz and spatial resolution of 1.49 mm/pixel was used to determine time until ignition and surface temperatures at ignition for these and additional tests at irradiances of 5-525 W/cm². Relative concentrations of volatile decomposition products were observed to reach steady state for > 30 s (at 37 W/cm²) before ignition occurred. In cases of piloted ignition, surface ignition occurs at irradiances < 5 W/cm². In HEL scenarios, ignition is dependent on reaching surface temperatures of 1451 ± 48 K and irradiances > 19 W/cm². Hyper-spectral imagery was collected and processed by Captain Ashley Gonzales.

Introduction

Ignition time is a key property of materials that characterizes the rate of fire spread and is of great interest in the field of fire science. When a polymer matrix composite is radiantly heated to its decomposition temperature, volatile decomposition products are produced at the surface. For an epoxy-based composite, this requires an incident heat flux of at least 1.3 W/cm². If the flux and decomposition rate is high enough (approximately 0.0075 kg/m²s [95]) ignition will occur and the surface will burn, fed by additional decomposition products until the material is exhausted. Decomposition rates increase at higher heat fluxes and ignition times decrease rapidly. Because of their low thermal conductivities, ignition times are largely independent of material thickness for radiant fluxes above 10 W/cm² [10].

In a fire scenario, the source of heat to decompose the matrix is a nearby fire, and practically all existing data is for piloted ignition. This is not the case for the initial stages of an HEL scenario, which provides many times the necessary surface heating to produce volatile products but provides no ignition source, producing much different ignition criteria.

As volatile decomposition vapors accumulate in the vicinity of the laser spot, they can be detected and their relative concentrations tracked during the period leading up to ignition using an imaging Fourier Transform Spectrometer (IFTS). IFTS uses a Michelson interferometer and a detector array to generate interference spectra at every pixel in a scene. IFTS has been previously used to analyze the constituents of industrial smokestacks [50], jet engine exhaust plumes [51], chemical plumes [52], natural gas flare emissions [53], and HEL material degradation plumes (fiberglass [4], polymethyl methacrylate (PMMA) [54], and graphite [55]).

Experimental

CFRP panels of 3.2-mm thickness in varying sizes were irradiated by a 2-kW cw IPG Photonics fiber laser at 1.07 μm . Low irradiance (5-64 W/cm^2) experiments were conducted on 10.38 cm x 10.38 cm panels with a 6-cm diameter laser spot for 120 s. High irradiance (85-525 W/cm^2) experiments were conducted on 30.48 cm x 15.24 cm panels with a 2.4-cm diameter laser spot and 15.24 cm x 2.54 cm panels with a 1.65-cm diameter laser spot.

Surface temperature maps were measured using a FLIR SC6000 MWIR camera at four integration times at frame rates of 30-240 fps. This imagery was corrected for non-

linearity and non-uniformity, calibrated with a wide-area blackbody, and corrected with measured emissivities of CFRP as a function of decomposition phase and temperature (up to 773 °C with extrapolation to higher temperatures). More details on these experiments and techniques can be found in Chapters 2 and 4.

Absorption spectra of the decomposition plume were measured from the side (Fig. 38) using a Telops Hyper-Cam MWIR IFTS for irradiances $< 64 \text{ W/cm}^2$. After ignition, the sooty plume burned with a much brighter flame and saturated the IFTS detector. Different instrument settings are required to image the plume before and after ignition, and would have required duplicate experiments, which were not repeated due to the focus on characterizing the plume prior to ignition. The Telops IFTS was windowed down to 128×64 pixels (from a max of 320×256) and the spectral resolution was reduced to 16 cm^{-1} (from a max of 0.25 cm^{-1}) at integration times of 40-50 μs . This was done to increase the frame rate to 9-14 fps (from typical values of 1-2 fps) to enable observations in the case of rapidly changing plume dynamics.

Results and Discussion

The time when the laser was turned on was determined with an accuracy of 0.03 s using footage from a visible witness camera at 30 Hz. Timestamps on frames from the witness camera and the FLIR MWIR camera were synchronized using a timing signal from the FLIR IRIG system. Ignition times relative to the time the laser was turned on were determined from both the visible camera and confirmed from a temperature spike present in the FLIR data at ignition. Most FLIR data was taken at $> 120 \text{ Hz}$, producing an overall accuracy in ignition times of approximately 0.04 s.

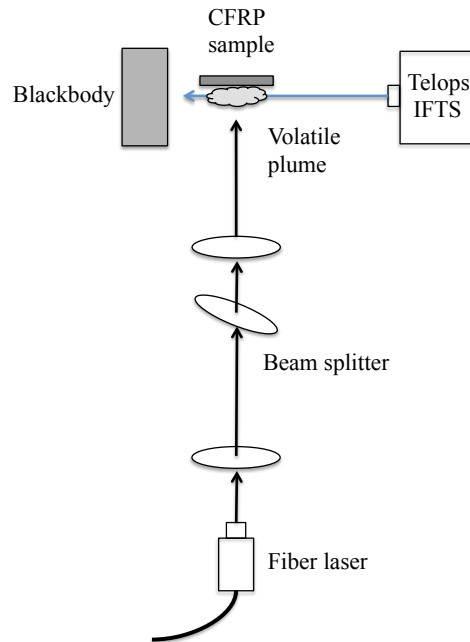
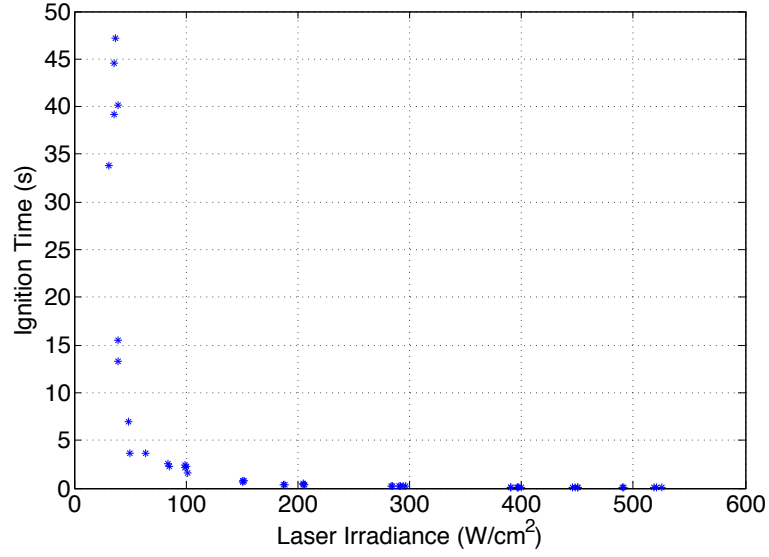


Fig. 38. Telops IFTS imaging configuration. IFTS measurements were taken concurrently with FLIR surface temperature measurements (see schematic in Fig. 2), but for clarity those elements have been omitted here.

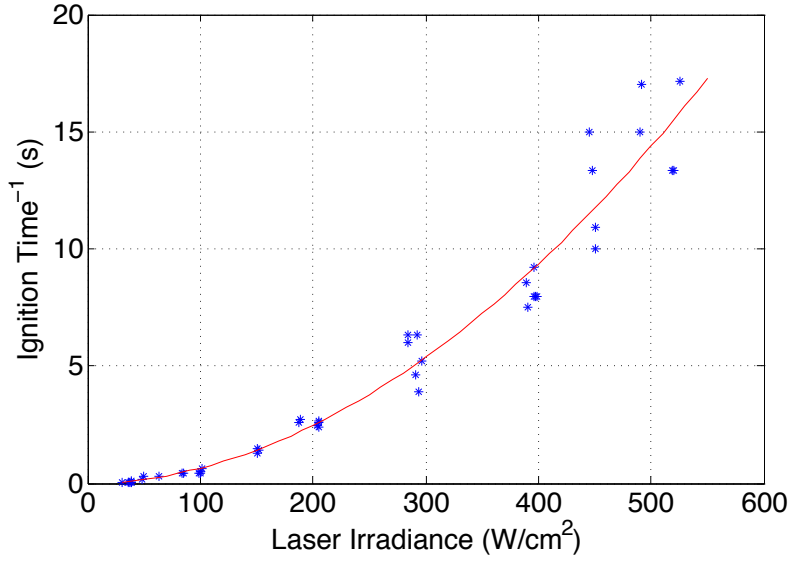
At irradiances $> 500 \text{ W/cm}^2$, ignition times are determined rather imprecisely as $0.07 \pm 0.04 \text{ s}$. Ignition was observed for all irradiances $> 21 \text{ W/cm}^2$ with the ignition times as shown in Fig. 39. The threshold for ignition occurs near 21 W/cm^2 with some tests igniting and others not. When ignition occurs, it is after $> 100 \text{ s}$. At 35 W/cm^2 , ignition occurs in 40-50 s. As irradiance increases, ignition times decrease rapidly, decreasing to 2.1 s by 100 W/cm^2 and 0.07 s at 525 W/cm^2 , near the measurement limit in this work. Ignition times show a small dependence on sample thickness, decreasing from an average of 43.6 s to 28.4 s to 24.1 s as thickness decreases from 3.2 mm to 2.4 mm to 1.7 mm, at $35 \pm 2 \text{ W/cm}^2$. This is likely due to a decreasing amount of matrix available to decompose, which has a cooling effect and delays surface heating to the ignition

temperature. Fig. 39(b) shows a slight upward curvature, indicating that ignition times (t_{ign}) have an exponential inverse dependence on surface intensity (L) of the form

$$t_{\text{ign}} = 1.083 \times 10^4 L^{-1.924}.$$



(a)

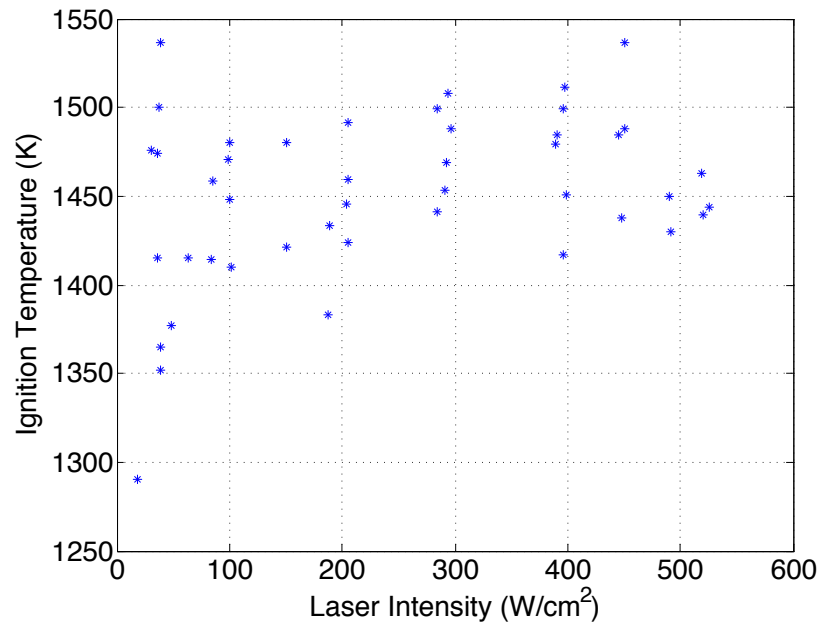


(b)

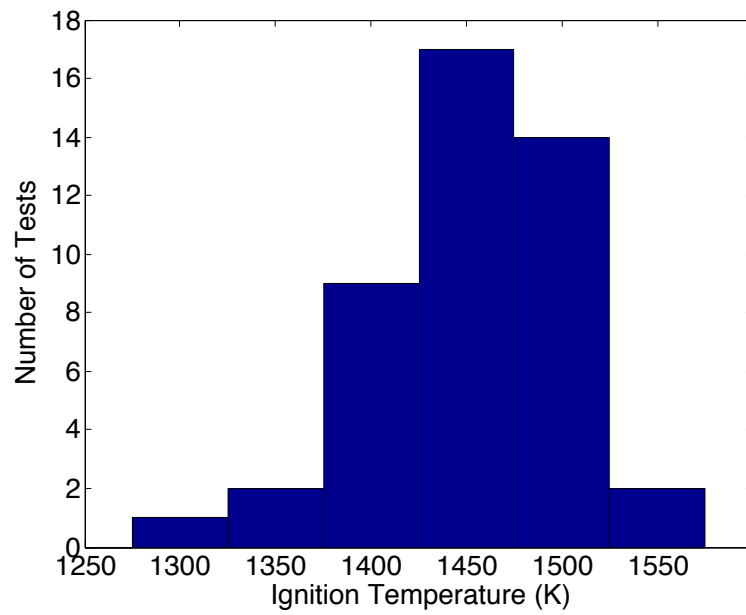
Fig. 39. Ignition times (a) and ignition time inverse (b) as a function of incident laser irradiance

Ignition temperatures were determined from the FLIR imagery at laser center in the frame immediately before ignition. This was done to avoid the thermal emission from the ignition flash (creating the spike in temperature indicative of ignition). Raw temperatures (assuming $\epsilon = 1$) were corrected using the same measured emissivities detailed in Chapter III. Final ignition temperatures at different laser intensities are shown in Fig. 40. Surface temperature at ignition does not appear to be dependent on laser intensity or surface heating rate. Temperatures are approximately normally distributed (Fig. 40(b)) around 1451 K with a standard deviation of 48 K for all laser intensities, sample sizes, and laser spot diameters tested.

An example of the Telops IFTS data is shown in Fig. 41. Fig. 41(a) shows a broadband image from its side-view position. The turbulent smoky plume can be clearly seen as can the high intensity region where the laser is incident, the cool edge of the sample in profile and backside heating. The spectrum at each pixel at laser height, traversing the plume from far in front to behind the panel (each labeled with an x), is shown in Fig. 41(b). All pixels show the rising blackbody baseline at lower wavenumbers. Several pixels passing directly through the most intense region in the broadband image display a broad peak from 2677-3201 cm^{-1} and a sharp peak from 3600-3700 cm^{-1} . An additional peak that appears to be correlated with these peaks appears from 1959-2337 cm^{-1} .



(a)



(b)

Fig. 40. Ignition temperatures as a function of laser intensity.

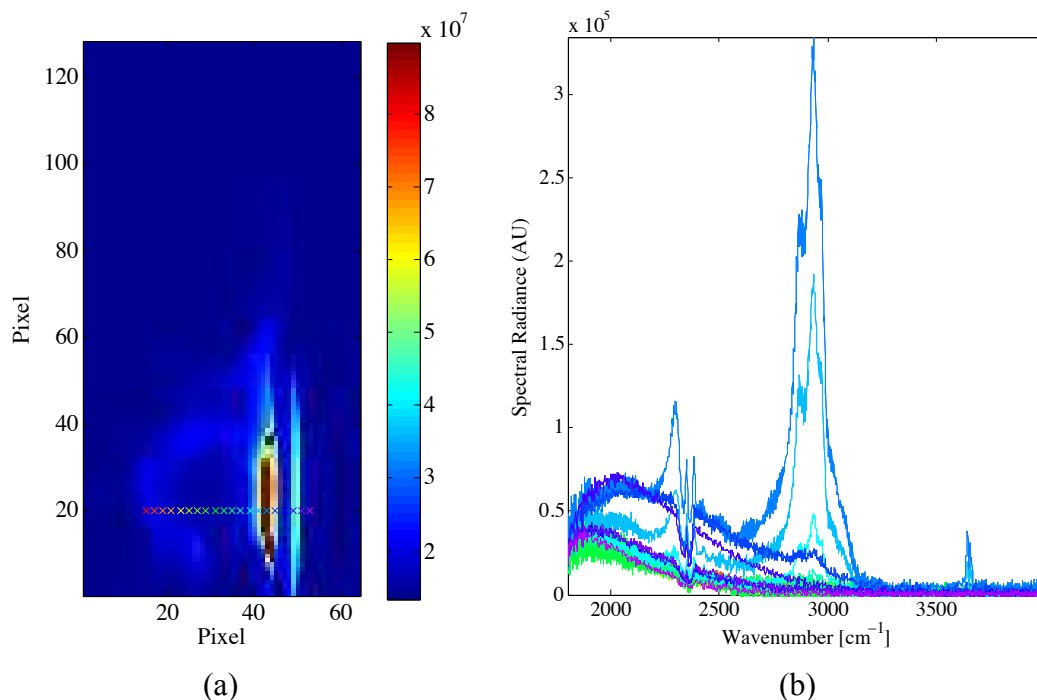


Fig. 41. The Telops MWIR IFTS imaged through the surface decomposition plume with the sample in profile (5 W/cm^2 laser coming from the left) as shown in the broadband image in part (a), with the highest intensity in front of the laser spot. Part (b) shows the FTIR spectrum at each pixel in a row at laser center, starting far in front of the sample and ending on the backside, with the highest intensity peaks from $1959\text{--}2337 \text{ cm}^{-1}$, $2677\text{--}3201 \text{ cm}^{-1}$, and $3600\text{--}3700 \text{ cm}^{-1}$ for several pixels near the surface.

Many of the decomposition products resulting from decomposition of the epoxy matrix in CFRP have been identified [22] and have characteristic absorption peaks centered near 3000 cm^{-1} due to C-H bond stretching and at 3700 cm^{-1} due to phenolic O-H bond stretching. However, their production ratios are less well known and their absorption cross-sections are unavailable. This limits the tracking of decomposition products in the plume to relative concentrations estimated from the changing peak areas only.

Peak areas are calculated as illustrated in Fig. 42. After smoothing using a moving average filter with a span of 5 points, the data in four spectral regions lacking

strong features (shown in blue) is fit to a second-order polynomial and used to remove the blackbody baseline to isolate the peak areas only Fig. 42(b). Then, the peak areas in the three spectral regions of interest ($1959\text{--}2337\text{ cm}^{-1}$, $2677\text{--}3201\text{ cm}^{-1}$, and $3600\text{--}3700\text{ cm}^{-1}$) are numerically integrated. This procedure is repeated for every pixel in each frame to produce images of changing volatile peak areas as a function of spatial location and time throughout each test.

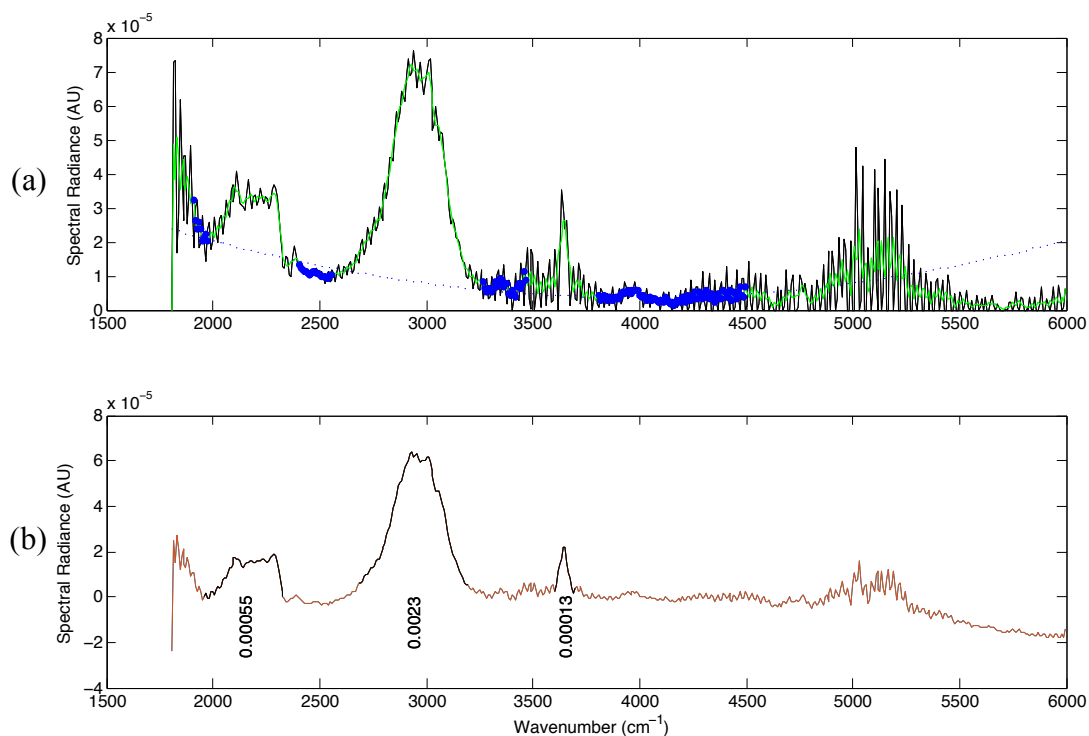


Fig. 42. Illustration of peak area calculation. Calibrated spectra (—) in (a) are first smoothed (—) and the baseline (—) is fit to a polynomial before being removed. Peak areas (b) are then numerically integrated. The feature near 5000 cm^{-1} is an artifact of calibration, which is poor above 4000 cm^{-1} .

The pixel with maximum peak area for each spectral band in each frame, near laser center as shown in Fig. 41(a), is plotted in Fig. 43. The relative concentrations quickly rise from zero at laser on and establish a steady concentration after a few

seconds. The three peak areas are linearly correlated with one another, suggesting a single-step volatile-producing decomposition reaction. This concentration is relatively unchanged for the remainder of the shot, up until ignition occurs. At this point, the plume becomes optically thick and the Telops IFTS detector saturates from the intensity of the sooty combustion flame. This is not consistent with a required minimum concentration of volatile products near the surface for ignition to occur. Instead, sufficient volatiles are present and waiting for the surface temperatures to reach the

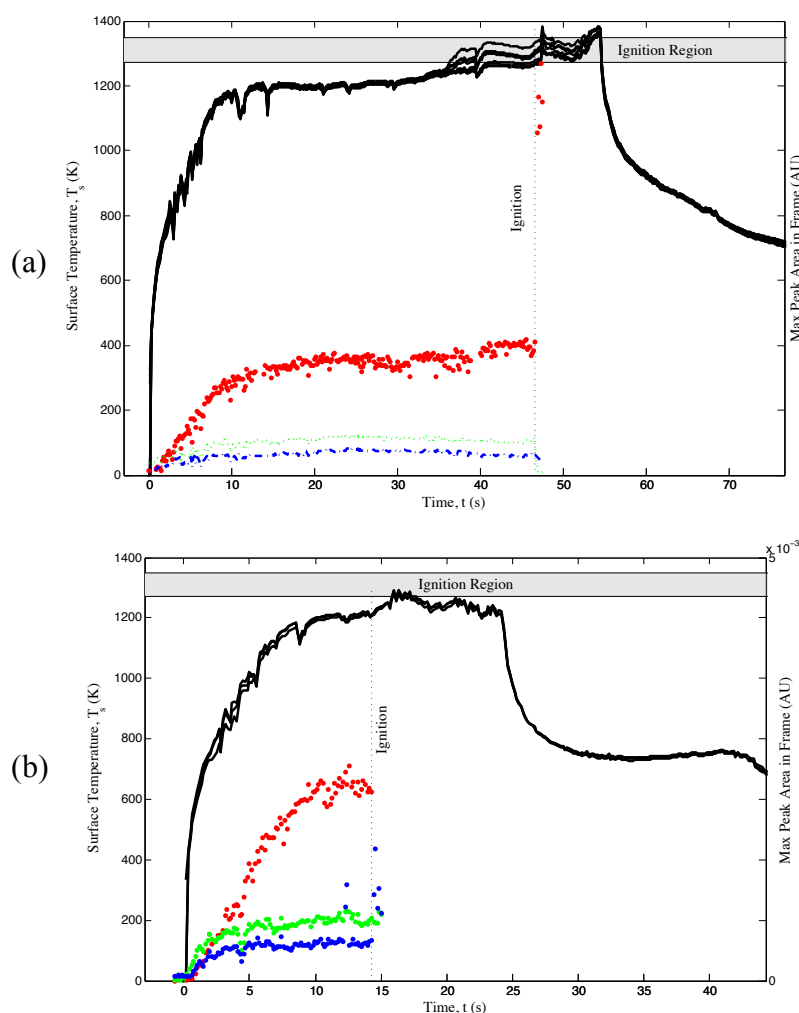


Fig. 43. Maximum volatile peak areas and surface temperatures (T_s) at (a) 37 W/cm² and (b) 39 W/cm². Peak areas from 2677-3201 cm⁻¹ are greatest (•), followed by peak areas from 1959-2337 cm⁻¹ (•), and peak areas from 3600-3700 cm⁻¹ (•).

critical surface temperature (1451 ± 48 K) to cause ignition. One exception to this occurs in cases where front side ignition occurs quickly and flames reach beyond the top of the sample. In this case backside volatiles are present in suitable quantities to be externally ignited at much lower surface temperatures (approximately 700 °C).

Conclusions

Under buoyant conditions, epoxy decomposition of CFRP under high energy laser irradiation at 1.07 μm produces sufficient volatile decomposition products to support combustion at very low irradiances (<5 W/cm²), but must have an ignition source or laser heated surface temperatures of 1451 ± 48 K for ignition to occur. Radiometric temperature measurements are made within 0.004 - 0.033 seconds of ignition and relative volatile concentrations at the surface during the time period leading up to ignition are measured using imaging Fourier Transform Spectroscopy and reach steady state concentrations in approximately 3 seconds. This finding is valid for laser spot sizes ranging from 1.65-6 cm diameter and laser powers from 5-525 W/cm².

VII. Conclusions

Thermal imaging of laser irradiated carbon fiber reinforced polymer (CFRP) and graphite at high spatial and temporal resolution along with thermal modeling was developed as a tool for investigating laser-material interactions, including decomposition kinetics and the phase and temperature dependence of thermal and optical material properties. Measured surface temperatures were corrected using measured spectral emissivities of material decomposition phases with limited temperature dependence. A heat transfer model based on Fourier's heat transfer equation along with appropriate boundary conditions and decomposition reactions was used to model surface temperatures. Model results for laser irradiation of CFRP developed at low irradiance (5 W/cm^2) were used to predict laser effects at irradiances as high as 525 W/cm^2 with the addition of modeled surface heating due to surface combustion. Compressive strength remaining in CFRP material after a 10 second laser irradiation was measured and correlated to model results to estimate the residual strength of CFRP decomposition phases. The dependence of ignition of volatile decomposition products on plume concentration and surface temperatures was investigated using imaging Fourier Transform Spectroscopy (IFTS). Graphite was modeled to estimate temperature dependent thermal properties and reaction kinetics for binder removal and graphite sublimation.

Key Results

This research has demonstrated the ability to develop thermal models of laser-material interactions from changing surface temperature maps on both carbon fiber-

reinforced polymers (CFRP) and porous graphite. Models derived from efforts modeling composite response to surface fire proved to be adequate. Surface temperatures were measured with a dynamic range > 3000 K at frame rates up to 240 Hz and corrected using measured pre- and post-irradiation emissivity values. Residual strength of CFRP was measured as a function of irradiance and distance from the laser spot and modeled using the developed model. Ignition conditions under laser irradiation were determined.

Carbon Fiber Composite

Surface temperature maps of the incident and backside faces of a CFRP composite material irradiated with a high power laser at $1.07\text{ }\mu\text{m}$ and $5\text{--}64\text{ W/cm}^2$ were recorded with a MWIR thermal camera during a 120 second exposure. Raw temperature maps were corrected using measured spectral emissivity of several phases of matrix decomposition. Measured temperature distributions were modeled with a 3D numerical heat diffusion model to estimate resin decomposition kinetic parameters, the enthalpies of decomposition, and the thermal properties of decomposition reaction stages. Several heat transfer mechanisms were considered, including emission, convection, heats of decomposition and the heat capacity of departing volatile decomposition products. The model was constrained by evolving spatial temperature distributions over both front and back faces for various irradiances and sample thicknesses as well as available literature values. No additional heating rate dependence of the decomposition kinetics were observed at the very high heating rates ($12\text{--}330\text{ }^{\circ}\text{C/s}$) studied here.

Graphite

Temperature maps of the incident face of porous graphite samples irradiated with a high power laser at $1.07\text{ }\mu\text{m}$ at irradiances of $0.78\text{--}3\text{ kW/cm}^2$ were recorded at 87.5 Hz

and 0.33 mm/pixel resolution with a MWIR thermal camera. Raw temperatures were corrected using measured spectral emissivity of irradiated and un-irradiated graphite from 2-25 μm . Emissivity decreased with wavelength for each sample, increased at all wavelengths after irradiation ($\Delta\epsilon = +0.05\text{-}0.09$), and is lower for less porous grades of graphite. Consideration of the evolution of surface emissivity is critical to the accuracy of surface temperature maps, with a temperature uncertainty of approximately 20 K for each 0.01 difference ($\Delta\epsilon$) from a true value of $\epsilon = 0.9$ at 3000 K.

Initial heating rates at laser center of 400 – 1800 K/s and steady state temperatures of 2500 – 3500 K are achieved. As much as 43 % of the laser power is re-radiated for surface temperature of 3350 K. Heating rates temporarily decline when heating through 2200 – 2900 K, due to binder removal. Maximum steady state temperatures of approximately 3600 K are reached, approaching the sublimation temperature. The radial distribution of temperatures is dramatic, with surface temperature declining by as much as 2000 K or 60 %, at distances of two laser spots sizes, despite thermal diffusivity greater than typical metals. Edge temperatures can be as high as 1500 K.

Temporal and spatial temperature changes throughout the 120-second test were modeled to estimate temperature dependent conductivity and kinetic parameters of graphite binder removal and graphite sublimation. First order Arrhenius pre-exponential factors and activation energies were found to be $4 \times 10^6 \text{ s}^{-1}$ and $3.5 \times 10^5 \text{ J/mol}$ for binder removal and $3 \times 10^9 \text{ s}^{-1}$ and $7.1 \times 10^5 \text{ J/mol}$ for graphite sublimation, respectively. The effect of plume absorption of sublimation graphite is also estimated.

Carbon Fiber Composite Strength Reduction

Residual ultimate compressive strength of laser irradiated CFRP is tested (1) as a function of irradiance level and distance away from a 120 second laser exposure and (2) as a function of irradiance level at the laser spot for a 10 second laser exposure. In the first configuration, irradiances ranging from 84-492 W/cm² were found to have a compressive strength reduction of 10-50% in the visibly undamaged region immediately adjacent to the laser spot. All damage is localized within a radius that is 2-4X the laser spot radius, with smaller damage zones for shorter duration exposures. In the second configuration, pre-cut testing strips irradiated at 100-525 W/cm² were found to have residual compressive strengths of 27-59% remaining when combustion was limited to the front side only, decreasing to 5-10% for both front and backside flames.

The thermal model previously developed was modified to incorporate heating due to surface flames and used to predict the resulting distribution of decomposition phases in the final testing cross section. A system of equations was used to estimate the ultimate compressive strengths of the dehydrated resin decomposition phase and char to be 128 MPa and 48 MPa, respectively.

Carbon Fiber Composite Ignition Conditions

Ignition of volatile products from the thermal decomposition of the epoxy matrix of carbon fiber reinforced polymers (CFRP) as a result of high energy laser (HEL) irradiation at 1.07 μm is dependent on reaching surface temperatures of 1451 ± 48 K. Imaging Fourier transform spectroscopy (IFTS) is used to measure and track relative concentrations of volatile decomposition products within the surface plume. These

concentrations reach steady state conditions within approximately 3 seconds and do not ignite until the ignition surface temperature is reached.

Recommendations for Future Work

Accurate radiometric temperature measurement depends heavily on accurate emissivity values and the increased use of thermal imaging for the investigation of laser-material interactions will require the best emissivity values available. Hemispherical directional reflectometers (HDRs) at present provide emissivity measurements at moderate temperatures. These studies can be buoyed by thermal imagery of known surface temperatures and the development of simultaneous emissivity and temperature extraction techniques using IFTS measurements of the material surface.

The modeling approach demonstrated here can be adapted and enhanced to incorporate additional experimental factors present in real laser engagement scenarios including tangential flow conditions, surface coatings, and sandwich stack-ups. Model extensions including carbon fiber oxidation and sublimation also become more necessary as laser powers and exposure time increase.

A major difficulty encountered in this work was the simultaneous determination of multiple, interrelated material property and heat transfer process parameters. This process is greatly aided by careful experimental design to create limiting cases, which while not necessarily relevant to a laser engagement scenario, allow specific processes and material properties to be isolated. Some examples for inclusion in future work include long duration low irradiance testing to determine pre-decomposition properties, re-irradiation of decomposing samples to determine changing properties, and thermal

isolation from sample mounts. Simultaneous backside imaging should be standard on all testing. The impact of integration time on the maximum range of temperature measurement must also be understood and carefully selected to capture either the full range of sample temperatures or the range of greatest interest.

Ignition of decomposition products at the surface is markedly different under conditions of piloted (requiring minimum volatile concentration) and spontaneous (requiring minimum surface temperature) ignition. The concentrations of volatile products required under conditions of piloted ignition are much less (under conditions studied here) than those already present when surface temperatures reach the spontaneous ignition temperature. Strategies for providing an ignition source early in a tactical laser engagement to initiate surface combustion may warrant further investigation. Additional experimental work investigating HEL irradiation of composite materials under conditions of piloted ignition may be warranted as well.

Appendix A. Thermal Model Sensitivity Analysis

Chapters III and IV present 3D, explicit, finite difference thermal models with boundary conditions and material decomposition reactions for the laser heating of carbon fiber reinforced polymer (CFRP) and porous graphite materials. In both cases, predicted surface temperatures are fit to measured surface temperatures to infer changing material conductivities and kinetic parameters of the decomposition reactions throughout laser irradiation. The models contained approximately 35 and 15 independent model parameters for CFRP and graphite, respectively, potentially allowing extensive tuning of the predictions and calling into question the uniqueness of the resulting fit parameters. This concern is addressed several ways throughout this work. First, literature values were used for model parameters whenever available and applicable. Second, material properties were measured when possible, particularly in the case of surface optical properties. This reduced the number of fit parameters to 12 and 9 for CFRP and graphite, respectively. Within this reduced set, a smaller subset of 3 or 4 parameters were dominant during short intervals of the test, particularly in the case of a single phase of decomposition. Lastly, a common set of fit parameters is used to fit spatial and temporal temperature variation for all experiments at multiple laser irradiation levels. Together, this serves to increase confidence in the result.

In the figures that follow, material parameters are varied individually from the results reported in Tables 3, 4, and 7 and the effect on predicted temperatures is shown. This helps to communicate the relative importance of each parameter in producing the final prediction and the amount of variance in each before the fit is affected.

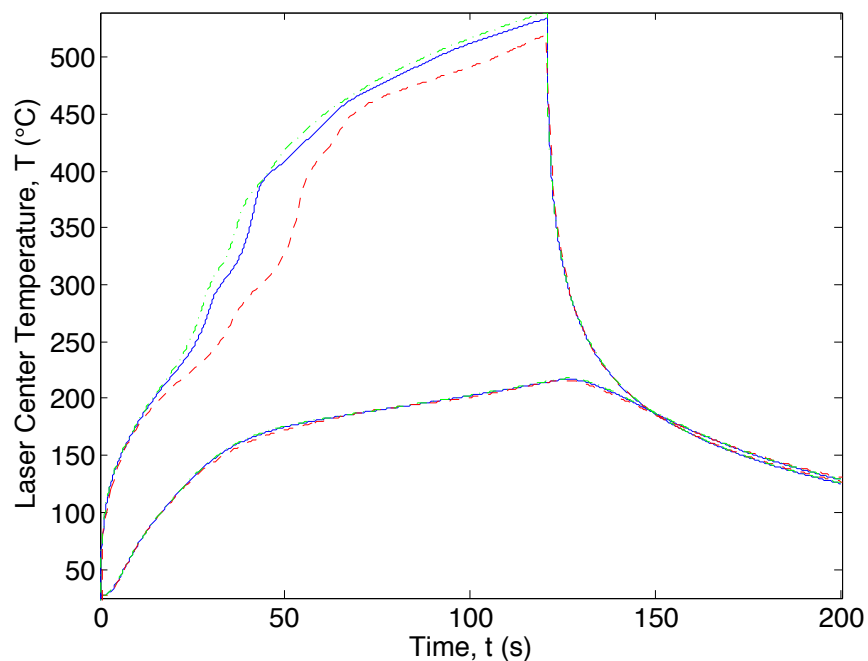


Fig. 44. Impact of the number of model elements in the thickness direction on front and backside laser center temperatures at 5 W/cm^2 with 4 ($-\cdot-$), 8 ($-$), and 16 ($- -$) elements.

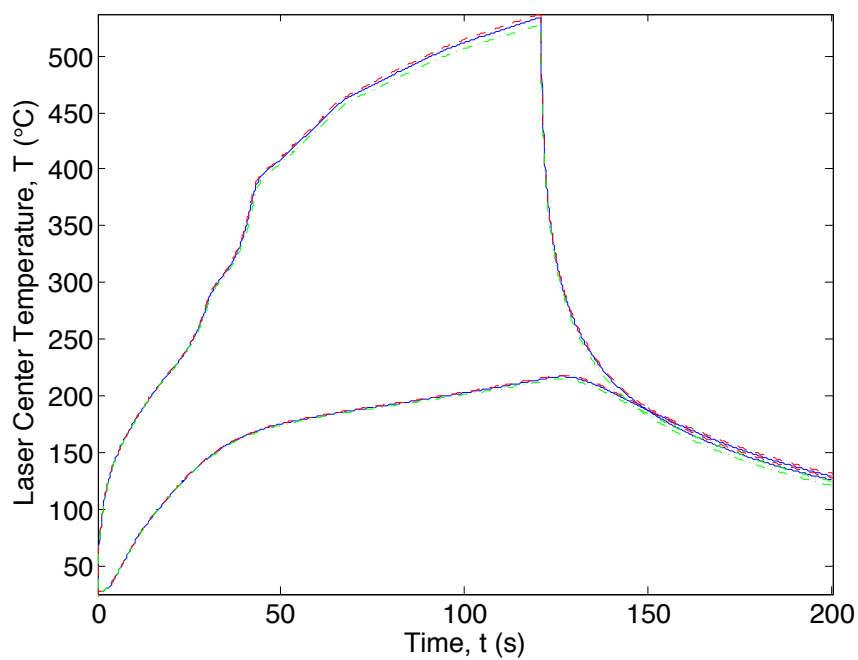


Fig. 45. Impact of the residual weight percent of char after decomposition on front and backside laser center temperatures at 5 W/cm^2 : 60% ($-\cdot-$), 40% ($-$), and 20% ($- -$).

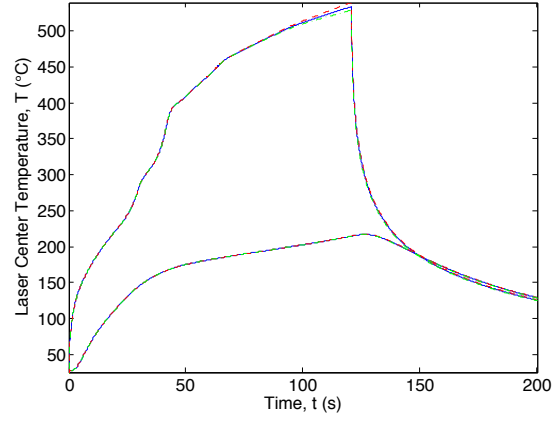


Fig. 46. Impact of radiative cooling of bare fiber on front and backside laser center temperatures at 5 W/cm^2 with $\epsilon = \epsilon(T) - 0.1$ (---), $\epsilon(T)$ (—), and $\epsilon(T) + 0.1$ (---).

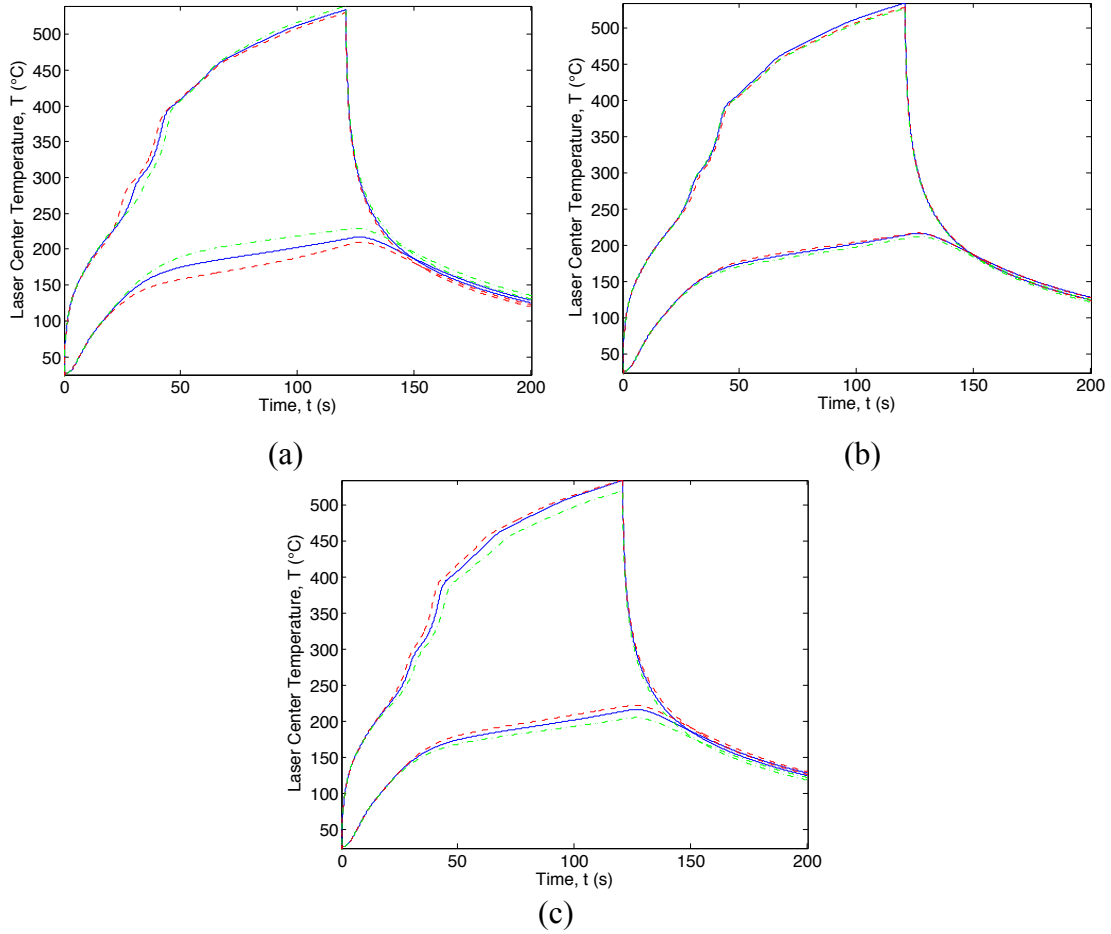


Fig. 47. Impact of the resin dehydration reaction (a) activation energy [5% reduction (---), best fit (—), and 5% increase (-·-)], (b) pre-exponential factor [25% reduction (---), best fit (—), and 25% increase (-·-)], and (c) enthalpy of reaction [25% reduction (---), best fit (—), and 25% increase (-·-)] on front and back- side laser center temperatures at 5 W/cm^2 .

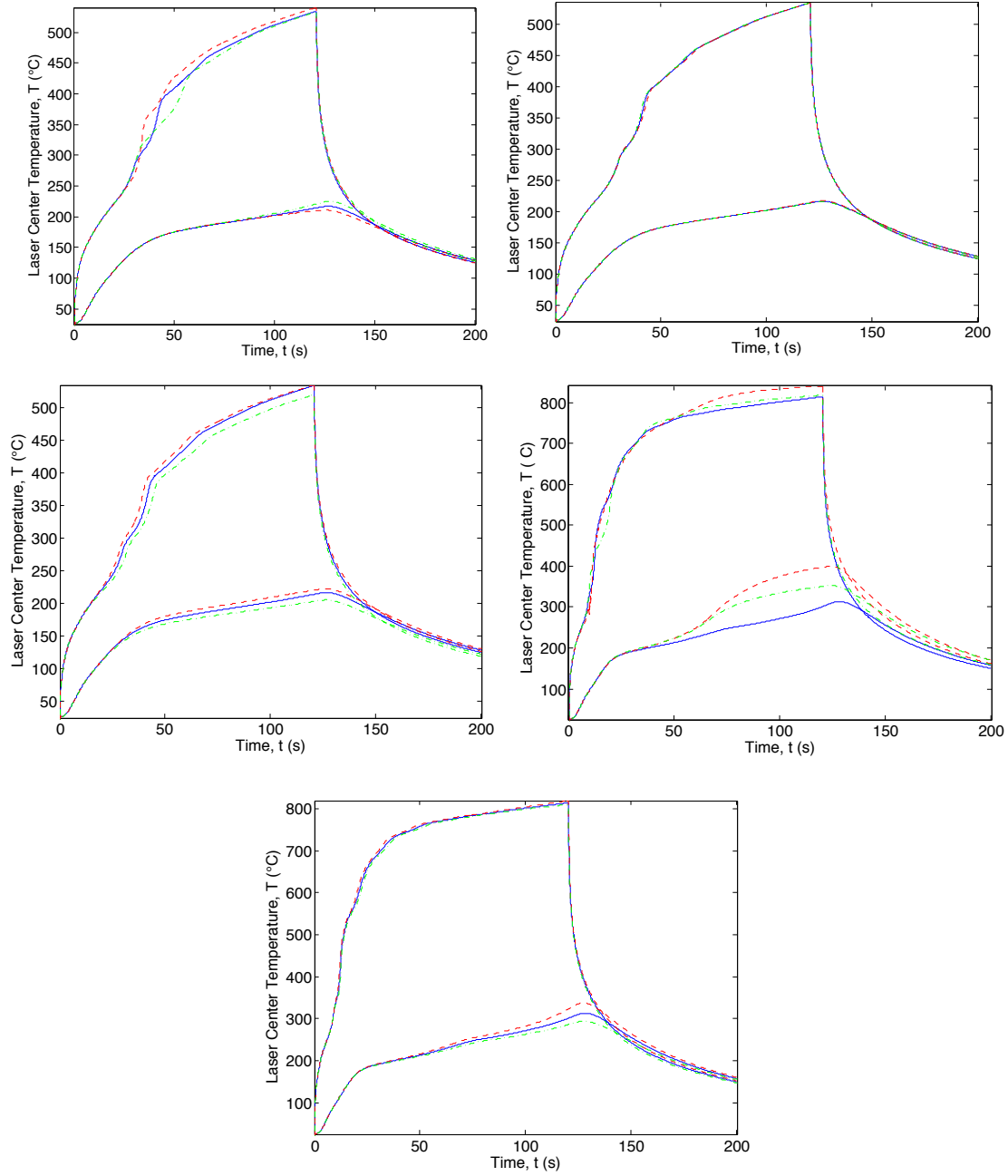


Fig. 48. Impact of the dehydrated resin decomposition reaction (a) activation energy [10% reduction (---), best fit (—), and 10% increase (- · -)], (b) pre-exponential factor [25% reduction (---), best fit (—), and 25% increase (- · -)], and (c) enthalpy of reaction [25% reduction (---), best fit (—), and 25% increase (- · -)] on front and back-side laser center temperatures at 5 W/cm². The impact of dehydrated resin decomposition reaction (d) activation energy and (e) enthalpy of reaction on laser center temperatures at 10 W/cm² is shown as well for 25% reduction (---), best fit (—), and 25% increase (- · -)

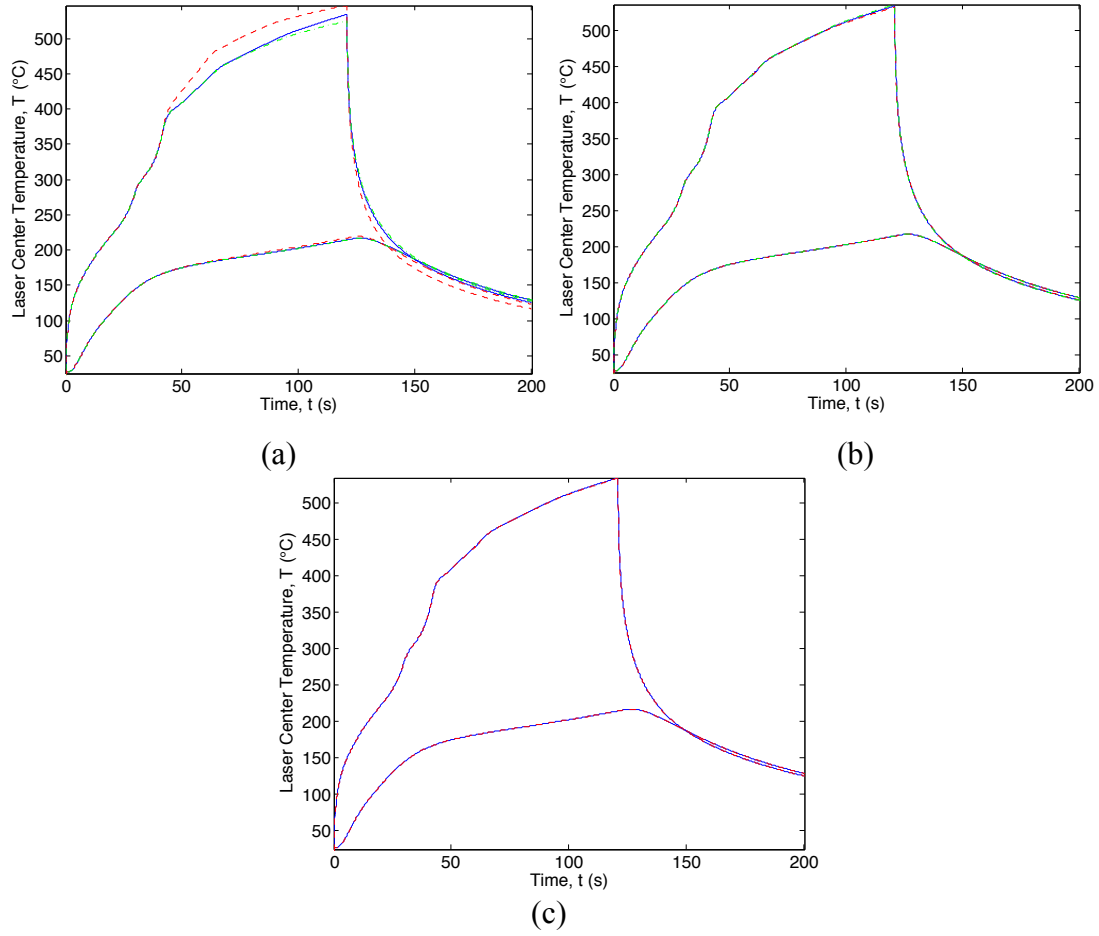


Fig. 49. Impact of the char oxidation reaction (a) activation energy [25% reduction (---), best fit (—), and 25% increase (- · -)], (b) pre-exponential factor [25% reduction (---), best fit (—), and 25% increase (- · -)], and (c) enthalpy of reaction [0.2 MJ/kg (---), none (—)] on front and back- side laser center temperatures at 5 W/cm².

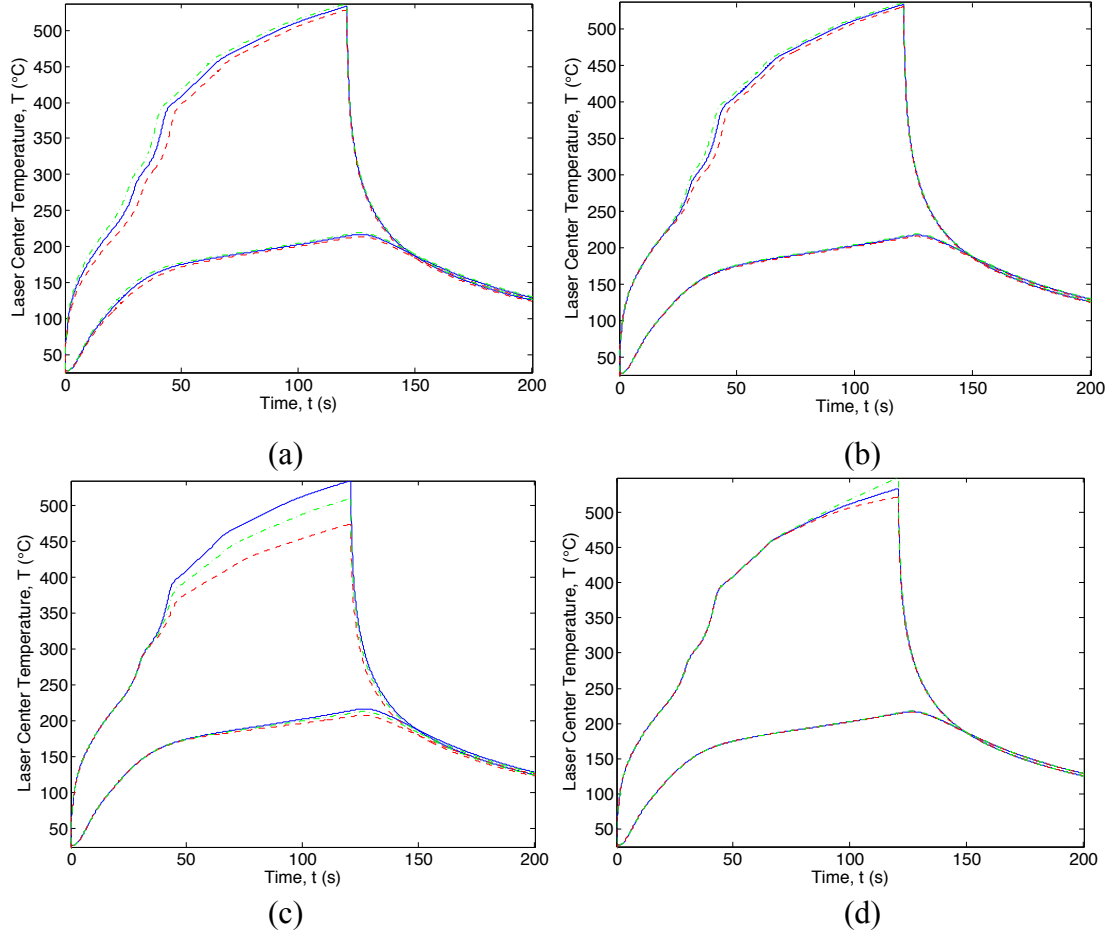


Fig. 50. Impact of the laser absorptivity of (a) virgin resin [1.0 (---), 0.93 (—), and 0.85 (---)], (b) dehydrated resin [1.0 (---), 0.93 (—), and 0.85 (---)], (c) char 0.95 [(---), 0.98 (—), and 0.75 (---)], and (d) bare fiber [$\alpha + 0.1$ (---), $\alpha(T)$ (—), and $\alpha - 0.1$ (---)] on front and backside laser center temperatures at 5 W/cm². The effect is greatest when a given decomposition phase is most abundant.

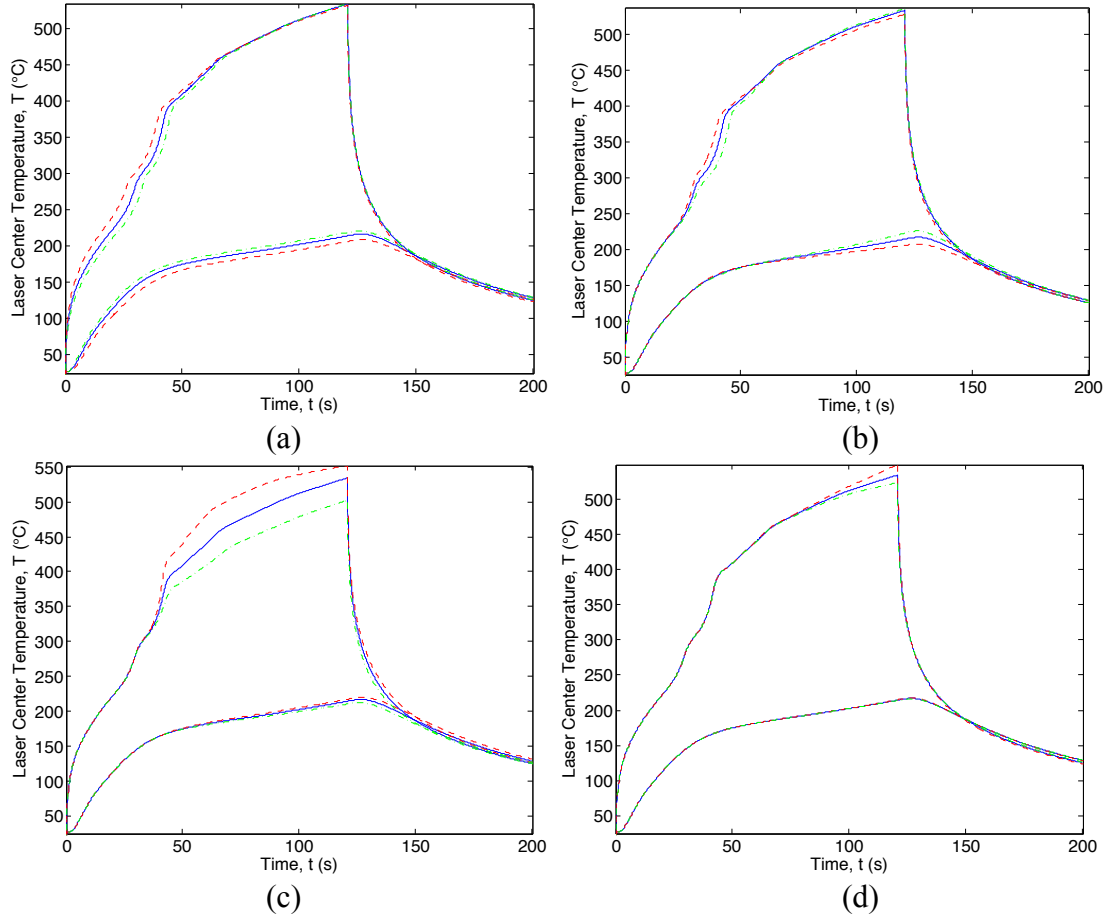


Fig. 51. Impact of the thermal conductivity in the thickness direction of (a) virgin resin, (b) dehydrated resin, (c) char, and (d) bare fiber on front and backside laser center temperatures at 5 W/cm^2 : 25% reduction (---), best fit (—), and 25% increase (- - -).

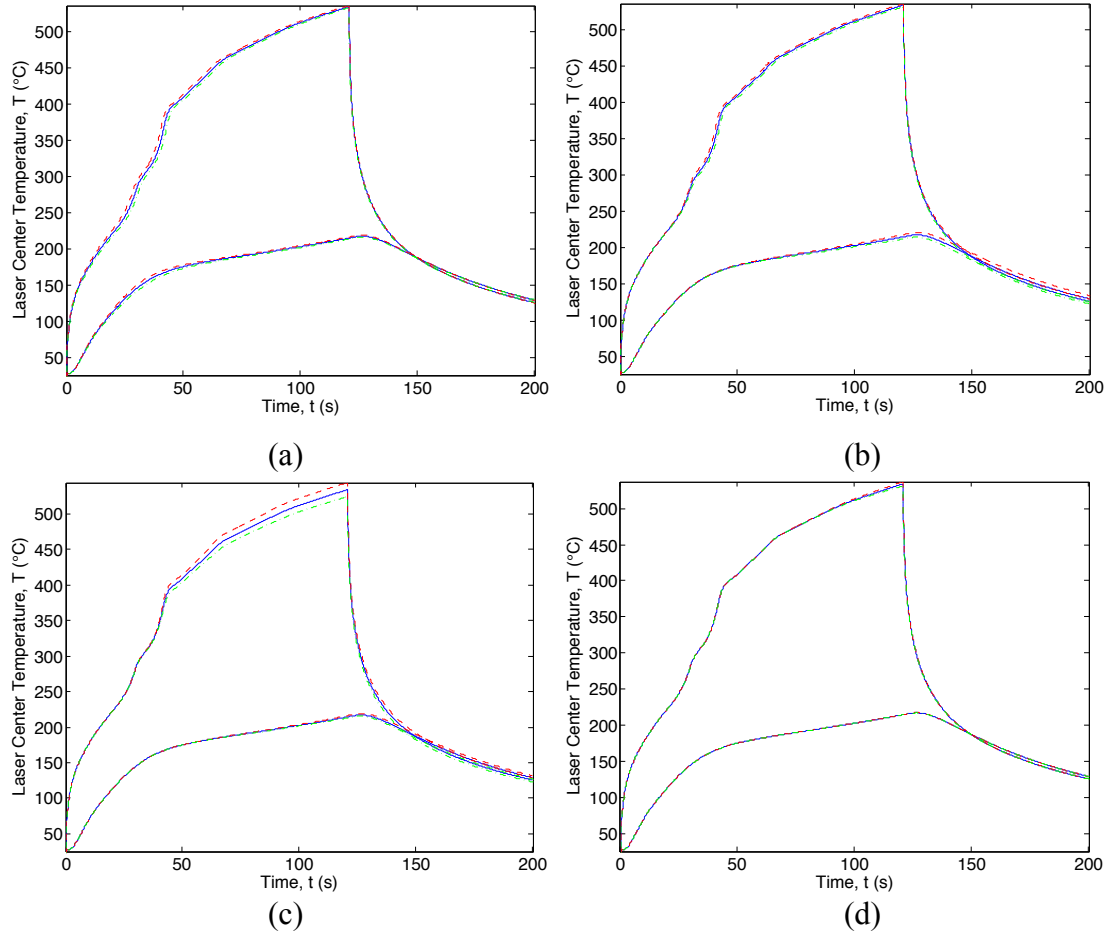


Fig. 52. Impact of the thermal conductivity in the fiber/surface planar direction of (a) virgin resin, (b) dehydrated resin, (c) char, and (d) bare fiber on front and backside laser center temperatures at 5 W/cm^2 : 25% reduction (---), best fit (—), and 25% increase (- · -).

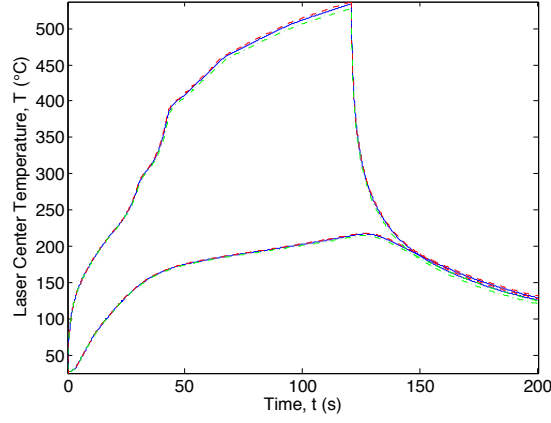


Fig. 53. Impact of the surface convection coefficient (hc) on front and back laser center temperatures at 5 W/cm^2 : 50% reduction (---), best fit (—), and 100% increase (- · -).

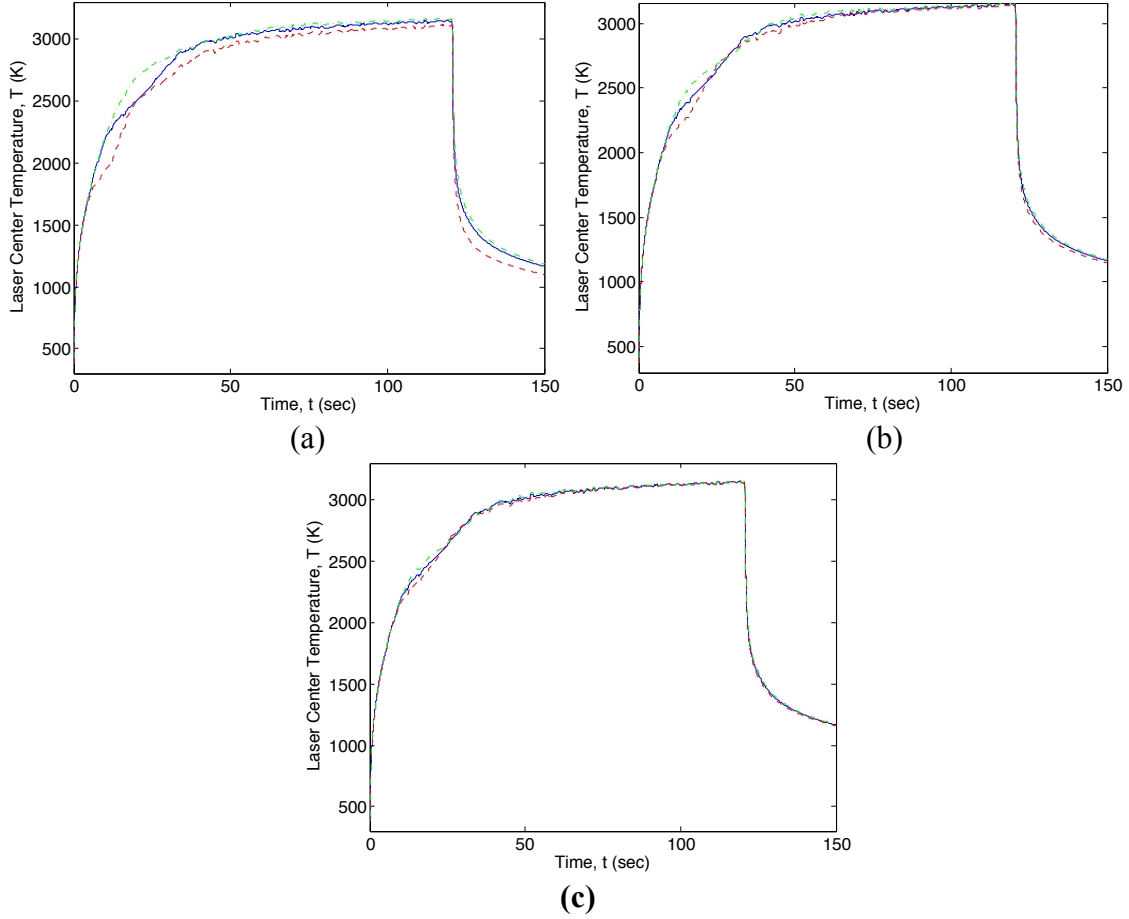


Fig. 54. Impact of graphite binder removal activation energy on front and backside laser center temperatures at 1500 W/cm^2 at varying deviations from best fit parameter: (a) 25% reduction (---), best fit (—), and 25% increase (- · -), (b) 10% reduction (---), best fit (—), and 10% increase (- · -), (c) 5% reduction (---), best fit (—), and 5% increase (- · -)

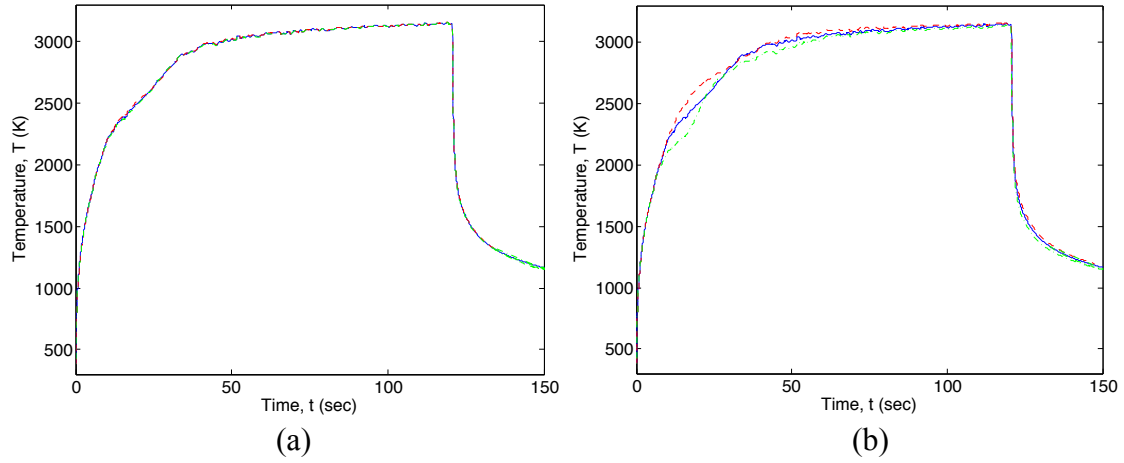


Fig. 55. Impact of the graphite binder removal pre-exponential factor on front and backside laser center temperatures at 1500 W/cm^2 for variations of (a) 25% reduction (---), best fit (—), and 25% increase (---) and (b) 90% reduction (---), best fit (—), and 1000% increase (---).

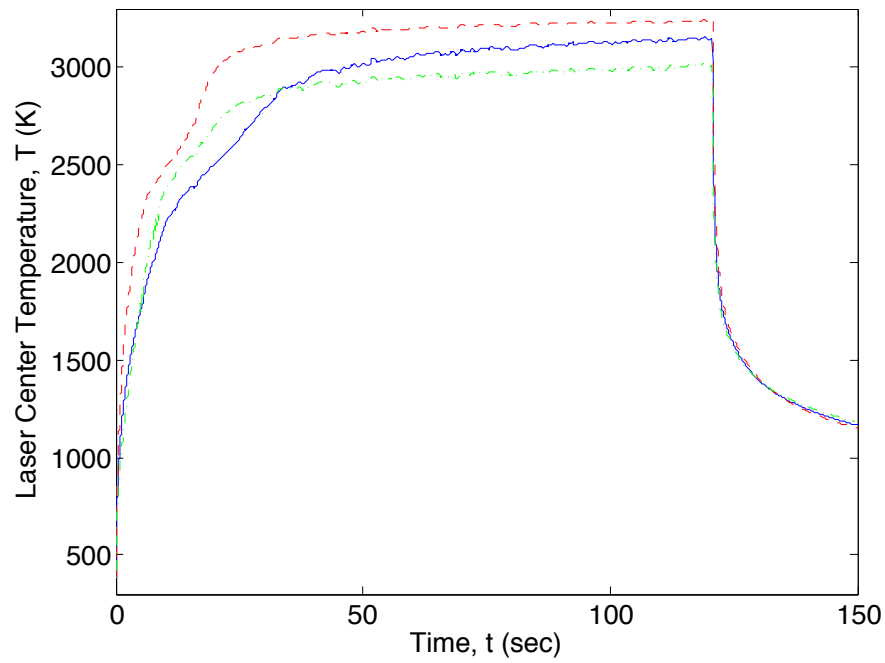


Fig. 56. Impact of the graphite conductivity on front and backside laser center temperatures at 1500 W/cm^2 for variations of (a) 25% reduction (---), best fit (—), and 25% increase (---).

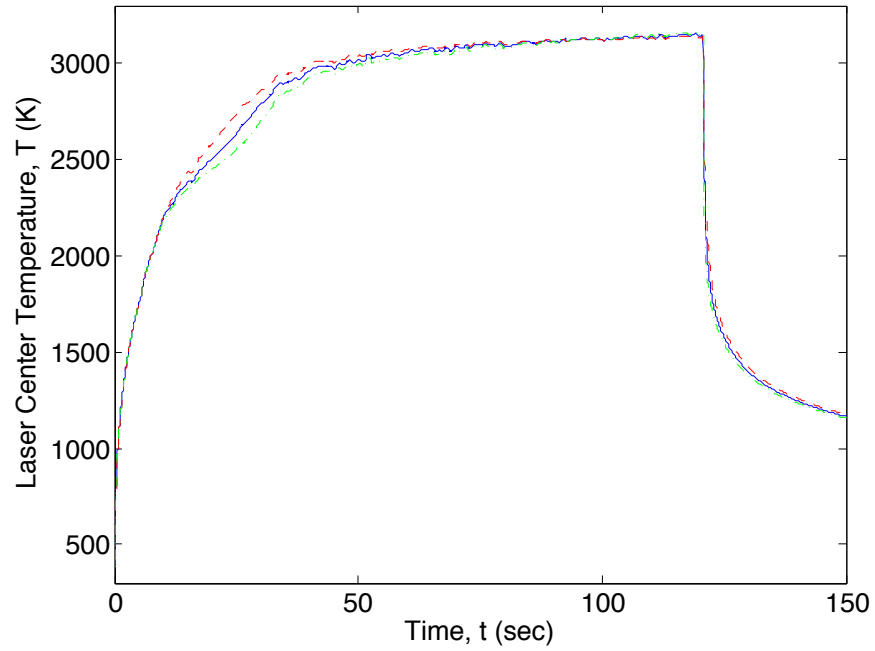


Fig. 57. Impact of the percent graphite binder initially present on front and backside laser center temperatures at 1500 W/cm^2 for variations of (a) 20% binder (---), 40% binder (—), and 60% binder (- · -).

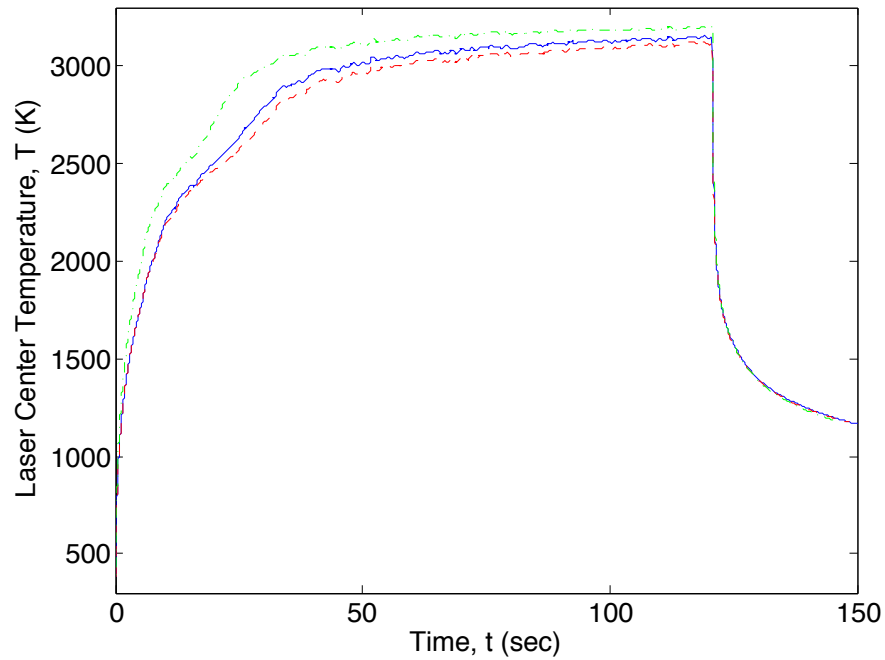


Fig. 58. Impact of the graphite absorptivity and emissivity ($\epsilon = \alpha$) on front and backside laser center temperatures at 1500 W/cm^2 for variations of (a) $\epsilon - 0.1$ (---), ϵ (—), and $\epsilon + 0.1$ (- · -).

Bibliography

- [1] G. P. Perram, S. J. Cusumano, R. L. Hengehold, and S. T. Fiorino, *An Introduction to Laser Weapons Systems*. Directed Energy Professional Society, 2010.
- [2] S. T. Fiorino, R. J. Bartell, M. J. Krizo, G. P. Perram, D. J. Fedyk, K. P. Moore, T. R. Harris, and S. J. Cusumano, “Worldwide Mission Planning Tool for Tactical Laser Systems,” *J. Aerosp. Comput. Inf. Commun.*, vol. 6, no. 8, pp. 491–505, 2009.
- [3] R. W. Duffner, *Airborne Laser: Bullets of Light*. Plenum Trade, 1997.
- [4] R. I. Acosta, K. C. Gross, G. P. Perram, S. M. Johnson, L. Dao, D. F. Medina, R. Roybal, and P. Black, “Gas-phase plume from laser-irradiated fiberglass-Reinforced polymers via imaging fourier transform spectroscopy,” *Appl. Spectrosc.*, vol. 68, no. 7, pp. 723–732, 2015.
- [5] R. F. Cozzens and R. B. Fox, “Infrared laser ablation of polymers,” *Polym. Eng. Sci.*, vol. 18, pp. 900–904, 1978.
- [6] Y. Liu and S. Kumar, “Recent Progress in Fabrication , Structure , and Properties of Carbon Fibers,” pp. 234–258, 2012.
- [7] L. H. Peebles, “Carbon Fibers: Formation, Structure, and Properties.” CRC Press, Boca Raton, FL, 1995.
- [8] J.-B. Donnet and R. C. Bansal, “Carbon Fibers.” M. Dekker, New York, 1990.
- [9] B. J. Hayes, “Effect of Resin Choice on Prepreg Processing,” in *Carbon Fibers and Their Composites*, E. Fitzer, Ed. Springer-Verlag, 1985.
- [10] A. P. Mouritz and A. G. Gibson, *Fire Properties of Polymer Composite Materials*, 1st ed. Dordrecht: Springer, 2006.
- [11] S. H. Goodman, “Epoxy Resins,” in *Handbook of Thermoset Plastics*, Park Ridge: Noyes Publications, 1986, pp. 132–182.
- [12] S.-M. Lee, D.-S. Kang, and J.-S. Roh, “Bulk graphite: materials and manufacturing process,” *Carbon Lett.*, vol. 16, no. 3, pp. 135–146, 2015.
- [13] A. R. Ubbelohde and F. A. Lewis, *Graphite and Its Crystal Compounds*. Oxford, 1960.

- [14] T. Stratoudaki, C. Edwards, S. Dixon, and S. B. Palmer, "Optical absorption of epoxy resin and its role in the laser ultrasonic generation mechanism in composite materials," *Rev. Quant. Nondestruct. Eval.*, vol. 22, pp. 965–972, 2003.
- [15] A. D. W. McKie and R. C. Addison, "Practical considerations for the rapid inspection of composite materials using laser-based ultrasound," *Ultrasonics*, vol. 32, no. 5, pp. 333–345, 1994.
- [16] G Neuer, "Emissivity measurements on graphite and composite materials in the visible and infrared spectral range," *QIRT 92 - Eurotherm Ser. 27*, 1992.
- [17] C. a. Silva, E. (Ed) Marotta, M. Schuller, L. Peel, and M. O'Neill, "In-Plane Thermal Conductivity in Thin Carbon Fiber Composites," *J. Thermophys. Heat Transf.*, vol. 21, no. 3, pp. 460–467, 2007.
- [18] M. Pilling, B. Yates, M. Black, and P. Tattersall, "The thermal conductivity of carbon fibre-reinforced composites," *J. Mater. Sci.*, vol. 10, no. 4, pp. 246–246, 1979.
- [19] S. D. McIvor, M. I. Darby, G. H. Wostenholm, and B. Yates, "Thermal conductivity measurements of some glass fibre- and carbon fibre-reinforced plastics," *J. Mater. Sci.*, vol. 25, pp. 3127–3132, 1990.
- [20] E. P. Scott and J. V. Beck, "Estimation of Thermal Properties in Epoxy Matrix/Carbon Fiber Composite Materials," *J. Compos. Mater.*, vol. 26, no. 1, pp. 132–149, 1992.
- [21] S. Feih and A. P. Mouritz, "Tensile properties of carbon fibres and carbon fibre-polymer composites in fire," *Compos. Part A Appl. Sci. Manuf.*, vol. 43, no. 5, pp. 765–772, 2012.
- [22] N. Grassie, M. I. Guy, and N. H. Tennent, "Degradation of Epoxy Polymers : Part 4 Thermal Degradation of Bisphenol-A Diglycidyl Ether Cured with Ethylene Diamine," *Polym. Degrad. Stab.*, vol. 14, pp. 125–137, 1986.
- [23] H. Nakagawa, S. Tsuge, and T. Koyama, "Studies on thermal degradation of epoxy resins by high-resolution pyrolysis-gas chromatography," *J. Anal. Appl. Pyrolysis*, vol. 12, no. 2, pp. 97–113, 1987.
- [24] K. S. Chen and R. Z. Yeh, "Pyrolysis kinetics of epoxy resin in a nitrogen atmosphere," *J. Hazard. Mater.*, vol. 49, pp. 105–113, 1996.
- [25] R. B. Prime, H. E. Bair, S. Vyazovkin, P. K. Gallagher, and A. Riga, "Thermogravimetric Analysis," in *Thermal Analysis of Polymer*, J. D. Menczel and R. B. Prime, Eds. Hoboken, N.J.: John Wiley.

- [26] P. Budrugaec and E. Segal, "Application of isoconversional and multivariate non-linear regression methods for evaluation of the degradation mechanism and kinetic parameters of an epoxy resin," *Polym. Degrad. Stab.*, vol. 93, pp. 1073–1080, 2008.
- [27] E. Kandare, B. K. Kandola, P. Myler, and G. Edwards, "Thermo-mechanical Responses of Fiber-reinforced Epoxy Composites Exposed to High Temperature Environments. Part I: Experimental Data Acquisition," *J. Compos. Mater.*, vol. 44, no. 26, pp. 3093–3114, 2010.
- [28] N. Rose, M. Le Bras, S. Bourbigot, R. Delobepb, and B. Castes, "Comprehensive study of the oxidative degradation of an epoxy resin using the degradation front model," *Polym. Degrad. Stab.*, vol. 3910, no. 96, 1996.
- [29] N. Rose, M. Le Bras, S. Bourbigot, and R. Delobel, "Thermal oxidative degradation of epoxy resins : evaluation of their heat resistance using invariant kinetic parameters," *Polym. Degrad. Stab.*, vol. 45, pp. 387–397, 1994.
- [30] E. Kandare, B. K. Kandola, and J. E. J. Staggs, "Global kinetics of thermal degradation of flame-retarded epoxy resin formulations," *Polym. Degrad. Stab.*, vol. 92, no. 10, pp. 1778–1787, 2007.
- [31] E. L. Dereniak and G. D. Boreman, *Infrared Detectors and Systems*, 1st ed. John Wiley & Sons, Inc., 1996.
- [32] T. J. Quinn, *Temperature*, 2nd ed. Academic Press, 1990.
- [33] S. T. Yang, M. J. Matthews, S. Elhadj, V. G. Draggoo, and S. E. Bisson, "Thermal transport in CO₂ laser irradiated fused silica: In situ measurements and analysis," *J. Appl. Phys.*, vol. 106, no. 10, pp. 1–7, 2009.
- [34] S. Elhadj, M. J. Matthews, S. T. Yang, D. J. Cooke, J. S. Stolken, R. M. Vignes, V. G. Draggoo, and S. E. Bisson, "Determination of the intrinsic temperature dependent thermal conductivity from analysis of surface temperature of laser irradiated materials," *Appl. Phys. Lett.*, vol. 96, no. 7, pp. 4–7, 2010.
- [35] S. Elhadj, M. J. Matthews, S. T. Yang, and D. J. Cooke, "Evaporation kinetics of laser heated silica in reactive and inert gases based on near-equilibrium dynamics," *Opt. Express*, vol. 20, no. 2, p. 1575, 2012.
- [36] R. F. Cozzens, M. Evans, and J. Duncan, "High Energy Laser Lethality Involving Carbon Fiber Reinforced Composite Material," *DTIC*, 2013.

- [37] J. B. Henderson, J. A. Wiebelt, and M. R. Tant, "A Model for the Thermal Response of Polymer Composite Materials with Experimental Verification," *J. Compos. Mater.*, vol. 19, pp. 579–595, 1985.
- [38] R. D. Chippendale, I. O. Golosnoy, and P. L. Lewin, "Numerical modelling of thermal decomposition processes and associated damage in carbon fibre composites," *J. Phys. D. Appl. Phys.*, vol. 47, no. 38, p. 385301, 2014.
- [39] E. D. McCarthy, B. K. Kandola, G. Edwards, P. Myler, J. Yuan, Y. C. Wang, and E. Kandare, "Modelling flaming combustion in glass fibre-reinforced composite laminates," *J. Compos. Mater.*, vol. 47, no. 19, pp. 2371–2384, 2012.
- [40] J. B. Henderson, M. R. Tant, and G. R. Moore, "Determination of Kinetic Parameters for the Thermal Decomposition of Phenolic Ablative Materials by a Multiple Heating Rate Method," *Thermochim. Acta*, vol. 44, pp. 253–264, 1981.
- [41] A. G. Gibson, Y.-S. Wu, H. W. Chandler, J. A. D. Wilcox, and P. Bettess, "A model for the thermal performance of thick composite laminates in hydrocarbon fires," *Rev. L'Institut Fr. du Pet.*, vol. 50, pp. 69–74, 1995.
- [42] J. Florio, J. B. Henderson, F. L. Test, and R. Hariharan, "A study of the effects of the assumption of local thermal equilibrium on the overall thermally-induced response of a decomposition, glass-filled polymer composite," *Int. J. Heat Mass Transf.*, vol. 34, pp. 135–147, 1991.
- [43] A. P. Mouritz and Z. Mathys, "Post-fire mechanical properties of marine polymer composites," *Compos. Struct.*, vol. 47, no. 47, pp. 643–653, 1999.
- [44] G. A. Pering, P. V Farrell, and G. S. Springer, "Degradation of tensile and shear properties of composites exposed to fire or high temperature," *J. Compos. Mater.*, vol. 14, pp. 54–66, 1980.
- [45] S. Feih, A. P. Mouritz, Z. Mathys, and A. G. Gibson, "Tensile Strength Modeling of Glass Fiber—Polymer Composites in Fire," *J. Compos. Mater.*, vol. 41, no. 19, pp. 2387–2410, 2007.
- [46] L. A. Burns, S. Feih, and A. P. Mouritz, "Compression Failure of Carbon Fiber-Epoxy Laminates in Fire," *J. Aircr.*, vol. 47, no. 2, pp. 528–533, 2010.
- [47] S. Feih and A. P. Mouritz, "Tensile properties of carbon fibres and carbon fibre-polymer composites in fire," *Off. Nav. Res. Compos. Fire*, vol. 43, no. 5, pp. 765–772, 2012.

- [48] C. Sauder, J. Lamon, and R. Pailler, "Thermomechanical properties of carbon fibres at high temperatures (up to 2000 °C)," *Compos. Sci. Technol.*, vol. 62, no. 4, pp. 499–504, 2002.
- [49] C. Sauder, J. Lamon, and R. Pailler, "The tensile behavior of carbon fibers at high temperatures up to 2400 °C," *Carbon N. Y.*, vol. 42, no. 4, pp. 715–725, 2004.
- [50] J. L. Massman and K. C. Gross, "Understanding the influence of turbulence in imaging Fourier transform spectroscopy of smokestack plumes," *Proc. SPIE*, vol. 8048, p. 80480A.
- [51] E. A. Moore, K. C. Gross, S. J. Bowen, G. P. Perram, M. Chamberland, V. Farley, J.-P. Gagnon, P. Lagueux, and A. Villemaire, "Characterizing and overcoming spectral artifacts in imaging Fourier-transform spectroscopy of turbulent exhaust plumes," *Proc. SPIE*, vol. 7304, p. 730416.
- [52] K. C. Bradley, K. C. Gross, and G. P. Perram, "Imaging Fourier Transform Spectrometry of Chemical Plumes," *Proc. SPIE*, vol. 7304, p. 73040J.
- [53] S. Savary, J.-P. Gagnon, K. Gross, P. Tremblay, M. Chamberland, and V. Farley, "Standoff identification and quantification of flare emissions using infrared hyperspectral imaging," *Proc. SPIE*, vol. 8024, p. 80240T.
- [54] R. I. Acosta, K. C. Gross, and G. P. Perram, "Thermal degradation of Poly(methyl methacrylate) with a 1.064 μm Nd:YAG laser in a buoyant flow," *Polym. Degrad. Stab.*, vol. 121, pp. 78–89, 2015.
- [55] R. I. Acosta, K. C. Gross, and G. P. Perram, "Combustion kinetics of laser irradiated porous graphite from imaging Fourier transform spectroscopy," *Combust. Flame*, vol. 163, pp. 90–99, 2015.
- [56] "NIST Chemistry WebBook," *National Institute of Standards and Technology*. [Online]. Available: <http://webbook.nist.gov/chemistry/>. [Accessed: 08-Mar-2016].
- [57] R. J. Bartell, G. P. Perram, S. T. Fiorino, S. N. Long, M. J. Houle, C. A. Rice, Z. P. Manning, D. W. Bunch, M. J. Krizo, and L. E. Gravley, "Methodology for comparing worldwide performance of diverse weight-constrained high energy laser systems," *Laser Source Syst. Technol. Def. Secur.*, vol. 5792, no. 1, pp. 76–87, 2005.
- [58] C. Soutis, "Fibre reinforced composites in aircraft construction," *Prog. Aerosp. Sci.*, vol. 41, no. 2, pp. 143–151, 2005.

- [59] C. D. Boley and A. M. Rubenchik, "Modeling of laser interactions with composite materials," *Appl. Opt.*, vol. 52, no. 14, pp. 3329–3337, 2013.
- [60] A. Oberlin, "Carbonization and graphitization," *Carbon N. Y.*, vol. 22, no. 6, pp. 521–541, 1984.
- [61] J. B. Henderson and T. E. Wiecek, "A Mathematical Model to Predict the Thermal Response of Decomposing, Expanding Polymer Composites," *J. Compos. Mater.*, vol. 21, pp. 373–393, 1987.
- [62] S. M. Baumann, C. Keenan, M. A. Marciniak, and G. P. Perram, "Spectral and temperature-dependent infrared emissivity measurements of painted metals for improved temperature estimation during laser damage testing," *Proc. SPIE*, vol. 9237, p. 923713, 2014.
- [63] Neuer, "Spectral and Total Emissivity Measurements of Highly Emitting Materials," *Int. J. Thermophys.*, vol. 16, no. 1, pp. 257–265, 1995.
- [64] G. W. Autio and E. Scala, "The normal spectral emissivity of isotropic and anisotropic materials," *Carbon N. Y.*, vol. 4, no. 1, pp. 13–28, 1966.
- [65] Y. Touloukian, "Thermal radiative properties: nonmetallic solids," *Thermophys. Prop. Matter, Vol.8*, 1972.
- [66] R. K. Freeman, F. A. Rigby, and N. Morley, "Temperature-Dependent Reflectance of Plated Metals and Composite Materials Under Laser Irradiation," *J. Thermophys. Heat Transf.*, vol. 14, no. 3, pp. 305–312, 2000.
- [67] F. P. Incropera and D. P. DeWitt, *Fundamentals of Heat and Mass Transfer*, 4th ed. New York: John Wiley & Sons, Ltd., 1996.
- [68] E. Gutierrez-Miravete, "Chapter 6 Numerical Methods for Transient Problems." [Online]. Available: <http://www.ewp.rpi.edu/hartford/~wallj2/CHT/Notes/ch06.pdf>. [Accessed: 16-Mar-2016].
- [69] G. Kalogiannakis, D. Van Hemelrijck, and G. Van Assche, "Measurements of Thermal Properties of Carbon/Epoxy and Glass/Epoxy using Modulated Temperature Differential Scanning Calorimetry," *J. Compos. Mater.*, vol. 38, no. 2, pp. 163–175, 2004.
- [70] E. Kandare, B. K. Kandola, D. McCarthy, P. Myler, G. Edwards, Y. Jifeng, and Y. C. Wang, "Fiber-reinforced epoxy composites exposed to high temperature environments . Part II : modeling mechanical property degradation," *J. Compos. Mater.*, vol. 45, no. 14, pp. 1511–1521, 2010.

- [71] N. Rose, M. Le Bras, R. Delobel, B. Costes, and Y. Henry, "Thermal oxidative degradation of an epoxy resin," *Polym. Degrad. Stab.*, vol. 42, pp. 307–316, 1993.
- [72] P. Mucha, R. Weber, N. Speker, P. Berger, B. Sommer, and T. Graf, "Calibrated Heat Flow Model for Determining the Heat Conduction Losses in Laser Cutting of CFRP," *Phys. Procedia*, vol. 56, pp. 1208–1217, 2014.
- [73] G. T. Phillips, W. A. Bauer, C. D. Fox, A. E. Gonzales, N. C. Herr, R. C. Gosse, and G. P. Perram, "Mass removal by oxidation and sublimation of porous graphite during fiber laser irradiation," *Opt. Eng.*, vol. 56, no. 1, 2016.
- [74] H. K. Chelliah, A. Makino, I. Kato, N. Araki, and C. K. Law, "Modeling of graphite oxidation in a stagnation-point flow field using detailed homogeneous and semiglobal heterogeneous mechanisms with comparisons to experiments," *Combust. Flame*, vol. 104, no. 4, pp. 469–480, 1996.
- [75] A. Makino, N. Araki, and Y. Mihara, "Combustion of artificial graphite in stagnation flow: Estimation of global kinetic parameters from experimental results," *Combust. Flame*, vol. 96, no. 3, pp. 261–274, 1994.
- [76] T. M. Linjewile, V. S. Gururajan, and P. K. Agarwal, "The CO CO₂ product ratio from the combustion of single petroleum coke spheres in an incipiently fluidized bed," *Chem. Eng. Sci.*, vol. 50, no. 12, pp. 1881–1888, 1995.
- [77] A. E. Gonzales, "Kinetics of Graphite Oxidation in Reacting Flow From Imaging Fourier Transform Spectroscopy," 2016.
- [78] A. G. Whittaker, P. L. Kintner, L. S. Nelson, and N. Richardson, "Carbon Vapor Pressure in the Range 3450 to 4500 K and Evidence for Melting at ~3800 K," *DTIC*, pp. 1–59, 1981.
- [79] N. A. Gokcen, E. T. Chang, and T. M. Poston, "Determination of Graphite-Liquid-Vapor Triple Point by Laser Heating," *DTIC*, pp. 1–60, 1976.
- [80] A. A. Voevodin, J. G. Jones, J. S. Zabinski, Z. Czigany, and L. Hultman, "Growth and structure of fullerene-like CN x thin films produced by pulsed laser ablation of graphite in nitrogen," *J. Appl. Phys.*, vol. 92, no. 9, pp. 4980–4988, 2002.
- [81] A. A. Puretzky, D. J. Styers-Barnett, C. M. Rouleau, H. Hu, B. Zhao, I. N. Ivanov, and D. B. Geohegan, "Cumulative and continuous laser vaporization synthesis of single wall carbon nanotubes and nanohorns," *Appl. Phys. A Mater. Sci. Process.*, vol. 93, no. 4, pp. 849–855, 2008.

- [82] C. D. Scott, S. Arepalli, P. Nikolaev, and R. E. Smalley, "Growth mechanisms for single-wall carbon nanotubes in a laser-ablation process," *Appl. Phys. A Mater. Sci. Process.*, vol. 72, no. 5, pp. 573–580, 2001.
- [83] A. Semerok, S. V. Fomichev, J. M. Weulersse, F. Brygo, P. Y. Thro, and C. Grisolia, "Heating and ablation of tokamak graphite by pulsed nanosecond Nd-YAG lasers," *J. Appl. Phys.*, vol. 101, no. 8, pp. 0–10, 2007.
- [84] A. K. Dubey and V. Yadava, "Laser beam machining-A review," *Int. J. Mach. Tools Manuf.*, vol. 48, no. 6, pp. 609–628, 2008.
- [85] L. Babout, B. J. Marsden, P. M. Mummery, and T. J. Marrow, "Three-dimensional characterization and thermal property modelling of thermally oxidized nuclear graphite," *Acta Mater.*, vol. 56, no. 16, pp. 4242–4254, 2008.
- [86] A. M. Rubenchik, S. S. Q. Wu, V. K. Kanz, M. M. LeBlanc, W. H. Lowdermilk, M. D. Rotter, and J. R. Stanley, "Temperature-dependent 780-nm laser absorption by engineering grade aluminum, titanium, and steel alloy surfaces," *Opt. Eng.*, vol. 53, no. 12, p. 122506, 2014.
- [87] R. G. Wilson and C. R. Spitzer, "Visible and near-infrared emittance of ablation chars and carbon," *AIAA J.*, vol. 6, no. 4, pp. 665–671, 1968.
- [88] O. Rozenbaum, D. De Sousa Meneses, and P. Echegut, "Texture and porosity effects on the thermal radiative behavior of alumina ceramics," *Int. J. Thermophys.*, vol. 30, no. 2, pp. 580–590, 2009.
- [89] K. K. Kelley, "High-Temperature Heat content, heat capacity, and entropy data for the elements and inorganic compounds," *Bureau of Mines*, vol. Bulletin 5. 1960.
- [90] A. Cezairliyan and A. P. Miiller, "Heat capacity and electrical resistivity of POCO AXM-5Q1 graphite in the range 1500-3000 K by a pulse-heating technique," *Int. J. Thermophys.*, vol. 6, no. 3, pp. 285–300, 1985.
- [91] C. Uher, "4.3.2 - Temperature dependence of thermal conductivity of graphite," in *Thermal Conductivity of Pure Metals and Alloys*, 1991, pp. 430–439.
- [92] A. I. Savvatimskiy, "Measurements of the melting point of graphite and the properties of liquid carbon (a review for 1963-2003)," *Carbon N. Y.*, vol. 43, no. 6, pp. 1115–1142, 2005.
- [93] J. Abrahamson, "Graphite sublimation temperatures, carbon arcs and crystallite erosion," *Carbon N. Y.*, vol. 12, no. 2, 1974.

- [94] NIST, “NIST-JANAF Thermochemical Tables,” 1983. [Online]. Available: <http://kinetics.nist.gov/janaf/html/C-003.html>. [Accessed: 01-Aug-2016].
- [95] A. G. Gibson, A. P. Mouritz, Y. Wu, C. P. Gardiner, and Z. Mathys, *Validation of the Gibson model for the fire reaction properties of fibre-polymer composites*. Newcastle, 2003.

Vita

Captain Nicholas C. Herr graduated from Elizabethtown Area High School in Elizabethtown, Pennsylvania. He attended the United States Air Force Academy in Colorado Springs, Colorado, where he was a Distinguished Graduate and received a Bachelor of Science in Materials Science and a commission as a Second Lieutenant in the Air Force in May 2008.

His first assignment was at Wright-Patterson AFB, OH as a student at the Air Force Institute of Technology (AFIT). He graduated from AFIT as a Distinguished Graduate and received a Masters degree in Materials Science in March 2010. His next assignment was to the Air Force Corrosion Prevention and Control Office at Robins AFB, GA where he managed research projects to improve Air Force corrosion prevention materials and techniques. While also at Robins AFB, Captain Herr worked in the 402nd Commodities Maintenance Group Engineering Support Flight to support metal finishing operations and transition production to a new state-of-the-art facility. In August 2013, he returned to AFIT to pursue his PhD. Upon completion, he will join the faculty in AFIT's Engineering Physics department.

REPORT DOCUMENTATION PAGE				Form Approved OMB No. 074-0188	
<p>The public reporting burden for this collection of information is estimated to average 1 hour per response, including the time for reviewing instructions, searching existing data sources, gathering and maintaining the data needed, and completing and reviewing the collection of information. Send comments regarding this burden estimate or any other aspect of the collection of information, including suggestions for reducing this burden to Department of Defense, Washington Headquarters Services, Directorate for Information Operations and Reports (0704-0188), 1215 Jefferson Davis Highway, Suite 1204, Arlington, VA 22202-4302. Respondents should be aware that notwithstanding any other provision of law, no person shall be subject to a penalty for failing to comply with a collection of information if it does not display a currently valid OMB control number.</p> <p>PLEASE DO NOT RETURN YOUR FORM TO THE ABOVE ADDRESS.</p>					
1. REPORT DATE (DD-MM-YYYY) 16-09-2016		2. REPORT TYPE Doctoral Dissertation		3. DATES COVERED (From – To) August 2013 – September 2016	
TITLE AND SUBTITLE DEGRADATION OF CARBON FIBER REINFORCED POLYMER AND GRAPHITE BY LASER HEATING				5a. CONTRACT NUMBER	
				5b. GRANT NUMBER	
				5c. PROGRAM ELEMENT NUMBER	
6. AUTHOR(S) Herr, Nicholas C., Captain, USAF				5d. PROJECT NUMBER	
				5e. TASK NUMBER	
				5f. WORK UNIT NUMBER	
7. PERFORMING ORGANIZATION NAMES(S) AND ADDRESS(S) Air Force Institute of Technology Graduate School of Engineering and Management (AFIT/EN) 2950 Hobson Way, Building 640 WPAFB OH 45433-8865				8. PERFORMING ORGANIZATION REPORT NUMBER AFIT-ENP-DS-16-S-025	
9. SPONSORING/MONITORING AGENCY NAME(S) AND ADDRESS(ES) High Energy Laser Joint Technology Office 901 University Blvd. SE, Suite 100 Albuquerque, NM 87106 505-248-8208 harro.ackermann@jto.hpc.mil ATTN: Dr. Harro Ackermann				10. SPONSOR/MONITOR'S ACRONYM(S) HEL-JTO	
				11. SPONSOR/MONITOR'S REPORT NUMBER(S)	
12. DISTRIBUTION/AVAILABILITY STATEMENT DISTRIBUTION STATEMENT A. APPROVED FOR PUBLIC RELEASE; DISTRIBUTION UNLIMITED.					
13. SUPPLEMENTARY NOTES This material is declared a work of the U.S. Government and is not subject to copyright protection in the United States.					
14. ABSTRACT The availability of high power, diode pumped solid state and fiber lasers at powers > 10 kW and shorter wavelengths (1.07 μm) has invigorated the development of tactical laser weapons. This shift to tactical missions greatly increases the variety of potential targets including carbon fiber reinforced polymers and related materials. The complexity of laser-material interactions has driven a historical reliance on live-fire testing and empirical models, but this becomes more difficult as the number of target materials grow. This dissertation combines thermal imagery and existing thermal models of the fire response of composite materials to develop a hybrid modeling approach of laser-induced material heating and degradation. The resulting approach is used to develop thermal models of carbon fiber reinforced polymer and graphite materials and applied to the modeling of remaining composite compressive strength after laser irradiation. The dependence of laser-induced surface ignition on surface temperatures and the concentrations of combustible decomposition products is also explored.					
15. SUBJECT TERMS Carbon Fiber, Graphite, High Power Laser, Emissivity, Laser Heating, Thermal Model, Temperature Measurement					
16. SECURITY CLASSIFICATION OF:			17. LIMITATION OF ABSTRACT UU	18. NUMBER OF PAGES 143	19a. NAME OF RESPONSIBLE PERSON Dr. Glen P. Perram, AFIT/ENP
a. REPORT U	b. ABSTRACT U	c. THIS PAGE U			19b. TELEPHONE NUMBER (Include area code) (937) 255-6565, ext 4504 Glen.Perram@afit.edu

